

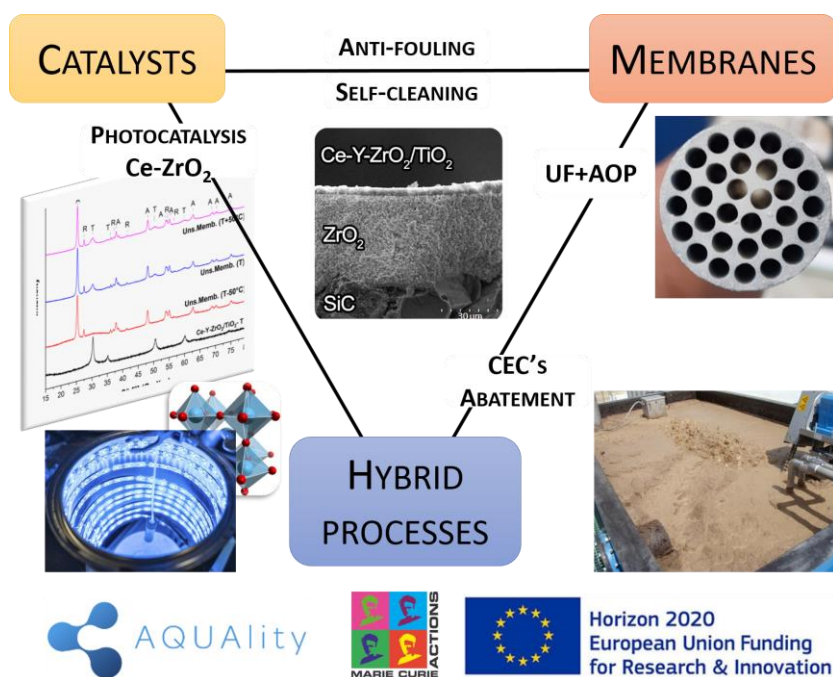


Università degli Studi di Torino

Doctoral School of the University of Torino

PhD Programme in Chemical and Materials Sciences XXXIII Cycle

Catalytic Membranes for Separation and Abatement of Contaminants from Drinking Water and Wastewater



Fabrício Eduardo Bortot Coelho

Supervisor:

Prof. Giuliana Magnacca

Co-supervisor:

Dr. Victor M. Candelario



Università degli Studi di Torino

Doctoral School of the University of Torino

PhD Programme in Chemical and Materials Sciences 35 cycle

Catalytic Membranes for Separation and Abatement of Contaminants from Drinking Waters and Wastewaters

Candidate: **Fabício Eduardo Bortot Coelho**

Supervisor: Prof. **Giuliana Magnacca**

Co-supervisor: Dr. **Victor M. Candelario**

Jury Members: Prof. **Vittorio Boffa**
Aalborg University
Department of Chemistry and Bioscience

Prof. **Luigi Rizzo**
University of Salerno
Department of Civil Engineering

Prof. **Maria Cristina Paganini**
University of Torino
Department of Chemistry

Head of the Doctoral School: Prof. Alberto Rizzuti
PhD Programme Coordinator: Prof. Bartolomeo Civalleri

Torino, 2021

To my grandparents

*“Nothing in life is to be feared, it is only to be understood.
Now is the time to understand more, so that we may fear less.”*

Marie Skłodowska Curie

INDEX

INTRODUCTION.....	1
1. PHOTODEGRADATION OF HUMIC ACID USING Ce-ZrO₂ CATALYST.....	8
1.1. Introduction	8
1.2. Materials and Methods	8
1.2.1. Synthesis and characterization of photocatalysts	8
1.2.2. Photocatalytic Experiments	9
1.3. Results and Discussion.....	10
1.3.1. Characterization of Photocatalysts	10
1.3.2. Adsorption Isotherms	13
1.3.3. Photocatalytic Activity	16
1.3.4. Spectral and TOC Changes in Treated HA Solutions	22
1.3.5. Effect of Scavengers—Photocatalytic Mechanism	23
1.4. Conclusions	25
1.5. Annex 1	26
2. PHOTOCATALYTIC REMOVAL OF Cr(VI) USING IMMOBILIZED Ce-ZrO₂.....	29
2.1. Introduction	29
2.2. Materials and Methods	31
2.2.1. Synthesis and characterization of the Ce-ZrO ₂ photocatalyst.....	31
2.2.2. Photocatalytic Experiments.....	32
2.3. Results and Discussion.....	34
2.3.1. Suspended Ce-ZrO ₂ nanopowder	34
2.3.2. Immobilized Ce-ZrO ₂	41
2.4. Conclusions	46
3. ZrO₂/SiC ULTRAFILTRATION MEMBRANE	48
3.1. Introduction	48
3.2. Materials and Methods	49
3.2.1. Powder characterization and dispersion studies.....	49
3.2.2. Membrane fabrication	50
3.2.3. Membrane characterization and testing.....	51
3.3. Results and Discussion.....	53
3.3.1. Characterization of ZrO ₂ powder and SiC support	53

3.3.2. Optimization of the suspension	55
3.3.3. Membrane coating and sintering	57
3.3.4. Characterization of the membrane	63
3.3.5. Olive oil recovery (Oil/water separation).....	65
3.3.6. Corrosion.....	68
3.4. Conclusions	70
3.5. Annex 2	71
4. Ce-ZrO₂/TiO₂ PHOTOCATALYTIC MEMBRANE	77
4.1. Introduction	77
4.2. Materials and Methods	77
4.2.1. Membrane fabrication	77
4.2.2. Membrane characterization	79
4.2.3. Photocatalytic tests.....	80
4.3. Results and Discussion.....	82
4.3.1. Characterization of the Zr/Ti sols.....	82
4.3.2. Optimization of the coating.....	86
4.3.3. Characterization of the membrane	88
4.3.4. Photocatalytic activity	90
4.3.5. Anti-fouling properties	93
4.4. Conclusions	96
4.5. Annex 3	97
5. CONCLUSIONS.....	100
6. REFERENCES	102
7. APPENDIX A: PUBLICATIONS.....	121
8. APPENDIX B: PERIODS ABROAD	122
9. APPENDIX C: DIDACTIC WORK.....	122
ACKNOWLEDGMENTS	128

INTRODUCTION

Water is the most precious resource in the world. It is essential in every aspect of life and economy [1]. A global water crisis is on course since water demand and pollution keep increasing while many people still do not have supply of clean water [2], especially with the uncertainties of climate change [3]. In addition, a class of recalcitrant pollutants, previously undetected and thereby unregulated for many years [4], represents a great risk to human health. They are called contaminants of emerging concern (CECs) and are usually present in low concentrations, including pharmaceuticals, pesticides, veterinary drugs, flame retardants, personal care, and household products [5]. CECs have potential harmful human and ecotoxicological effects, such as the endocrine disruption caused by bisphenol A and nonylphenol [6]. Additionally, at the wastewater treatments plants (WWTPs), traditional treatments such as activated sludge and sand filters, may not be efficient in fully eliminating many of these compounds [4]. In this way, tertiary treatments should be designed targeting specifically the CECs removal. Among these treatments, Advanced Oxidation Processes (AOP), such as ozonation, have been successfully applied in the degradation of numerous pollutants in drinking and waste waters treatment plants [7–9]. AOPs generate reactive oxygen species (ROS), such as hydroxyl radicals ($\bullet\text{OH}$), which are strong oxidants able to degrade refractory pollutants into inorganic molecules [10]. Among several AOP, Fenton process is an efficient Fe-catalysed decomposition of oxidant H_2O_2 into $\bullet\text{OH}$ [34], while photocatalysis is based on the generation of ROS upon light absorption by a semiconductor catalyst [22,35]. In the photo-Fenton process, the organics degradation is enhanced by light irradiation, which promotes the catalyst regeneration by the photo-reduction of Fe^{3+} to Fe^{2+} [34]. Another approach is to use photocatalysis to generate H_2O_2 and promote the Fenton reaction by adding Fe^{+2} to the system [36]. Besides the AOP advantages, these processes may have their selectivity and efficiency affected by the presence of organic matter and inorganic salts in the water matrix [4,11].

Considering the foregoing, the world urges for sustainable, cost-effective, and reliable methods for drinking water purification and wastewater treatments [12,13]. In this way, membrane filtration attracts great attention due to its high throughput and high quality permeate [14], which made this technique applied in several processes such as wastewater treatment and drinking water production [15]. Compared to traditional technologies, membrane filtration has many advantages such as little or no chemical requirement, ease of operation, and modular construction, allowing its easy upscale [16,17]. However, there are still some challenges to overcome, such as membrane fouling and elevated energy consumption in nanofiltration (NF) and reverse osmosis (RO) systems [18].

Polymeric membranes have been dominant in water treatment [19] but their poor long-term stability limits their application [1]. On the other hand, ceramic membranes present excellent mechanical, chemical, and thermal properties compared with traditional polymeric membranes [20], which allows them to operate in a wide range of pH, elevated temperatures, and with organic solvents. Moreover, these membranes can be backwashed and regenerated under harsh cleaning conditions, resulting in a longer lifetime and lower costs [1,21]. Furthermore, the higher hydrophilicity and porosity of ceramic membranes result in higher fluxes at low pressures and lower fouling tendency compared to the polymeric ones [19,22,23]. Therefore, ceramic membranes are technically suitable for challenging water purification processes [24] and harsh environments [25] in order to be applied, for instance, to textile, metallurgy, and pharmaceutical wastewater treatment, humic-rich surface water purification [26], oil/water separation, food and beverage industry [27], corrosive feeds [28], and aggressive solvents [24].

Ceramic membranes can be divided in two groups, isotropic and asymmetric. When the separation layer cannot be distinguished in the direction of the membrane thickness, the membrane is symmetric or isotropic [19]. These membranes have a homogenous composition being made of a single material. On the other hand, asymmetric membranes consist of a coarse support covered by one or more intermediate layers with decreasing pore size, as shown in **Fig. 1**. The top layer usually is a denser active layer, responsible for the separation [25,29]. The support and intermediate/top layers can be made of the same material, or they can have different compositions, which is usually typical of asymmetric composite membranes.

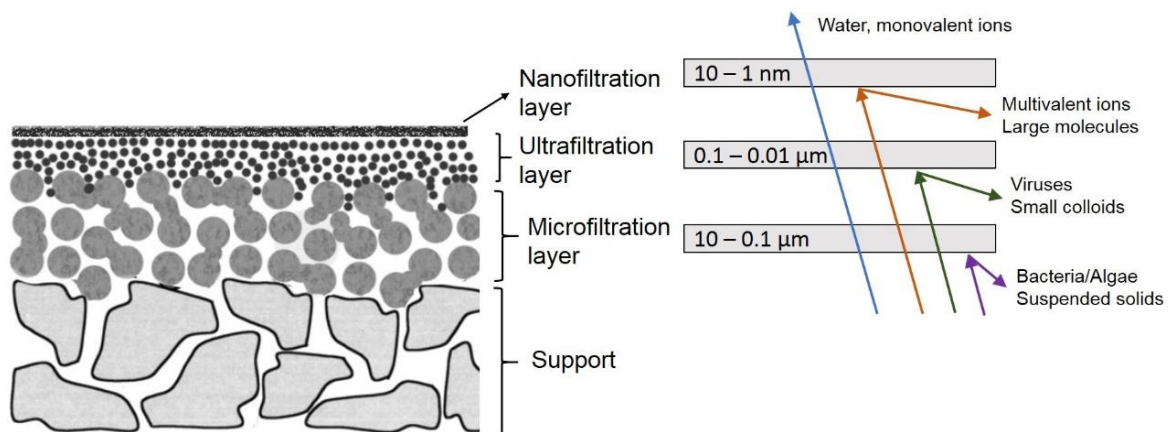


Fig. 1. General structure of asymmetric ceramic membranes showing the correspondence between each layer pore size with their retention properties and application range.

Traditionally, ceramic membranes applied in filtration processes are made mainly of alumina (Al_2O_3), silica (SiO_2), zeolite, mullite, and other oxide mixtures [19,27], because these materials have good cost-effectiveness, homogeneous pore size distribution, and flexibility to tailor the required porosity [30]. Nevertheless, the practical application of these membranes has a

limitation, mainly because of the insufficient chemical and thermal stability of SiO_2 and Al_2O_3 under corrosive and aggressive conditions such as very low or high pH and hydrothermal environments [31,32]. For these reasons, the development of new membranes based on refractory materials, such as zirconium dioxide and silicon carbide, are of ultimate relevance.

Zirconia (ZrO_2) is a promising material for membrane applications owing to its several advantageous properties. First, it can work at high temperatures [18], being applied for hot gases separations, membrane reactors, and solid-state fuel cells. Second, it has a high chemical stability that makes it suitable for conditions where silica and alumina membranes fail [33–35], especially in strong alkaline media [36], allowing severe cleaning and disinfection of ZrO_2 membranes [37]. Third, zirconia has a high hydrophilicity [21,33], which leads to membranes with high water fluxes and low fouling tendency during water treatments [1]. Considering these properties, the use of ZrO_2 membranes in macrofiltration (MF) and ultrafiltration (UF) processes have been demonstrated in several pilot-scale studies for wastewater treatments [33], oil-water separation [38,39], and filtration in the presence of aggressive solvents, high salinity, radioactive [28] and heavily contaminated feeds [24,40], and under hydrothermal conditions [31].

Besides zirconia advantageous properties, fabricating membranes with this material presents some challenges that hinder its development, such the difficulty in obtaining a defect-free active layer with small pores [34]. Avoiding cracks in the top layers is quite challenging as it is closely related to the phase transformations experienced by zirconia during the membrane fabrication process. Pure ZrO_2 , in fact, presents three crystalline forms: monoclinic, tetragonal, cubic. The change from tetragonal to monoclinic phase occurs around 1173 °C, while the symmetric cubic phase forms at temperatures above 2370 °C [18,36], and the phase transition from monoclinic to tetragonal zirconia implies large volume variation of the crystalline cells (~4-9 %) which causes crack formation during the sintering at high temperature necessary for membrane fabrication.

In order to avoid the cracks, the tetragonal or cubic polymorphs are stabilized by doping zirconia with yttria (3-10 %mol Y_2O_3), calcium oxide (12–13 mol% CaO), magnesium oxide (MgO), or rare-earth oxides (8–12 mol%), such as Yb_2O_3 , Nd_2O_3 , and Sm_2O_3 [41]. Among all, the most commonly used material, yttria stabilized zirconia (YSZ), is known for its high strength and fracture toughness [42], combined with an elevated corrosion and temperature resistance, even under hydrothermal conditions[31], being adequate for gas separation [43], pervaporation [44], solvent filtration [45], and highly acid or basic feeds [46].

Although extensive studies have been performed on the preparation of zirconia layers, most of them are supported by alumina [16,38,40,47–51], which does not possess the required chemical and thermal stability, limiting their application [31]. A corrosion-resistant support could be

obtained with silicon carbide (SiC), a great alternative to traditional materials [52–54], since it presents excellent chemical and thermal stabilities in extreme conditions, such as strong alkaline media or high temperature (600-800 °C) environments [55]. Furthermore, SiC shows low thermal expansion coefficient, high thermal conductivity and super-hydrophilic properties with a water contact angle below 5° [12,56], implying low fouling tendency and high permeate fluxes in wastewater treatment [57]. Even though SiC emerged as an excellent porous support among other ceramic materials [22,58–60], it is not suitable for UF applications, since pure silicon carbide membranes usually have pore sizes higher than 0.1 µm [13,55,61]. Concerning these aspects, an asymmetric composite membrane, in which a ZrO₂ UF selective layer is coated on a macroporous SiC substrate, should have the chemical resistance and the water permeability suitable for producing a high-performance membrane.

If the choice of the materials can improve the stability of the membranes, membrane technology still has a drawback that needs to be solved for its full development [62–64]: membrane fouling reduces the system performance and the lifespan of the membrane, increases operation costs, and decelerates the scale-up to industrial applications [62,65–68]. Fouling is characterized by the reduction of the permeate flux or increase of the transmembrane pressure as a result of the blockage of the membrane pores [69]. The major causes of fouling are the adsorption of feed solutes, the deposition of particles, the gel formation, and the bacterial growth (biofouling) [69,70]. In surface waters and wastewaters filtration, fouling is caused mainly by the presence of organic compounds [66], which can be dyes, surfactants, oil, and phenolic compounds [27,39,71], or natural organic matter (NOM), such as humic and fulvic acids [8,66,72]. When the dissolved matter is adsorbed onto the membrane surface and/or in the pores, it is considered an irreversible fouling [73], which usually requires chemical cleaning for recover the original flux of the membranes [74].

Many strategies were adopted for fouling prevention, some of them related to operation conditions (e.g. backwashing, pre-treatment of the feed, critical flux, and high cross flow velocity [8,69,75]), and others focused on the membrane modification, such as functionalization with polymers [76], nanoparticles [64], and catalysts [27,77]. This functionalization could act by two different mechanisms. Traditionally, it was applied to modify the charge and hydrophobicity of the membrane surface, preventing the adsorption/adhesion of fouling substances [17,64,72,78–80]. In a more recent approach, membrane functionalization can add a catalytic layer, which is responsible for the degradation of organic compounds, which prevents the fouling [81]. Among the catalytic process available, photocatalysis is one of the most promising one thanks to the possibility of using solar light and the for the high mineralization efficiency, which ideally produces carbon dioxide, water, and inorganic mineral ions as final products [82].

Recently, great achievements have been reported for photocatalytic ceramic membranes with not only anti-fouling and self-cleaning properties [83–86] but also serving additional functions, such as disinfection [84] and pollutant degradation [87]. Mendret et al. [85] observed that UV irradiation prevented flux decline in the filtration of the dye Acid Orange 7 with their photocatalytic $\text{TiO}_2/\text{Al}_2\text{O}_3$ membrane (pore size smaller than $0.2\ \mu\text{m}$) prepared by a sol-gel route. However, in their work and in many others reported in the literature [87–89], the photocatalytic layer was not responsible for the separation process because the catalyst particles were only stably immobilized on the membrane. This is explainable considering the challenges to overcome in fabricating a homogeneous and defect-free separation layer with small pore size without losing the catalytic activity of the employed material [90]. Even though, several authors were able in fabricating ceramic membranes in which the top layer actually acted as photocatalytic and separation layer [71,83–86,91], for instance, Manjumol et al. [90] developed an Al- TiO_2 ultrafiltration membrane with pore size around 11 nm able in separating and degrading methylene blue under UV light irradiation. In their study and in the majority of the reports, the active layer was deposited on macro/mesoporous alumina supports [71,83–92], but, as already mentioned, they suffered insufficient chemical and thermal stability to operate under corrosive and aggressive conditions such as very low or high pH values [31,32,36].

Even though titanium dioxide (TiO_2) is the most studied and widely applied photocatalyst [10,88,93], its application in pure TiO_2 membranes is very limited, due to the reduction of porosity and cracks formation caused by the partial anatase to rutile phase transformation that occurs upon sintering at temperatures higher than $350\ ^\circ\text{C}$ [89]. To overcome these drawbacks, a mixed $\text{TiO}_2/\text{ZrO}_2$ oxide was chosen as catalyst for fabricating a new photocatalytic membrane. In fact, it is known that in a Ti-doped zirconia, the tetragonal phase of ZrO_2 is partially stabilized and its crystallisation temperature increases up to $550\ ^\circ\text{C}$ [94], which prevents crack formation and loss of porosity during membrane sintering [95], allowing the formation of a homogeneous separation layer with smaller pore size and higher catalytic activity than those exposed by the pure oxides [89,96,97].

In addition, pure titania requires photons in UV frequencies to promote the electron-hole charge separation (i.e., excitation from the Valence band (VB) to the Conduction band (CB), separated by about 3.2 eV): this practically excludes the possibility of using sunlight as an energy source for pristine TiO_2 . To overcome this limitation, several modifications of TiO_2 have been studied, such as its doping with transition-metal ions [98], non-metal atoms [99], or supported metal nanoparticles having plasmonic effects [100]. Also coupling two different semiconductors resulted successful [101]. All these systems constitute the second-generation photoactive materials based on titanium dioxide. On the other hand, semiconductors with higher band gap values imply

higher electrochemical potentials of excited electrons and holes, which can lead to more effective photocatalytic activity [102]. Therefore, the continuous pursuit of active photocatalysts that work under visible light has addressed the research to the development of a third generation of materials not based on TiO₂ [15,103]. Zirconium dioxide has been rarely applied in photocatalysis because of its wide band gap (ca. 5.0 eV), although some reports are available concerning photo-oxidation of chemicals [104–106] and water photosplitting [107]. On the other hand, the band energy levels of ZrO₂ are suitable for photocatalytic applications because the lowest potential of the CB is -1.0 V (vs. normal hydrogen electrode (NHE), pH 0), much more negative than that of TiO₂ anatase (-0.1 V), whereas the highest potential of the VB is +4.0 V, more positive than that of TiO₂ (+3.1 V). Therefore, ZrO₂ energetic photo-induced electrons and holes are able to generate reactive oxygen species (ROS), with a great potential to degrade organic compounds or to oxidize directly the organic molecules [108]. Recent works from our group [108,109] demonstrated doping ZrO₂ with cerium can introduce intra band gap states between zirconia VB and CB, allowing the new catalyst to absorb visible light through a double jump mechanism. These findings were relevant, since they indicated that solar light could be used as light source for the cerium-doped zirconia (Ce-ZrO₂) photocatalytic degradation of organic compounds [102,110]. Such process could then be applied in the control of fouling by degrading organic fouling molecules, such as humic like substances, but also degrading contaminants of emerging concern, which would have important environmental implications.

The main purpose of this thesis is to develop a new photocatalytic membrane, based on cerium-doped zirconia (Ce-ZrO₂) on macroporous silicon carbide (SiC) supports, with improved anti-fouling and self-cleaning properties as well as able to remove contaminants of emerging concern. Considering that no preceding study has specifically explored the fabrication of photocatalytic membranes on SiC supports, the present work is highly innovative and with a potential impact on membrane technology and water treatment field.

This thesis is organized in 4 chapters, as schematised in **Fig. 2**.

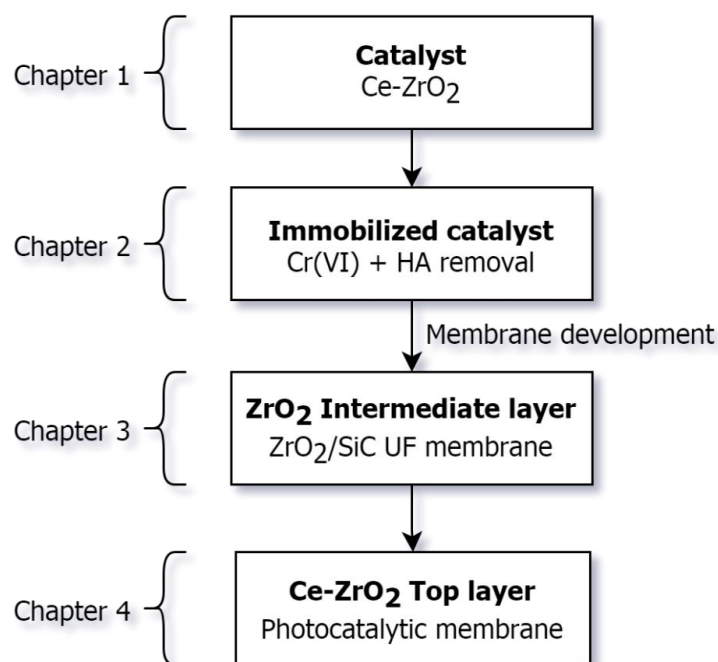


Fig. 2. Flow chart of the thesis structure.

In the first chapter, prior to the fabrication of the photocatalytic membrane, it is evaluated whether the Ce-ZrO₂ catalyst is efficient in the degradation of humic acid (HA), a model foulant for natural and waste waters. In order to test that aspect, the catalyst synthesis conditions and the mechanism of HA photodegradation using the catalyst as a suspended nanopowder were investigated. In the second chapter, the immobilization of the catalyst on a support and whether the catalyst activity was affected by the immobilization process were discussed. For that purpose, the removal by photoreduction of Cr(VI) from galvanizing industry effluent using immobilized photocatalyst Ce-ZrO₂, in the presence of HA, was described. In chapter three, own to the large pores of the silicon carbide support chosen to fabricate the photocatalytic membrane, a zirconia intermediate layer was firstly deposited on the SiC support. With that, a novel ZrO₂/SiC ultrafiltration membrane was obtained, fully characterized and tested under real application conditions in the oil/water separation. In the fourth and last chapter, the preparation of the Ce-ZrO₂ photocatalytic membrane by a sol-gel technique on the ZrO₂/SiC matrix was studied. Several parameters were investigated for optimizing the catalytic layer of the photocatalytic membrane. The retentions of several compounds of interest were measured. Next, the membrane was tested in the degradation of HA and phenol, as well as in the prevention of fouling in the HA filtration under simulated solar light.

1. PHOTODEGRADATION OF HUMIC ACID USING Ce-ZrO₂ CATALYST

Part of the work described in the present chapter has been previously published in:

Bortot Coelho, F.E.; Gionco, C.; Paganini, M.C.; Calza, P.; Magnacca, G. Control of Membrane Fouling in Organics Filtration Using Ce-Doped Zirconia and Visible Light. *Nanomaterials* **2019**, *9*, 534. <https://doi.org/10.3390/nano9040534>

1.1. Introduction

Ceramic membranes fabricated with photocatalyst materials present not only anti-fouling and self-cleaning properties but also serve multiple functions such as degradation of pollutants and disinfection [27,111]. Traditionally, titanium dioxide (TiO₂) has been the most studied and widely applied catalyst [10,88,93] due to its unique photocatalytic activity and stability [112].

In the present chapter, it was studied the photodegradation of humic acid using the catalyst Ce-doped ZrO₂, synthesised by hydrothermal and sol-gel processes. The nanopowders obtained were then characterized in terms of crystal structure, morphology, surface area, porosity, surface charge, light absorption, photo-induced charge separation, and ROS generation. Next, batch experiments were performed in order to evaluate the photocatalytic activity of the Ce-ZrO₂ nanoparticles dispersed in humic acid aqueous solutions under visible light irradiation. Adsorption isotherms were determined and the effects of several parameters (e.g., HA concentration, catalyst dosage, and pH) on HA removal were investigated. Langmuir-Hinshelwood model was used for kinetic modeling. The changes in spectral properties and in total organic carbon (TOC) were analyzed, confirming that HA is actually degraded during the photocatalytic process. Finally, a mechanism for the HA photodegradation is proposed.

1.2. Materials and Methods

1.2.1. Synthesis and characterization of photocatalysts

In the present work, hydrothermal and sol-gel processes were evaluated in order to prepare zirconia doped with 0.5% molar of cerium. In the hydrothermal synthesis, an aqueous solution 1.0 M of ZrOCl₂·8H₂O (CAS 13520-92-8, purity>98%, Aldrich) and 0.005 M Ce(SO₄)₂ (CAS 13454-94-9, essay>99,9%, Aldrich) were mixed and kept under stirring at room temperature. Then, the pH was adjusted to 11 by using an aqueous solution 4.0 M of NaOH. The resulting solution and the precipitates were then transferred into a 125 mL Teflon-lined stainless steel autoclave, 70% filled, which was heated at 175 °C for 15 h in an oven. The precipitates were hence centrifuged and washed three times with deionized water, then dried at 70 °C. This sample was labelled as Ce-

ZrO₂-HYD. For the sol-gel synthesis, 5 mL of zirconium propoxide Zr(OC₃H₇)₄ (CAS 23519-77-9, 70% wt., Aldrich) were mixed with 5 mL of 2-propanol. Then, 28 mg of Ce(NH₄)₂(NO₃)₆ (CAS 16774-21-3, purity > 98.5%, Aldrich), dissolved in 5 mL of double distilled water, were added to the first solution to start hydrolysis. The resulting gel was kept overnight at room temperature and then dried at 80 °C. After aging at room temperature for 10 days, the xerogel was calcined in a muffle furnace at 500 °C in air for 4 h. This sample was labelled Ce-ZrO₂-SG. For comparison, pure zirconia samples were prepared by the same hydrothermal and sol-gel procedures, without the addition of cerium, and named ZrO₂-HYD and ZrO₂-SG, respectively. All aqueous solutions were prepared using ultrapure water Millipore Milli-Q™. All chemicals were used without further purification.

Powder X-rays diffraction (XRD) patterns were obtained with a PANalytical PW3040/60 X'Pert PRO MPD, operating at 45 kV, 40 mA, with a Cu K α radiation source ($\lambda = 1.5418 \text{ \AA}$) and a Bragg Brentano geometry over the range $10^\circ < 2\theta < 80^\circ$.

Nitrogen adsorption-desorption isotherms were obtained (Micromeritics ASAP 2020) for the determination of surface area, using the Brunauer-Emmett-Teller (BET) model, and pore size distribution, using BJH model applied on the desorption branch of the isotherms. Prior to the adsorption run, all the samples were outgassed at 150 °C for 8 h.

Diffuse Reflectance Spectroscopy (DRS) data were recorded in the 200–800 nm range using a Varian Cary 5000 spectrometer, coupled with an integration sphere for diffuse reflectance studies, using a Carywin-UV/scan software. A sample of PTFE with 100% reflectance was used as the reference. The optical band gap energy has been calculated from the Tauc plot.

Zeta potential measurements were performed on a Zetasizer Nano ZS (Malvern Instrument) using principles of laser Doppler velocitometry and phase analysis light scattering (M3-PALS technique). 0.1% *w/v* suspensions of nanoparticles were prepared with a NaCl 0.01 M aqueous solution and ultrasonicated for 10 minutes before the analysis.

1.2.2. Photocatalytic Experiments

Humic acid solutions were prepared dissolving humic acid sodium salt (CAS 68131-04-4, Sigma Aldrich, MP > 300 °C) and then adjusting the pH to the desired value using aqueous solutions of NaOH and HCl.

For the determination of the adsorption isotherms, the zirconia powder was added to the HA solutions and the pH was then adjusted to 6.5. Then, the mixture was kept stirring in the dark for 24 h. The initial humic acid concentration ($[HA]_0$) was varied between 5 and 20 mg.L⁻¹ and the zirconia dosage between 0.1 and 1.0 g.L⁻¹.

In the photocatalytic experiments, a specific amount of the zirconia nanoparticles was added to the HA solution in order to achieve the desired catalyst dosage. As a reactor, it was used 100 mL borosilicate glass beaker. The pH was then adjusted to the desired value. Prior to irradiation, the mixture was kept under string in the dark for 3 hours in order to achieve HA adsorption equilibrium. Then, the mixture was irradiated with visible light for more 3 h under stirring, without any injection of gas. Samples were collected in specific intervals of time. The source of light was a home-built apparatus, consisting of a series of red-green-blue (RGB) LEDs disposed in a cylindrical support (diameter 11 cm), in which the beaker with the suspension was placed in the center of the cylinder. The LEDs emission spectrum is composed of tree peaks with maximum intensities around 455, 530, and 625 nm, all in the visible range. The total power of the system was 20 W and the irradiance at the center of the cylinder was 30 W.m^{-2} (measured with the HD 2302.0 Light meter, Delta OHM). Next, for determining the HA concentration in the solution, the samples were centrifuged at 11,000 rpm for 10 min. The UV-Vis spectra of the supernatants were then recorded using the spectrophotometer UVIKON 930 (Kontron Instruments), in the wavelength range of 200–700 nm. The concentration of humic acid was then calculated by the UV absorbance at 254 nm. This method has been extensively applied for determining the HA concentration [81,113–116] and it can be correlated to total organic carbon (TOC) value through a calibration curve [117,118]. TOC measurements were carried out with a Shimadzu TOC-V_{CSH} Total Organic Carbon Analyzer, equipped with an ASI-V auto-sampler, and fed with zero-grade air. The TOC was determined as the difference between total carbon (TC) and inorganic carbon (IC).

The stability of Ce-ZrO₂-SG nanoparticles was investigated in multiple HA photodegradation cycles. For that, after each 180 min cycle, a concentrated HA solution was added in order to achieve the initial HA concentration and keep the same initial catalyst dosage (1 g.L^{-1}). Then, the dispersion was irradiated again for another 180 min. No treatment, such as washing or centrifugation, was performed between the cycles.

1.3. Results and Discussion

1.3.1. Characterization of Photocatalysts

In agreement with previously reported characterization procedure [102,108,109,119,120], the structure of the resulting phases, obtained via both syntheses, is a mixture of monoclinic and tetragonal ZrO₂ (**Fig. A1.1**). In both pure and doped oxides, the monoclinic phase presents some degree of anisotropy, as suggested by the variable width of the diffraction peaks [109,120]. None

of the samples shows the presence of diffraction peaks related to the formation of CeO₂ phases, indicating that cerium was successfully inserted in the ZrO₂ matrix.

Table 1.1. Specific surface areas (S_{BET}) of pure and Ce-doped zirconia samples.

Sample	S_{BET} [m ² .g ⁻¹]
ZrO ₂ -HYD	44 ± 4
Ce-ZrO ₂ -HYD	49 ± 5
ZrO ₂ -SG	150 ± 15
Ce-ZrO ₂ -SG	70 ± 7

In order to investigate the surface area and porous structure of the doped zirconia samples, nitrogen adsorption/desorption analyses were performed. The BET method was used to determine the specific surface areas of the samples (reported in **Table 1.1**). As shown in **Fig. 1.1**, both samples show type IV IUPAC isotherms with a hysteresis loop type *H3* (typically observed in aggregates of plate-like particles giving rise to slit-shaped pores) in the relative pressure (P/P_0) range of 0.8–1.0, which indicates the presence of large mesoporosity. However, it is quite probable that this porosity is due to void space given by interparticle porosity, given by aggregation of primary particles [121,122] rather than intraparticle porosity. The explanation relies on the fact that to accommodate so large pores, bigger particles are required, which are not present in the samples, as suggested by the crystallite size (10–20 nm of diameter) and TEM images obtained in a previous work [108]. Regarding the specific surface area, the doped zirconia prepared by sol-gel synthesis exhibits a higher S_{BET} than the hydrothermally synthesized sample (**Table 1.1**), whereas the addition of Ce does not cause a substantial modification in the morphology of HYD sample but causes a decrease of the specific surface area of SG sample from 150 to 70 m².g⁻¹.

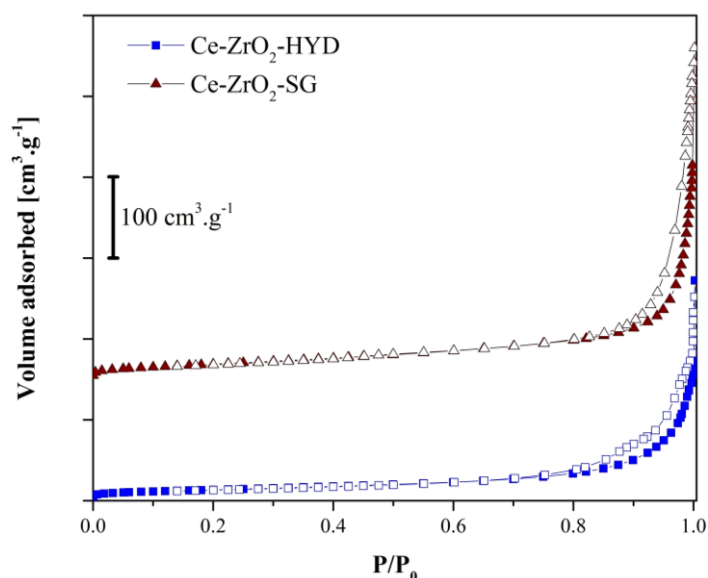


Fig. 1.1. N₂ adsorption/desorption isotherms of Ce-ZrO₂ prepared by sol-gel (SG) and hydrothermal (HYD) processes.

In order to evaluate the surface charge of the Ce-doped zirconia samples in aqueous solutions, since it is closely related to the adsorption properties, the zeta potential of the samples was measured at several pH values, as shown in **Fig. 1.2**. It can be observed that both hydrothermally and sol-gel prepared samples exhibit a negative charge in a wide range of pH (4–9), which indicates that the surface of the zirconia, as expected, is rich in OH groups (vide FTIR spectra, **Fig. A1.2**). The zirconia OH groups can be classified as terminal or bridged; terminal OH is a Brønsted base site, while bridged OH is a Brønsted acid site resulting from the protonation of bridging oxygen ions [123]. Using titration methods, Sahu and Rao [124], observed the prevalence of acid sites on zirconia surface, which explains the highly negative zeta potential values measured in the present work increasing the pH. These authors also stated that distribution of active sites is closely related to the amount of defects, which is mainly affected by preparation methods (e.g., calcination temperature, wet or dry synthesis). This fact can help to understand why the sol-gel prepared Ce-ZrO₂ has less negative zeta potential values than the hydrothermal one. In fact, the last step in the sol-gel process is a calcination at 500 °C, which reduces the amount of OH groups in particles surface.

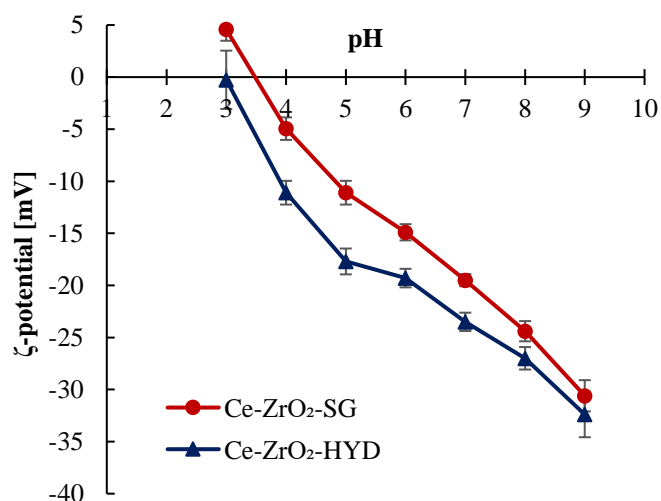


Fig. 1.2. Zeta potential as a function of pH for the Ce-ZrO₂ prepared by hydrothermal (HYD) and sol-gel (SG) processes.

The interest towards these materials in the present paper deals with their optical absorption properties, which were investigated by Diffuse Reflectance Spectroscopy (DRS). As seen in **Fig. A1.3**, the addition of a small amount of cerium dramatically affects the optical properties of the materials, promoting a red-shift in the absorption spectra. An absorption shoulder, centered at ca. 300 nm, with a tail in the visible region is clearly observed in both hydrothermal and sol-gel Ce-doped samples, but it is more pronounced in the hydrothermal sample, as also observed previously [109]. In regards to the band gap transitions, two E_{gap} values were reported, 5.2 and 3.6–3.7 [108,125], the first value associated with the fundamental VB→CB transition of ZrO₂ (unaffected by the Ce doping), the second one due to the absorption band associated to the O 2p→Ce 4f charge transfer transition [119]. Therefore, this result indicates that the prepared Ce-doped oxides have the potential to work as photocatalysts under solar light irradiation.

1.3.2. Adsorption Isotherms

Humic acid is a large molecule (30–50 kDa) with several hydrophilic functional groups, such as COOH and OH, but also with large hydrophobic moieties, some of them consisting of aromatic rings [64]. Given the chemical structure, it can interact very easily and strongly with ceramic materials which are rich of OH groups via ionic, electrostatic and hydrogen bonding. For our purposes, i.e., the study of antifouling materials for ceramic membrane production, humic substances are interesting for at least two reasons, as already discussed in the Introduction section: on one hand several substances present in natural water have structure and behaviors similar to those of humic substances and the study of the fate of these compounds in filtration units can allow to predict how long a membrane can resist the fouling process before the regeneration; on the other

hand, humic substances can mimic the fouling substances found in filters after separation of organic molecule (i.e., pollutants) from aqueous matrices. As the regeneration of a membrane requires time and economic burdens, it would be highly convenient to produce a membrane with antifouling properties, which can be done using a material with no affinity towards fouling substances (hydrophobic), or producing a membrane where the fouling can be removed by irradiation in the presence of a proper photocatalyst. If the photocatalytic material is used to fabricate the membrane, one can imagine producing an antifouling membrane with potentially infinite working time and no necessity of cyclic regeneration. Achieving the objective, the functional membrane prepared will be neither subjected to lack of permeation during use with several advantages for the industrial application of the device.

The photocatalyst we would like to use is the Ce-doped zirconia, whose activation upon visible light irradiation can allow to obtain an integrated system for filtration of pollutants and consequent abatement of the retentate in solar plants.

Since the Ce-doped zirconia nanoparticles are rich in –OH groups (vide FTIR spectra, **Fig. A1.2**), a considerable adsorption of HA into the particles surface is expected, but it is known in the literature that often the adsorption is only the first step to obtain the photocatalytic abatement of the adsorbed substrates [22,44]. In order to evaluate the extent of HA adsorption at the surface of Ce-ZrO₂ nanoparticles, a series of experiments were performed to obtain the related adsorption isotherms (in the dark, pH 6.5, T = 25 ± 3 °C). Then, the Langmuir model, which assumes monolayer adsorption onto a surface containing a finite number of adsorbing sites, and the Freundlich model, which assumes heterogeneous surface energies, were evaluated to fit the experimental data (**Fig. A1.4**). Only the Langmuir isotherm presented a good correlation (R² > 0.99) with the experimental data, therefore the relevant data of Langmuir fit were reported in **Table 1.2**. This can be explained by the fact that HA has a highly negative charge at neutral pH [126]; then, HA is mainly adsorbed in a monolayer rather than in multilayers due to the large electrostatic repulsion between the adsorbed molecules and the molecules to be adsorbed [127]. The Langmuir equation is expressed as:

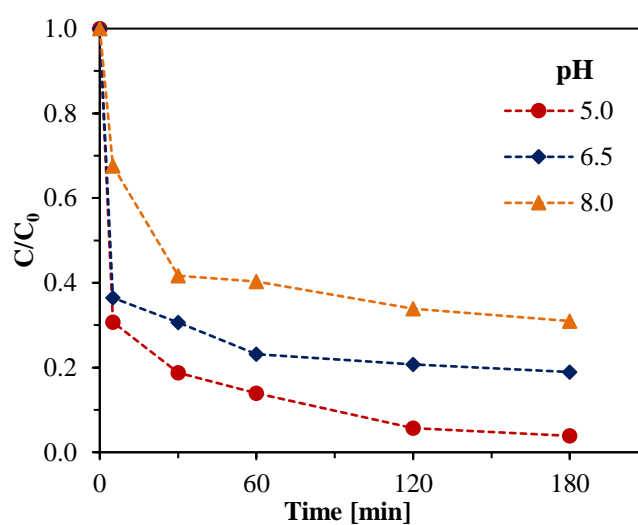
$$\frac{C_e}{q} = \frac{1}{q_e K_L} + \frac{C_e}{q_e} \quad (6)$$

In this equation, C_e is soluble material concentration [mg.L⁻¹], q_e is the adsorption capacity [mg.g⁻¹], q is the adsorption rate [mg.g⁻¹], and K_L is Langmuir equation constant.

Table 1.2. Parameters for the HA adsorption isotherms in the doped zirconia samples.

Sample	Langmuir adsorption model		
	qe [mg.g ⁻¹]	k _L	R ²
Ce-ZrO ₂ -HYD	9.3	0.36	0.998
Ce-ZrO ₂ -SG	12.3	0.74	0.997

From **Table 1.2**, it can be seen that the sol-gel zirconia has a higher HA adsorption capacity than the hydrothermal one. One possible explanation for this fact is the higher specific surface area of the sol-gel zirconia (**Table 1.1**), which implies a higher number of active sites available for the HA adsorption. In addition, the sol-gel prepared ZrO₂ has a lower negative surface charge than the hydrothermal one ($\zeta = -17.2$ at pH 6.5 vs. -21.4 mV); therefore, the repulsion between the negatively charged humic acid and the surface is less intense, favouring the adsorption of HA. To corroborate this statement, it can be shown how the pH affects HA adsorption on Ce-ZrO₂-SG particles (**Fig. 1.3**). At the pH 5.0, the negative surface charge of zirconia is lower (**Fig. 1.2**), which reduces the electrical repulsion by the negatively charged HA molecules, favouring their adsorption. However, it should be noticed that, at pH values lower than 5.5, the solubility of HA decreases considerably [128], which also explains the increased HA apparently adsorbed amount in more acidic solutions. Moreover, in acid medias humic acid molecules may aggregate to the extent of forming micelle-like structures [129]. On the other hand, at higher pH values, humic acid carboxylic and phenolic group deprotonate, increasing HA negative charge [126,129]. Consequentially, the HA repulsion exerted by zirconia nanoparticles is greater.

**Fig. 1.3.** Adsorption of humic acid on Ce-ZrO₂-SG (under dark, T = 25 ± 3 °C, [HA]₀ = 10 mg.L⁻¹, adsorbent dosage = 1 g.L⁻¹).

The values obtained for the maximum adsorption using doped zirconia are in agreement with other adsorbents. A value of 8 mg.g^{-1} have been reported by Ferro-Garcia et al. [130] for a commercial activated carbon. For zeolites, maximum HA adsorption capacity values of 8.7 and 13 mg.g^{-1} have been obtained by Moussavi et al. [131] and Coppola et al. [132], respectively. In comparison with other photocatalysts, Liu et al. [127] obtained an adsorption capacity of 5.9 mg.g^{-1} using zeolite/ TiO_2 particles, whereas Sun and Lee [126] reported 8 mg.g^{-1} for TiO_2 microspheres.

1.3.3. Photocatalytic Activity

In order to evaluate if the prepared zirconia nanoparticles would be able to degrade humic acid in a photocatalytic process, a series of experiments was done with 1 g.L^{-1} of pure and doped ZrO_2 . An experiment without any powder was also performed to check the direct photolysis of HA. Results are shown in **Fig. 1.4**.

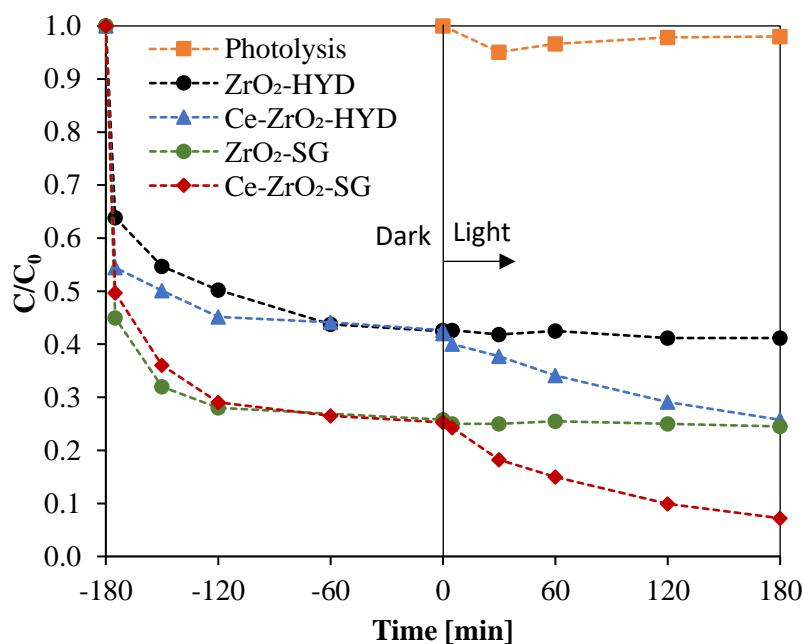


Fig. 1.4. Adsorption and photodegradation of humic acid using different zirconia samples ($[\text{HA}]_0 = 10 \text{ mg.L}^{-1}$, pH 6.5, catalyst dosage = 1 g.L^{-1}).

From this figure, it can be observed that practically no degradation of the humic acid occurs under visible-light irradiation, in agreement with results reported by other authors [113,133]. It can also be noticed that in the presence of pure ZrO_2 , the removal of HA was caused only by adsorption, in fact, after reaching adsorption equilibrium, it was not observed any further removal of HA under irradiation. This result corroborates the ones obtained by DRS and previous EPR characterization [102,108,109,120], since pure zirconia presents a wide band gap value of 5.2 eV, and visible-light irradiation is not able to promote the charge separation. Thus, without photo-

induced electrons and hole, neither the direct oxidation of HA nor the generation of radicals capable of degrading HA are possible. On the other hand, both hydrothermal and sol-gel Ce-doped ZrO₂ adsorb HA under dark but are also able to degrade humic acid under visible light irradiation in a photocatalytic process. As discussed in the previous section, the cerium doping introduces in the oxide an intra band gap state based on the Ce 4f levels. Therefore, using a double jump mechanism, Ce-ZrO₂ can absorb visible light frequencies, promoting charge separation. Then, the photo-induced electrons and holes initiate the HA oxidation reactions. For the Ce-ZrO₂-SG sample, 93% of the humic acid was removed after 180 min of adsorption in the dark followed by 180 min of light irradiation.

1.3.3.1. Effect of the Initial HA Concentration

Considering the potential application of the material, it is important to study the dependence of removal efficiency with the initial humic acid concentration ($[HA]_0$). Depending on the source of water (surface, ground), season, proximity to urban centers, the concentration on organic matter can vary considerably, from few mg.L⁻¹ to more than a hundred. Therefore, the values of initial HA concentration studied were those typically reported in works devoted to advanced oxidation process [21,22,36]. **Fig. 1.5** shows the photocatalytic experiment results starting from different initial HA concentrations using 1 mg.L⁻¹ of the hydrothermally and sol-gel prepared Ce-ZrO₂. It can be observed that HA removal decreases increasing the initial HA concentration, as also observed by other authors [113,114]. The explanation relies on the fact that at higher concentrations, more HA molecules are adsorbed at the zirconia nanoparticles surface, reducing the availability of the sites active for the photocatalytic reaction [114] and also increasing the repulsion for non-adsorbed HA molecules [134]. In addition, the adsorbed coloured HA molecules may also hinder the absorption of light by the zirconia particles, slowing down the degradation rate. It is also possible that, since the same dosage of catalyst was used and consequently the amount of radicals generated was the same, a less concentrated HA solution can be degraded more efficiently in shorter time.

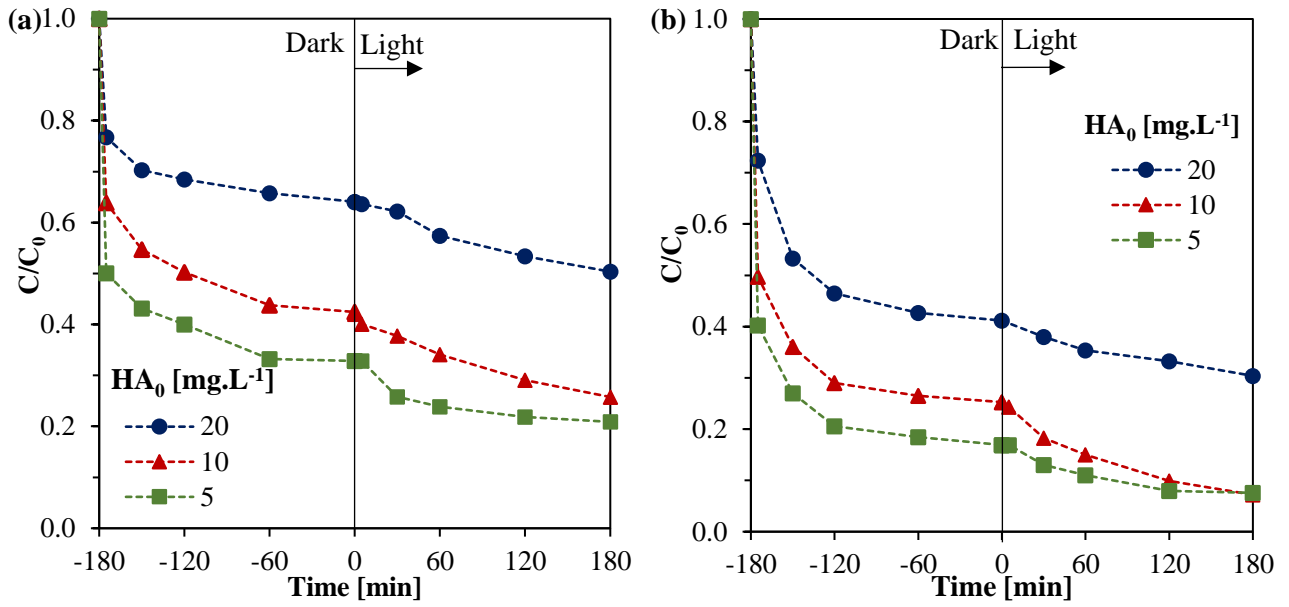


Fig. 1.5. Effect of initial humic acid concentration on HA removal using (a) Ce-ZrO₂-HYD and (b) Ce-ZrO₂-SG (pH 6.5, catalyst dosage = 1 g.L⁻¹).

The kinetic modelling helps to draw conclusion about reaction rates and provides useful rate equations for engineering the development of the system. For photocatalytic reactions, especially in the ones where adsorption represents a critical step in the photo-oxidation processes, Langmuir-Hinshelwood model is the most used one [112,123,135–137]. This model assumes that both oxidant and reducer are rapidly adsorbed and the rate-determining step of the reaction involves these both species present in a monolayer at the solid-liquid interface [138]. The initial reaction rate, r_0 [mg.L⁻¹.min⁻¹], in the Langmuir-Hinshelwood model can be expressed as following:

$$r_0 = \frac{-dC}{dt} = k \frac{K_{ads}C}{1 + K_{ads}C} = k_{obs}C \quad (7)$$

where k is the apparent reaction rate constant [mg.L⁻¹.min⁻¹] and K_{ads} is the adsorption equilibrium constant [L.mg⁻¹]. These constants can be grouped in a lumped parameter in order to obtain a pseudo-first-order kinetic equation, in which k_{obs} [min⁻¹] is the pseudo-first-order rate constant. Upon integration and linearization of equation (7), it is possible to determine k_{obs} by fitting the experimental data (Figure S5). The values obtained are shown in **Table 1.3**. With these values, it is possible to calculate the Langmuir-Hinshelwood constants (**Table 1.3**) by another linear fit (**Fig. A1.6**) using the linearized form of the equation (7), as following:

$$\frac{1}{k_{obs}} = \frac{1}{k}C_0 + \frac{1}{kK_{ads}} \quad (8)$$

Table 1.3. Pseudo-first-order kinetic rate constants (K_{obs}) in photocatalytic experiments with different initial HA concentrations ($[HA]_0$) and the Langmuir-Hinshelwood equation fitted parameters (k , K_{ads}).

Catalyst	[HA] ₀ [mg.L ⁻¹]	k _{obs} [min ⁻¹]	r ²	k [mg.L ⁻¹ .min ⁻¹]	K _{ads} [L.mg ⁻¹]
Ce-ZrO ₂ -HYD	20	0.0023	0.96	0.058	0.24
	10	0.0049	0.97		
	5	0.0053	0.94		
Ce-ZrO ₂ -SG	20	0.0040	0.91	0.099	0.28
	10	0.0097	0.96		
	5	0.0091	0.96		

Wang et al. [113] also applied the Langmuir-Hinshelwood modelling to the photodegradation of humic acid, the composite ZnO-TiO₂-Bamboo charcoal was used as catalyst. These authors reported a value of 0.22 L.mg⁻¹ for K_{ads} , which is in agreement with the value obtained in the present work, and 0.87 mg.L⁻¹.min⁻¹ for the apparent reaction rate, k . Although this value is one order of magnitude higher than that obtained in our experiments, the measured irradiance applied by those authors was 1500 against 30 w.m⁻² in the present work, justifying the results.

Comparing hydrothermal and sol-gel prepared Ce-ZrO₂, the sol-gel sample exhibits higher rate constants (**Table 1.3**) and higher removal of humic acid combining adsorption and photodegradation (**Fig. 1.5**). In addition, several membrane coating techniques derives from sol-gel chemistry [139–142]; therefore, considering a further application of doped zirconia as an anti-fouling layer in filtration membranes, the rest of the study will be focused on the sol-gel Ce-ZrO₂.

1.3.3.2. Effect of the Initial pH

Solution pH is a relevant operational parameter since it governs the protonation/deprotonation of organic compounds and the surface functional groups of zirconia, thus affecting the efficiency of adsorption and photocatalysis [143]. In addition, elevated costs can arise from pH adjustment, which can determine the feasibility of the processes. Therefore, in order to investigate the effect of the pH on the photocatalytic degradation efficiency of HA, it was chosen to work at the values of 5.0, 6.5, and 8.0, which are not so far from neutrality and within the range of natural surface waters [144]. In the experiments it was used 1 g.L⁻¹ of Ce-ZrO₂-SG and an initial HA concentration of 10 mg.L⁻¹; the results, as obtained with a preliminary adsorption carried out

in the dark (adsorption contribution) and with a subsequent irradiation (adsorption + photocatalytic removal), are shown in **Fig. 1.6**.

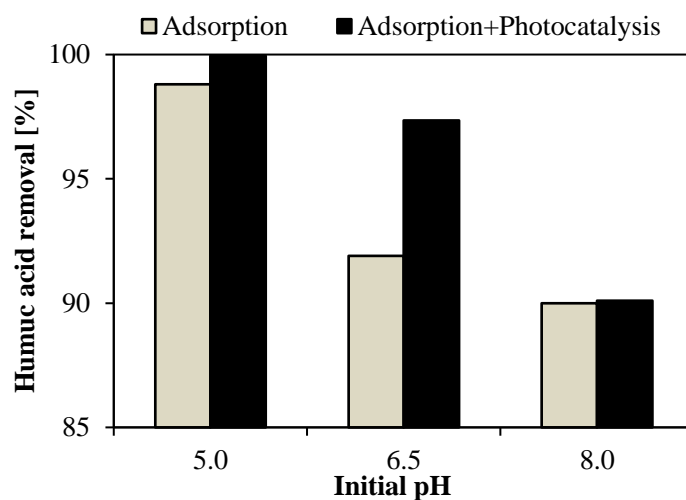


Fig. 1.6. Effect of initial pH on humic acid removal using 1 g.L^{-1} of Ce-ZrO₂-SG catalyst ($[\text{HA}]_0=10 \text{ mg.L}^{-1}$).

It can be observed an increasing trend in HA removal as the acidity increases, in agreement with other works on photocatalytic degradation of HA [113,114,136]. However, it should be noted that HA adsorption at the catalyst surface, which is an important step in the photodegradation process [136], was also higher at lower pH values. As discussed before, the HA adsorption is intensely affected by the solution pH, since in the acid pH range, the solubility of HA decreases considerably while its negative charge decreases. At the same time, the surface charge of zirconia becomes less negative, favoring the HA adsorption. Regarding the photocatalytic activity, for TiO₂ based photocatalysts, it has been reported that, under acidic conditions, the catalyst surface is more conducive for electrons leading to production of a photocurrent [145], which contributes to the generation of reactive oxygen species, and meanwhile avoids the recombination of electrons and holes [136]. Therefore, since adsorption is the dominant mechanism in the HA removal [81], the larger difference between adsorption and adsorption+photocatalysis was obtained at pH 6.5, which was used in the further experiments.

1.3.3.3. Effect of Catalyst Dosage

The influence of the amount of Ce-ZrO₂-SG nanopowder on the photodegradation efficiency is shown in **Fig. 1.7**. The increase of the catalyst dosage leads to an increase of HA removal by both adsorption and photocatalytic mechanisms. Higher doses of catalyst imply higher surface area and number of active sites available, which favors light interaction and HA adsorption [146]. On the other side, it has been reported in some studies, that higher doses of catalyst could

lead to negative effects due to light scattering and agglomeration of nanoparticles [114,146–150]. However, these phenomena were not observed in the catalyst dosage range tested, as the trend of adsorption contribution and adsorption + photocatalytic removal remains the same, possibly because the optimum catalyst dosage was not reached or investigated.

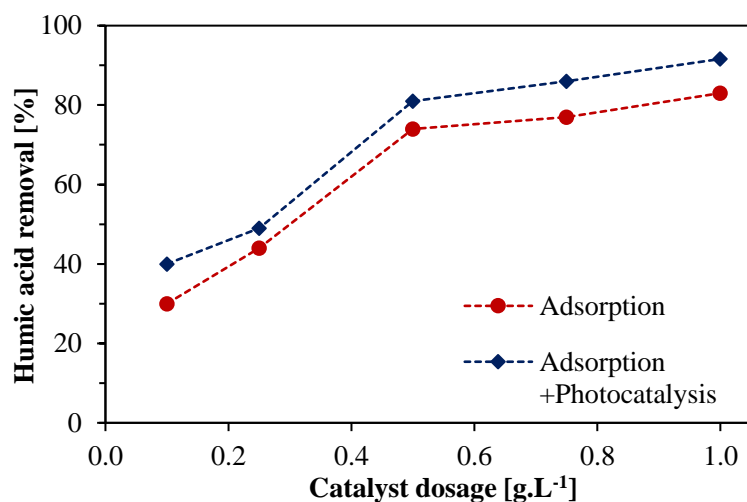


Fig. 1.7. Effect of Ce-ZrO₂-SG catalyst dosage on humic acid removal (pH 6.5, [HA]₀ = 10 mg.L⁻¹).

1.3.4. Stability of Ce-ZrO₂ Photocatalyst

The stability of photocatalyst and its auto-regeneration capacity is critical for its application in controlling fouling in membrane filtration processes. To demonstrate the potential applicability of Ce-ZrO₂ photocatalysts, the stability of Ce-ZrO₂-SG nanoparticles was investigated. **Fig. 1.8** shows the results of HA removal in multiple degradation cycles. It can be seen that there is a loss of performance from the first to the second cycle, but the performance keeps relatively stable from the second to the following two photodegradation cycles. It can be presumed that some HA molecules of high molecular weight and aromaticity are not completely degraded, accumulating in the solution. In addition, unreacted HA molecules, adsorbed on zirconia nanoparticles, can block ZrO₂ active sites and the light absorption. It is worth noting that no treatment, such as washing, was performed between the cycles. At the end of a cycle, a concentrated HA solution was added in order to achieve the initial HA concentration and the dispersion was irradiated again for 180 min. Therefore, these results suggest that Ce-doped zirconia have relatively stable performance as the active sites are regenerated under irradiation.

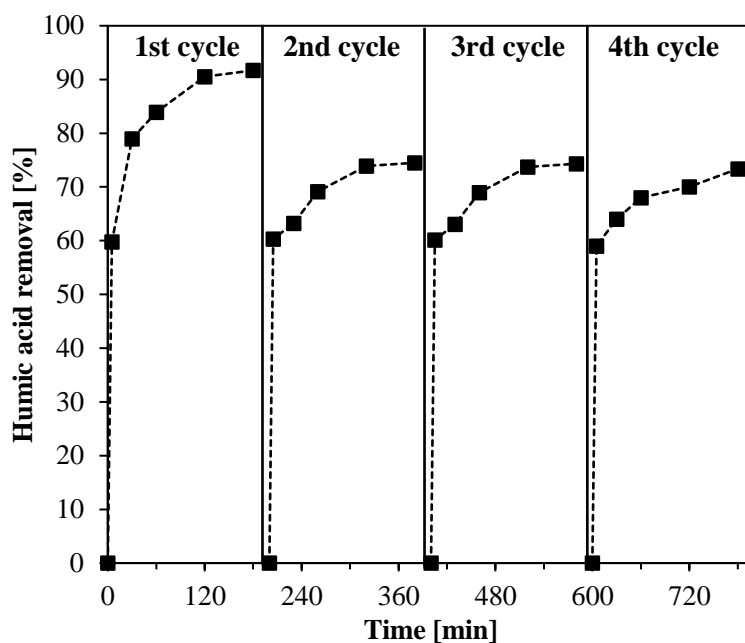


Fig. 1.8. Removal of humic acid in multiple photodegradation tests (Ce-ZrO₂-SG dosage = 1 g.L⁻¹, pH = 6.5, [HA]₀ = 10 mg.L⁻¹).

1.3.5. Spectral and TOC Changes in Treated HA Solutions

In **Fig. 1.9a**, the removal of humic acid, using Ce-ZrO₂ in the dark (adsorption) and under visible light irradiation (Ads+Photocatalysts), is presented in terms of TOC and UV absorption at 254 nm (UV₂₅₄). It is worth noting that both UV₂₅₄ absorbance and TOC values are used to quantify the humic acid, but a mathematical correlation of these two values is required in order to compare directly their absolute values [66]. In addition, the TOC measurements can be considered as preliminary analysis, given the complexity of quantifying the HA by this technique. The determination of a calibration curve and more replicates would be needed to provide more accurate results. Nevertheless, UV-Vis analyses were performed in triplicates and presented with the respective errors bars.

From **Fig. 1.9a**, it can be seen that the TOC reduction is lower than the UV₂₅₄ absorbance reduction, indicating that the HA is probably degraded to intermediates, such as alcohols, aldehydes, ketones and carboxylic acids [118], higher UV radiation absorbing compounds. Nevertheless, comparing the final TOC values, there is a considerable difference in the values of adsorption and photocatalysis, which is an evidence that some degree of mineralization was achieved. These results are in agreement with HA degradation employing as photocatalysts TiO₂/Fe₂O₃/GO [81], TiO₂/ZnO [113], and ZnO [114].

Uyguner and Bekbolet [118], studying the different molecular weights fraction of humic acid after a TiO₂ photocatalytic treatment, verified that the ratio between the absorption in wavelengths 254 and 436 nm (A₂₅₄/A₄₃₆) could be used as an indicative parameter of photocatalytic

degradation: an increase of the ratio was associated to a reduction in the higher molecular weight fractions of humic acid, which have higher aromaticity than the lighter fraction. Therefore, this ratio A_{254}/A_{436} was calculated for the HA photocatalytic degradation with Ce-ZrO₂ and presented in Fig. 1.9b.

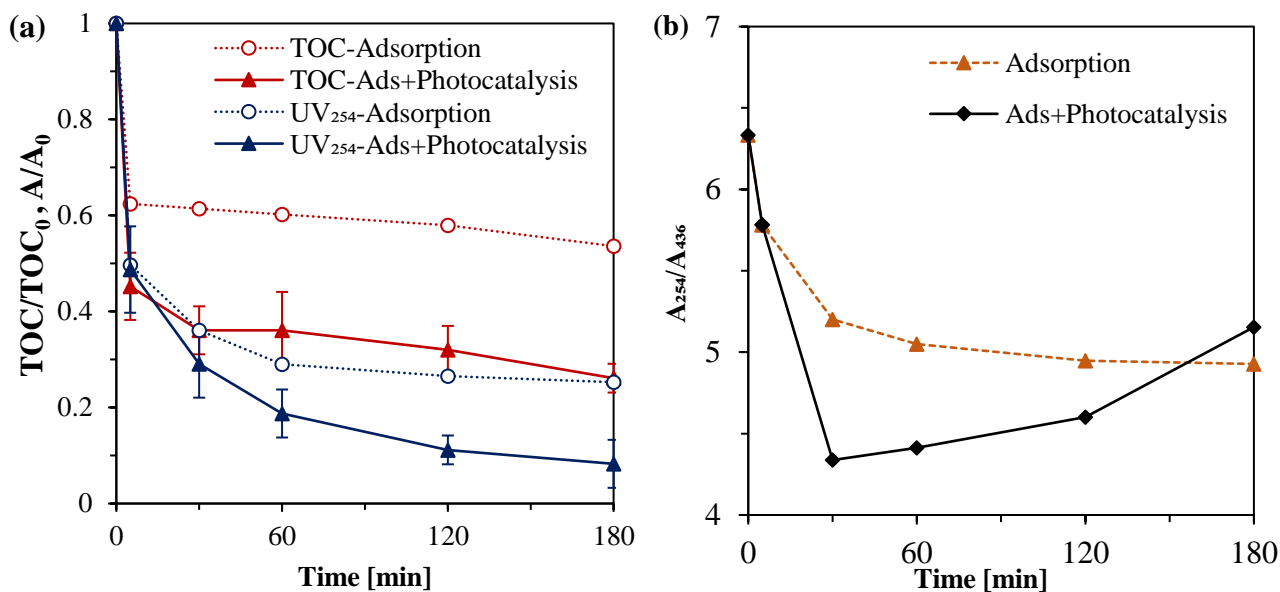


Fig. 1.9. (a) Removal of humic acid in terms of TOC and UV 254 nm absorbance; (b) ratio between UV-Vis absorbance values at the wavelength of 254 and 436 nm (A_{254}/A_{436}) in HA photodegradation tests (Ce-ZrO₂-SG dosage = 1 g.L⁻¹, pH = 6.5, [HA]₀ = 10 mg.L⁻¹).

It can be observed that the ratio A_{254}/A_{436} presents a fast decrease at the beginning of the experiment in the dark, and then it stabilizes because adsorption equilibrium was reached. This indicates that the HA molecules of lower molecular weight are preferentially adsorbed at the zirconia surface, since higher molecular weight fractions have higher aromaticity [118] and thus a more limited interaction with zirconia. Under irradiation, the ratio A_{254}/A_{436} first decreases due to the HA adsorption and then it increases continuously, since HA molecules have been degraded to lower molecular weight compounds.

1.3.6. Effect of Scavengers—Photocatalytic Mechanism

Among the mechanisms proposed for the degradation of organic molecules in photocatalytic processes, two of them have been frequently reported [123,151,152]. In the direct oxidation mechanism, the photo-induced holes oxidize the organic molecule adsorbed on the catalyst. In the indirect mechanism, photo-induced holes and electrons generate reactive oxygen species (ROS), mainly [•]OH radicals, that degrade the adsorbed organic molecule [123,133,151]. In both cases, adsorption of the organic molecule is critical in the photocatalytic degradation, since

photocatalytic reactions proceed at the surface or near the semiconductor surface [123]. In dyes bleaching studies, it is also reported a third mechanism, in which the dye acts as a photosensitizer by adsorbing the light and generating or initiating the reactions of ROS formation [153]. However, this mechanism does not seem probable for the humic acid photodegradation under visible light, considering that HA solutions do not have higher absorption in the visible region. As discussed in previous works [102,108,109,120], EPR studies indicated the generation of photo-induced holes and electrons, and the formation of $\cdot\text{OH}$ radicals when Ce-doped ZrO_2 was irradiated. Hence, in order to elucidate HA degradation mechanism with doped zirconia, a series of experiments were performed with $\text{Na}_2\text{-EDTA}$ (pointed as scavenger for holes [154] and a chelating agent that prevents HA adsorption on the oxide surface [151,155]) and isopropanol (commonly used as scavenger of $\cdot\text{OH}$ radical [155,156]). The results are shown in **Fig. 1.10**.

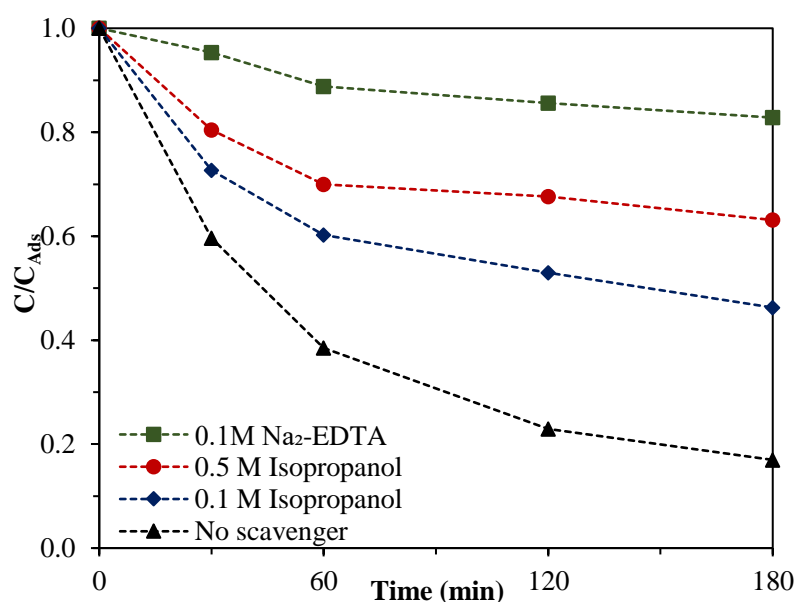


Fig. 1.10. Removal of HA in photocatalytic treatments with and without scavengers. The curves were calculated considering as initial concentration, C_{Ads} , the HA concentration after adsorption equilibrium (Ce-ZrO₂-SG dosage = 1 g.L⁻¹, pH = 6.5, $[\text{HA}]_0 = 10 \text{ mg.L}^{-1}$).

In the presence of $\text{Na}_2\text{-EDTA}$, it can be observed that the photocatalytic degradation of humic acid is highly decreased, since HA molecules are unable to adsorb at zirconia surface to undergo the oxidation reactions. Exhibiting a concentration-dependent effect, isopropanol also reduces the HA photodegradation efficacy by quenching $\cdot\text{OH}$ radicals. Thus, it can be inferred that $\cdot\text{OH}$ radicals are also responsible for the HA oxidation.

Finally, considering previous EPR results [108] and the present observations in the HA degradation, is proposed, in **Fig. 1.11**, a mechanism for the humic acid degradation under visible light irradiation using with Ce-ZrO₂ as photocatalyst. First, in a double jump mechanism, Ce-doped

ZrO₂ adsorbs visible light photons promoting the photo-induced charge separation. Then, zirconia valence band trapped holes (h⁺_(VB)): (a) directly extracting electrons from the adsorbed HA molecules and oxidizing them; and/or (b) reacting with the ⁻OH groups adsorbed on the photocatalyst (⁻OH_(ads)) producing adsorbed [•]OH radicals ([•]OH_(ads)) which successively oxidize HA molecules at the catalyst surface. Finally, in a less likely process, (c) the generated [•]OH radicals are released from the surface to the solution and oxidize HA molecules distant from the photocatalyst surface. Although this possibility was not evaluated in the tests with scavengers, (d) the superoxide anion radical ([•]O₂⁻), generated by photo-induced electrons (e⁻_(CB)), could also degrade the HA.

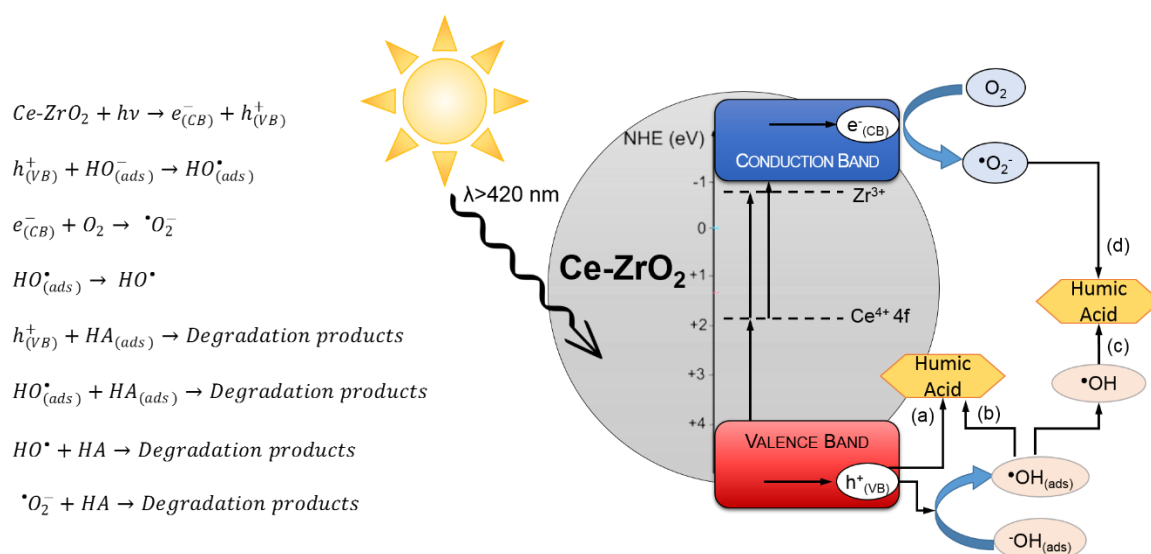


Fig. 1.11. Proposed mechanism for the photodegradation of HA under visible light using Ce-ZrO₂ as photocatalyst.

1.4. Conclusions

Ce-doped ZrO₂ nanoparticles with photocatalytic activity under visible light were synthesized by hydrothermal and sol-gel processes. The addition of a small amount of cerium introduces intra band gap states that act as a bridge between the VB and the CB of zirconia, allowing the absorption of low-energy photons in a double jump mechanism [108,109]. Therefore, a red shift in the absorption spectra is observed, indicating the possibility to use visible light to promote charge separation and the generation of ROS to degrade organic compounds. Thus, this catalyst can be considered a third-generation photocatalyst [157]. Ce-ZrO₂ was then applied in the photodegradation of humic acid, a good model molecule for membrane fouling tests. As a result, it was observed that the photocatalytic process led to the degradation of HA into smaller molecules, as indicated by spectroscopic and TOC changes. Sol-gel prepared Ce-ZrO₂ exhibited the higher HA removal, achieving 93% of efficiency in 180 min of irradiation using RGB LEDs as light

source, after 180 min of adsorption in the dark. Further experiments also confirmed the catalyst activity in neutral pH conditions and its stability for several photocatalytic cycles. The present findings point out to the further development of Ce-ZrO₂ photocatalytic membranes with improved anti-fouling properties. This will be important for new industrial applications of membrane filtration processes, especially for water treatment. In such processes, solar light photocatalysis can be used to degrade organic fouling compounds and possibly contaminants of emerging concern, which would have remarkable environmental implications. Therefore, this system requires more studies for its optimization and testing with real water samples.

1.5. Annex 1

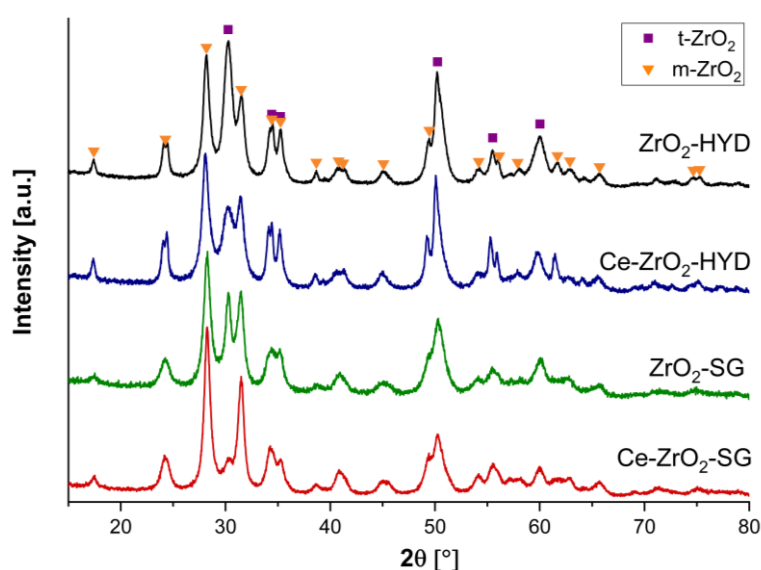


Fig. A1.1. XRD patterns of pure and Ce-doped ZrO₂ prepared by hydrothermal and sol-gel processes. Triangles and squares on top of the patterns indicate the peaks of monoclinic (m-ZrO₂, ICSD #658755) and tetragonal (t-ZrO₂, ICSD #66781) phases, respectively.

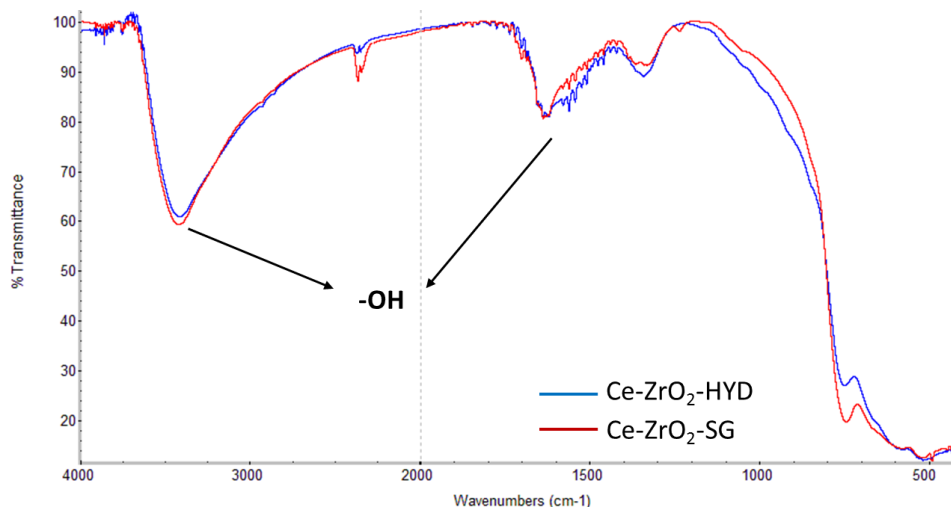


Fig. A1.2. FTIR spectra of Ce-ZrO₂ samples prepared by hydrothermal (HYD) and sol-gel (SG) processes. FTIR spectra were registered in transmission mode using a Bruker Vector 22 spectrophotometer equipped with Globar source, DTGS detector, and working with 128 scans at 4 cm⁻¹ resolution in the 4000-400 cm⁻¹ range. Samples were analyzed as self-supporting pellets by dispersing the samples in KBr (1:20 weight ratio).

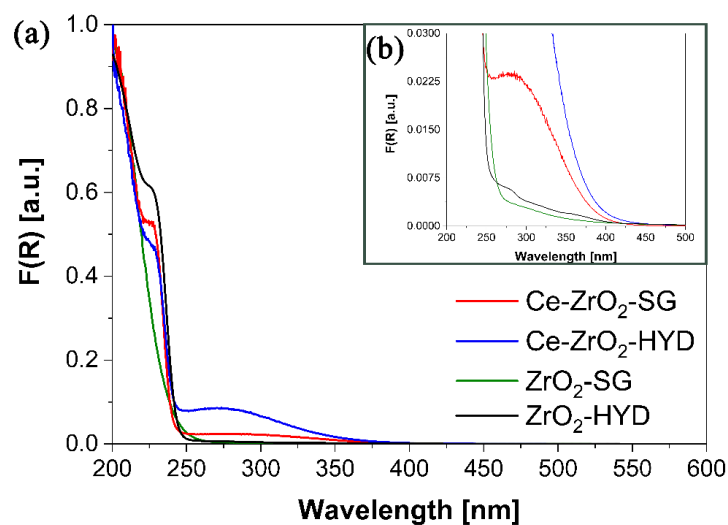


Fig. A1.3. (a) UV-Vis-DRS spectra of pure and Ce-doped ZrO₂ prepared by hydrothermal and sol-gel processes, (b) magnification of region 200-500 nm.

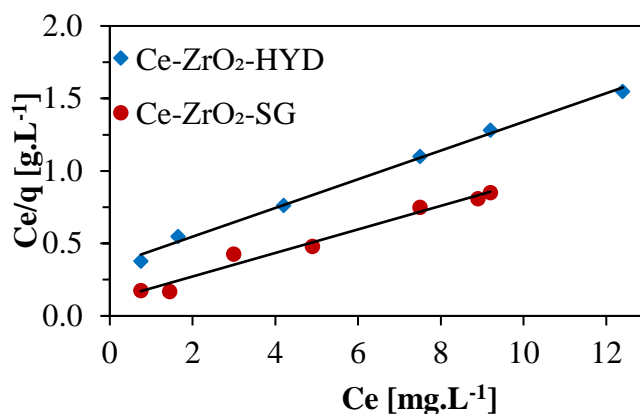


Figure A1.4. Linear fitting of Langmuir isotherm equation to experimental data of HA absorption on Ce-ZrO₂ samples prepared by hydrothermal (HYD) and sol-gel (SG) processes.

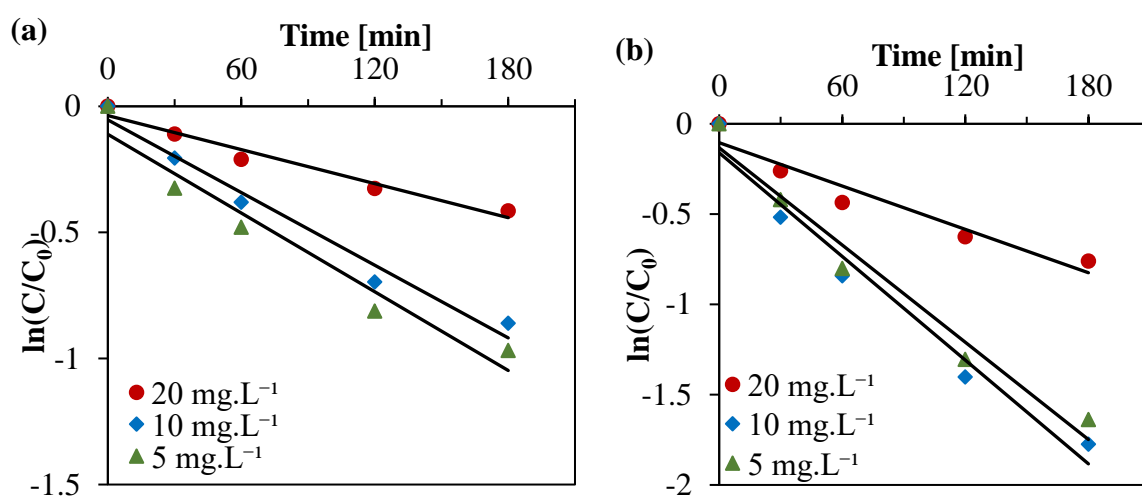


Figure A1.5. Determination of the pseudo-first-order kinetic rate constants, K_{obs} , for (a) Ce-ZrO₂-HYD and (b) Ce-ZrO₂-SG.

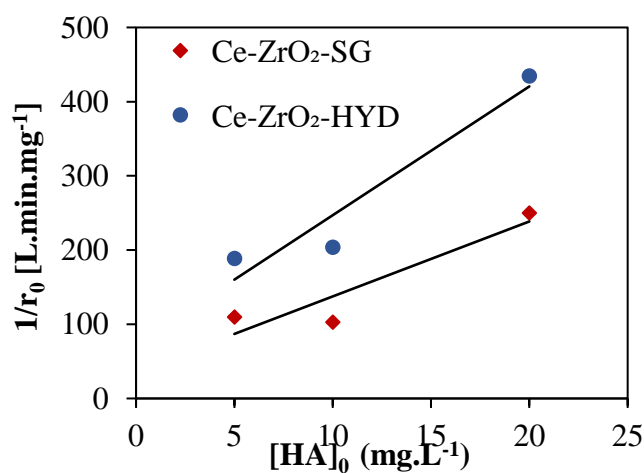


Fig. A1.6. Determination of the Langmuir-Hinshelwood model parameters for Ce-ZrO₂ samples prepared by hydrothermal (HYD) and sol-gel (SG) processes.

2. PHOTOCATALYTIC REMOVAL OF Cr(VI) USING IMMOBILIZED Ce-ZrO₂

Part of the work described in the present chapter has been previously published in:

Bortot Coelho, F.E.; Candelario, V.M.; Araújo, E.M.R.; Miranda, T.L.S.; Magnacca, G. Photocatalytic Reduction of Cr(VI) in the Presence of Humic Acid Using Immobilized Ce-ZrO₂ under Visible Light. *Nanomaterials* **2020**, *10*, 779. <https://doi.org/10.3390/nano10040779>

2.1. Introduction

Hexavalent chromium is widely used in several industrial processes, such as metal plating, leather tanning, pigment, and refractory production [158–160]. There is a serious global concern about the highly toxic effluents generated in these processes, since several cases of chromium contamination have been reported in soil, ground, and surface waters caused by the leakage from landfill sites or inappropriate treatment methods [161]. In aquatic environments, chromium primarily occurs in its hexavalent – Cr(VI) – and trivalent – Cr(III) – states. Hexavalent chromium is considered one of the most dangerous pollutants due to its high-toxicity to human, animals, and plants. It is widely recognized for its teratogenic and carcinogenic effect on human health [162,163]. In addition, high concentrations of Cr(VI) can inhibit significantly the biomass growth during wastewater biological treatments [164].

Several methods can be applied to treat Cr(VI) effluents, such as chemical precipitation, ion-exchange, filtration, solvent extraction, electrochemical, and biological processes [165,166]. Adsorption has been widely studied [167,168] but this method only concentrates the Cr(VI) or immobilize it in solid matrixes, which still need further treatment before disposal [166,169]. Since Cr(III) is about 500 times less toxic than its hexavalent form [170] and it can usually be immobilized through precipitation or adsorption onto a solid phase [161], several Cr(VI) treatment processes start with the reduction of this metal to its trivalent form. However, this reduction is not easily achieved due to the higher Cr(VI) stability in terms of the reduction potential [171], whereas the chemical reduction is an expensive process with a large footprint [172].

In this context, the photocatalytic reduction of Cr(VI) is attracting interest for being more practical and cleaner [172], especially considering the possibility of using solar light to drive the process, which could reduce considerably the costs. Among the photocatalysts available, semiconductors can be used since their conduction band (CB) is more negative than the reduction potential of Cr(VI) (*i.e.* ~ -0.36 at pH 7) [172]. However, as the reduction potential of Cr(VI) becomes more negative at higher pH, the photocatalytic reduction of the Cr(VI) ion is favoured in

lower pH range. Oxides such as TiO_2 [171,173,174] and ZnO [159] have been reported as efficient photocatalysts for this process but these oxides may not be totally stable in acid media [149,175].

Therefore, an alternative is to use zirconium dioxide (ZrO_2) as photocatalyst, since this oxide has an outstanding chemical [46], thermal and mechanical stability [176]. In addition, zirconia is a powerful candidate for Cr(VI) photocatalytic reduction, because the lowest potential of the CB is -1.0 eV (vs. normal hydrogen electrode (NHE), pH 0), much more negative than that of TiO_2 anatase (-0.1 eV), whereas the highest potential of the valence band (VB) is $+4.0$ eV, more positive than that of TiO_2 ($+3.1$ eV) [108]. On the other hand, these band energy levels imply in large band gap value (ca. 5.0 eV), which does not allow the activation of zirconia with solar light. Therefore, our group developed a nanosized Ce-doped zirconia (Ce-ZrO_2) capable of generating photo-induced electrons and holes under visible-light irradiation [108]. The cerium doping add Ce 4f empty intra band states, which act as a bridge between the VB and the CB of zirconia. In a “double jump” mechanism, low-energy photons (visible-light) is absorbed, leading to the excitation of electrons from the valence band to the conduction band [108,119]. This material found applications in degrading pollutants [109,110,119] and promoting water splitting [120].

The use of suspended photocatalysts, especially nanosized ones, presents a major disadvantage related to the catalyst recovery. At the end of the treatment, in fact, a time-consuming and expensive solid/liquid separation step is required to recycle the catalyst and avoid its leakage to the environment, since nanomaterials can harm human health [177] and have ecotoxicological impact [178]. In addition, suspended catalyst particles have a strong light absorption that decreases the depth of penetration of the light [179]. Therefore, a great effort has been made to immobilize photocatalysts on supports in order to obtain better light absorption efficiency and eliminate the catalyst recovery step [180,181].

Regarding the presence of natural organic matter (NOM) such as humic (HA) and fulvic (FA) acids in surface and wastewaters, its effects on Cr(VI) toxicity and treatment are still unclear. Dissolved NOM can promote the Cr(VI) reduction [182,183] but also increases the solubility and mobility of Cr(VI) species in soils [173,183,184]. In addition, undissolved NOM in soils can immobilize Cr(VI) via adsorption [185]; however, the solid-liquid separation in Cr removal process can be hindered by soluble Cr(III)-HA complexes [186].

Previous works studied the use of zirconia alone (*e.g.* N-ZrO_2 [187], amorphous ZrO_2 [188]) or in mixtures with other oxides (*e.g.* CuO/ZrO_2 [189], $\text{ZrO}_2/\text{TiO}_2$ [190], $\text{Fe-ZrO}_2/\text{TiO}_2$ [191–193]) as catalysts for the photoreduction of Cr(VI). However, there is no report on the use of cerium-doped zirconia for Cr(VI) removal neither the use of immobilized Ce-ZrO_2 in photocatalysis.

In this context, this chapter focuses on studying the photocatalytic reduction of Cr(VI) using Ce-doped ZrO₂ under visible light irradiation in aqueous systems. Moreover, it was evaluated how the presence of HA affects the Cr(VI) adsorption and reduction, since humic-like substances are usually present in wastewaters. Initially, in order to study the effects of some parameters (*e.g.* initial pH value and catalyst dosage) on Cr(VI) reduction, experiments were performed with suspended Ce-ZrO₂ particles, using solutions containing Cr(VI). Then, Ce-ZrO₂ immobilized on a macroporous silicon carbide (SiC) was evaluated for the photoreduction of Cr(VI) in a synthetic solution and in a galvanizing industry effluent ([Cr]_{total}= 89 mg L⁻¹, [Cr(VI)]=77 mg L⁻¹, [Zn]=1789 mg L⁻¹).

2.2. Materials and Methods

2.2.1. Synthesis and characterization of the Ce-ZrO₂ photocatalyst

In order to remove Cr(VI) by photoreduction, the catalyst applied was zirconia doped with 0.5 % molar of cerium. This catalyst was tested as suspended powder or immobilized on a support. In the first case, Ce-ZrO₂ nanopowder was synthesized by a sol-gel route developed in a previous work [110]. In brief, for the synthesis processes, 5 mL of zirconium propoxide Zr(OC₃H₇)₄ (CAS 23519-77-9, 70 % wt., Sigma-Aldrich) were mixed with 5 mL of 2-propanol (CAS 67-63-0, 99.5 %, Sigma-Aldrich). Then, 28 mg of Ce(NH₄)₂(NO₃)₆ (CAS 16774-21-3, purity > 98.5 %, Sigma-Aldrich), dissolved in 5 mL of distilled water, were added to the first solution to start hydrolysis. The resulting gel was kept overnight at room temperature and then dried at 80 °C. After aging at room temperature for 10 days, the xerogel was calcined in a muffle furnace at 500 °C in air for 4 h.

A sol-gel process, followed by dip coating and sintering were applied to immobilize Ce-ZrO₂ on a silicon carbide support with a ZrO₂ intermediate layer, which was supplied by LiqTech International A/S (Ballerup, DK). A SiC support was selected owing to this material high porosity, mechanical strength, good thermal and chemical resistance [58–60], which make it applicable in harsh environments, such as high temperature and acid media, where other materials (*e.g.* alumina and silica) fail [194,195]. The coating liquid was a colloidal sol prepared through an adapted procedure for yttria-stabilized zirconia synthesis [31]. For that, 5 mL of zirconium propoxide and 28 mg of Ce(NH₄)₂(NO₃)₆ were diluted in 25 mL of 2-propanol. Next, 60 mL of a 0.05 M solution of HNO₃ (CAS 7697-37-2, >65 %, Aldrich) was added and the system kept under reflux conditions until obtaining a transparent gel. The support was then dip coated with this gel and dried overnight under room temperature. Next, the coated support was calcined in a muffle furnace at 500 °C in air for 4 h. All chemicals were used as received, without further purification.

Zeta potential measurements were performed on a Zetasizer Nano ZS (Malvern Instruments, Malvern, UK) using principles of laser Doppler velocimetry and phase analysis light scattering (M3-PALS technique). 0.1 % w/v suspensions of nanoparticles were prepared with a NaCl 0.01 M aqueous solution and ultrasonicated for 10 minutes before the analysis.

Electronic microscopy images of the immobilized Ce-ZrO₂ were obtained with the Field Emission Gun Scanning Electronic Microscope FIB-FESEM S9000G (Tescan, Brno-Kohoutovice, CZ).

X-ray diffraction analyses (XRD) were performed in the diffractometer PW3040/60 X'Pert PRO MPD (Malvern Panalytical, Almelo, NL), operating at 45 kV, 40 mA, with a Cu K α radiation source ($\lambda = 1.5418 \text{ \AA}$) and a Bragg Brentano geometry over the range $10^\circ < 2\theta < 80^\circ$.

Diffuse Reflectance Spectroscopy (DRS) data were recorded in the 200–700 nm range using a Cary 5000 spectrometer (Varian, US), coupled with an integration sphere for diffuse reflectance studies. A sample of PTFE with 100% reflectance was used as the reference. The optical band gap energy has been calculated from the Tauc plot.

2.2.2. Photocatalytic Experiments

Stock Cr(VI) and humic acid solutions were prepared by dissolving the desired amounts of K₂Cr₂O₇ (CAS 7778-50-9, Sigma Aldrich, >99 %) and humic acid sodium salt (CAS 68131-04-4, Sigma Aldrich, MP > 300 °C) in distilled water. The pH values of the solutions were adjusted to the desired value using aqueous solutions of NaOH and HCl. A wastewater from a Cr(VI) bath used to passivate steel pieces coated with fused zinc was collected from a galvanizing industry in the state of Minas Gerais (Brazil). This effluent has a density of 1.007 g cm⁻³ at 20 °C, a pH value of 2.9, and a metal concentration of: [Cr]_{total} = 89 mg L⁻¹, [Cr(VI)] = 77 mg L⁻¹, [Zn] = 1789 mg L⁻¹.

For the first part of the photocatalytic reduction experiments, with powdery Ce-ZrO₂, a specific amount of the catalyst was added to the Cr(VI) or Cr(VI)+HA solutions in order to achieve the desired dosage. As a reactor, a 100 mL borosilicate glass was used. The pH was then adjusted to the desired value. Prior to irradiation, the mixture was kept at room temperature ($25 \pm 3 \text{ }^\circ\text{C}$), under stirring, in the dark, for 3 hours in order to achieve the adsorption equilibrium. Then, the mixture was irradiated with visible light for 3 h under stirring, without any injection of gas. Samples were collected in specific intervals of time and filtered with 0.27 μm siring filters prior to Cr(VI) analysis. All experiments were performed in duplicate.

As light source, an 18 W white LED lamp (Wellmax, Shanghai, CN) was used. This lamp has a colour temperature of 6500 K and, as indicated by the manufacturer, no UV/IR emission. In order to confirm the lamp emission, the UV irradiance ($\lambda < 400 \text{ nm}$) was measured with the light meter HD 2302.0 (Delta OHM, IT). No UV emission was detected, thus no filter was applied in

the photocatalysis experiments. When the lamp was positioned just above the beaker, the measured VIS-light irradiance ($400 <\lambda < 700 \text{ nm}$) was 1000 W m^{-2} .

For the second part of the experiments, Ce-ZrO₂ immobilized on the support (SiC/ZrO₂) was applied to the Cr(VI) photoreduction. A piece of 4x6 cm was added to a petri dish containing 30 mL of a Cr(VI) model solution or the galvanizing industry effluent (diluted 7X in order to achieve a Cr concentration of 11 mg L^{-1}) and positioned under the above-mentioned lamp (**Fig. 2.1**). In order to keep the system under stirring, the petri dish was placed in an orbital shaker at 400 rpm. A test with the diluted effluent spiked with HA was also performed. In the experiments with the Cr(VI) solution the initial pH was adjusted to 4, while for the effluent, it was utilized the natural value of the diluted effluent, around 3.5. Next, the system was kept in the dark for 6 h, for allowing the adsorption equilibrium, and then irradiated by visible light for 6 h. Samples were collected in specific intervals of time and stored for analysis. The temperature observed during the experiment never overcame 35°C. Although the lamp heat caused some evaporation/condensation of the solvent, the use of a closed container avoided loss of material and concentration changes. A control test was done with the system in the dark but heated at 35-40 °C and no significant difference was observed in comparison with the non-heated one.

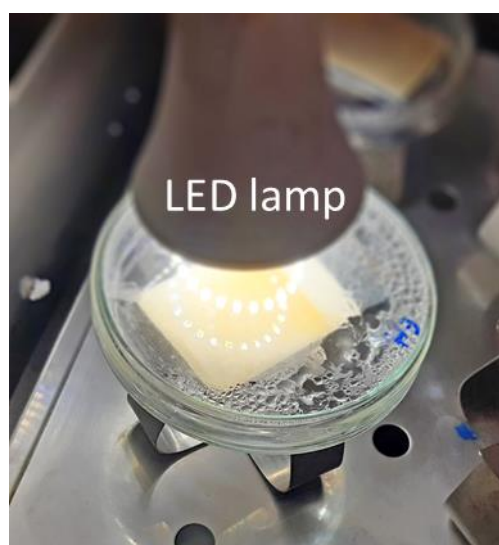


Fig. 2.1. Experimental setup for Cr(VI) photocatalytic reduction with immobilized Ce-ZrO₂.

The Cr(VI) concentration was determined applying the 1,5-diphenylcarbazide (DPC) method [196], in which the samples absorbance at 540 nm was measured with the UV-Vis spectrophotometer Cary 300 Scan (Varian, Palo Alto, USA). The concentration of HA in the samples was calculated using the UV absorbance at 254 nm [81,113–116], measured with the same equipment on samples before DPC addition. In the experiments with the effluent, the total Cr and

Zn concentrations were measured by atomic absorption spectroscopy (AAS) using the spectrophotometer XplorAA (GBC Scientific Equipment, Braeside, AU).

The Eh-pH (Pourbaix) diagram for the system Cr-H₂O was generated using the software HSC Chemistry 6.0 (Outokumpu, Helsinki, FI). The stability areas of the Cr species was calculated considering the reduction potentials and equilibrium constants provided by the software at the temperature of 25 °C and for a total Cr(VI) concentration of 10 mg L⁻¹.

2.3. Results and Discussion

2.3.1. Suspended Ce-ZrO₂ nanopowder

In previous works [108–110,119,120], it was studied the development and testing of Ce-ZrO₂ nanoparticles. An extensive the characterization of the material was performed, including XRD, SEM, TEM, N₂ adsorption/desorption, diffusive reflectance, and photo-electronic characterization. In summary, these analyses demonstrated that Ce-ZrO₂, prepared by the same sol-gel procedure applied in the present work, presents both tetragonal and monoclinic phases with crystallite size around 15 nm [109]. The specific surface are of this material is $70 \pm 7 \text{ m}^2 \text{ g}^{-1}$, the total pore volume is $0.33 \text{ cm}^3 \cdot \text{g}^{-1}$ and pore sizes from 3-10 nm [110]. In spin trapping electron paramagnetic resonance (EPR) experiments, Ce-doped zirconia formed two paramagnetic species (trapped electrons as Zr³⁺ species and holes as O⁻ species, when irradiated by visible light (>420 nm) [102]. It was also observed the formation of •OH radicals under visible light irradiation using the spin trap DMPO (5,5-Dimethyl-1-Pyrroline-N-Oxide) [108]. These results confirmed the photoactivity of the material under visible light, and allowed its application in the photocatalytic degradation of 2-propanol [119], methylene blue [102], and humic acid [110].

In the following items, we will discuss the activity of Ce-ZrO₂ nanopowder on photocatalytic reduction of Cr(VI) and the effects of the catalyst dosage and the initial pH on the Cr(VI) removal from model solutions containing only Cr(VI) or Cr(VI)+humic acid.

2.3.1.1. Effects of pH, HA, and catalyst dosage on Cr(VI) adsorption

It can be observed in **Fig. 2.2** that the Cr(VI) adsorption increases with higher catalyst dosages and lower the pH values for the systems without and with HA.

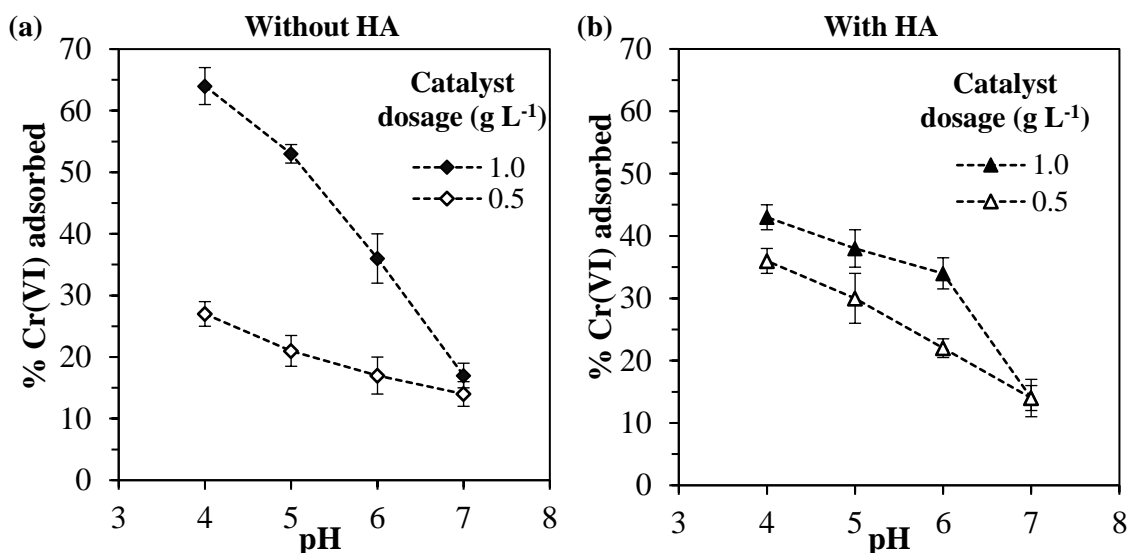


Fig. 2.2. Percentage of Cr(VI) adsorbed for different pH values and catalyst dosages for the systems: (a) without humic acid and (b) with 10 mg L⁻¹ of humic acid.

Considering first the system without HA (**Fig. 2.2a**), for pH values lower than 7, the use of double catalyst dosage led to an average increase of 2.3-fold in the amount of Cr(VI) adsorbed, since the higher mass of ZrO₂ exposed more active sites available for adsorption [197]. The increase in the amount of Cr(VI) adsorbed with higher catalyst dosage was also reported by other authors, which also observed this non-linear behaviour [198,199].

Regarding the pH value, higher Cr(VI) amounts were adsorbed in more acidic environments. This can be explained by the reduction of the electrical repulsion between chromium species and the zirconia surface. In fact, analysing the Cr(VI) species distribution (**Fig. 2.3b**), it can be observed that for pH values lower than ~6.5, the prevalent chromium species changes from the bivalent anion CrO₄²⁻ to the monovalent anion HCrO₄⁻. At the same time, in lower pH range the surface charge of Ce-ZrO₂ becomes less negative, as shown by ζ -potential measurements (**Fig. 2.3a**), with the protonation of OH groups at the surface. Therefore, in more acid media both Cr(VI) species and zirconia surface becomes less negatively charged, which reduces the repulsion and increases the adsorption, as reported by other authors for Cr(VI)-TiO₂ systems [158,173].

Concerning the ζ -potential of Ce-ZrO₂, this material exhibits a negative charge in a wide range of pH (>3.5) because of the presence of hydroxyl groups (ZrO₂-OH) on zirconia surface [123]. Other author [124] also observed a high negative ζ -potential of ZrO₂ as the pH increase.

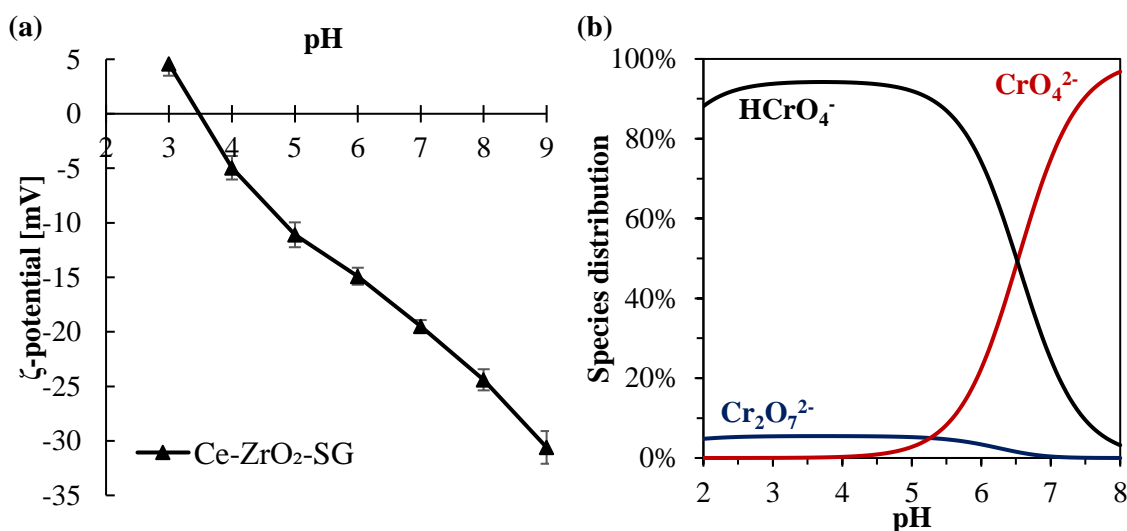


Fig. 2.3. (a) Cr(VI) species distribution diagram for a total Cr(VI) concentration of 10 mg L⁻¹ in water; (b) ζ-potential for Ce-doped zirconia.

Considering now the effect of humic acid, it is known that both Cr(VI) and HA compete for the adsorption at the zirconia surface [158] and that the number of active sites in the solid is limited. It should be noticed that in all the experiments, the adsorption of HA was greater than 80 % (data not shown), which was favoured by the range of pH utilized, since the humic acid adsorption is strongly increased in acid media [81,110,113,114,136,200].

Since for the catalyst dosage of 1.0 g L⁻¹ the presence of humic acid decreased the Cr(VI) adsorption, it may be concluded that HA is preferably adsorbed by zirconia, occupying the active sites of the catalyst. Nevertheless, for the catalyst dosage of 0.5 g L⁻¹, the presence of HA has slightly increased the Cr(VI) adsorption. Since humic acid can form complexes with Cr(VI) species[201], these Cr(VI)-HA complexes may be adsorbed by the catalyst, increasing the Cr(VI) adsorption in comparison with the system without HA.

2.3.1.2. Effects of HA and pH on the Cr(VI) photocatalytic reduction under different catalyst dosages

In **Fig. 2.4**, it can be observed the total removal of Cr(VI), *i.e.* combined effects of adsorption in the dark and photocatalytic reduction. The adsorption was discussed in the previous section. Now, in order to understand the contribution of the Cr(VI) photocatalytic reduction and the effects of pH and HA, each parameter is going to be studied separately.

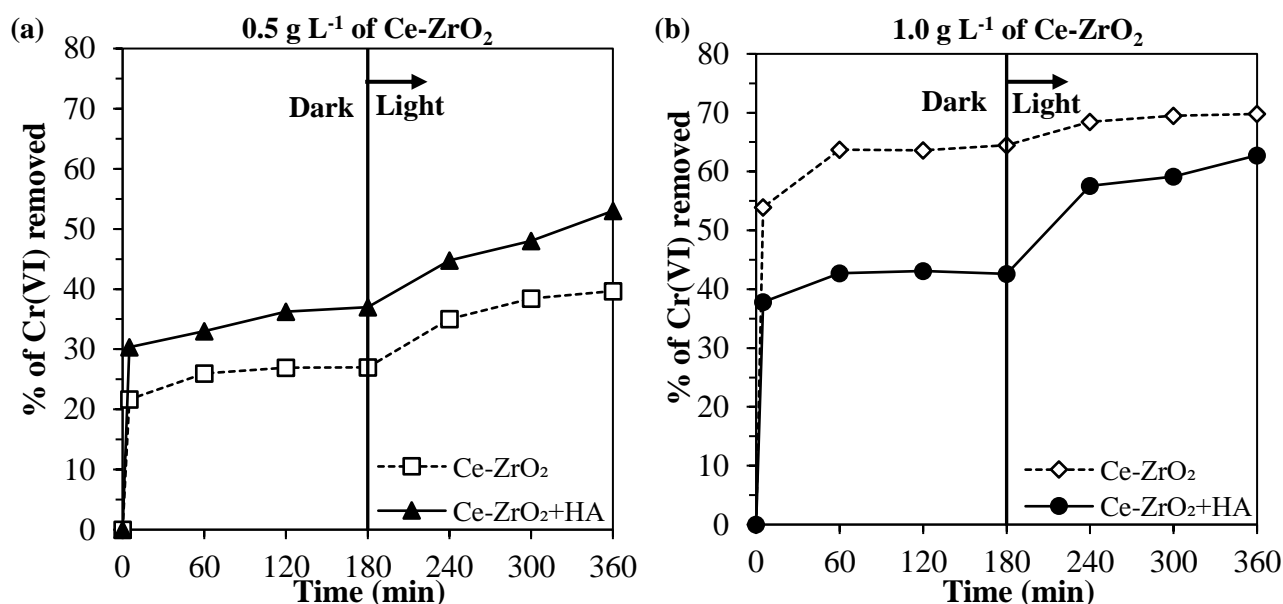


Fig. 2.4. Cr(VI) removed at an initial pH of 4, without HA and with 10 mg L⁻¹ of HA, in the experiments using: **(a)** 0.5 g L⁻¹ of Ce-ZrO₂ and **(b)** 1.0 g L⁻¹ of Ce-ZrO₂.

In the systems without humic acid (**Fig. 2.5a**), as expected, the higher catalyst dosage led to the higher Cr(VI) removal, since the number of adsorbing sites and electrons generated in the conduction band increase with increasing Ce-ZrO₂ amount. However, the comparison with **Fig. 2.5c** indicates that the photoreduced Cr(VI) amount does not increase significantly doubling the catalyst dosage, indicating that too much catalyst can shield the absorption of the incident light [158]. Further experiments are therefore needed to evaluate the optimal amount.

The initial pH value has two effects on Cr(VI) removal. As discussed previously, acid media favour the Cr(VI) adsorption by reducing the electrical repulsion between Cr(VI) species and the Ce-ZrO₂ surface. At the same time, also the photocatalytic reduction of Cr(VI) is favoured at lower pH values, as shown in **Fig. 2.5c**.

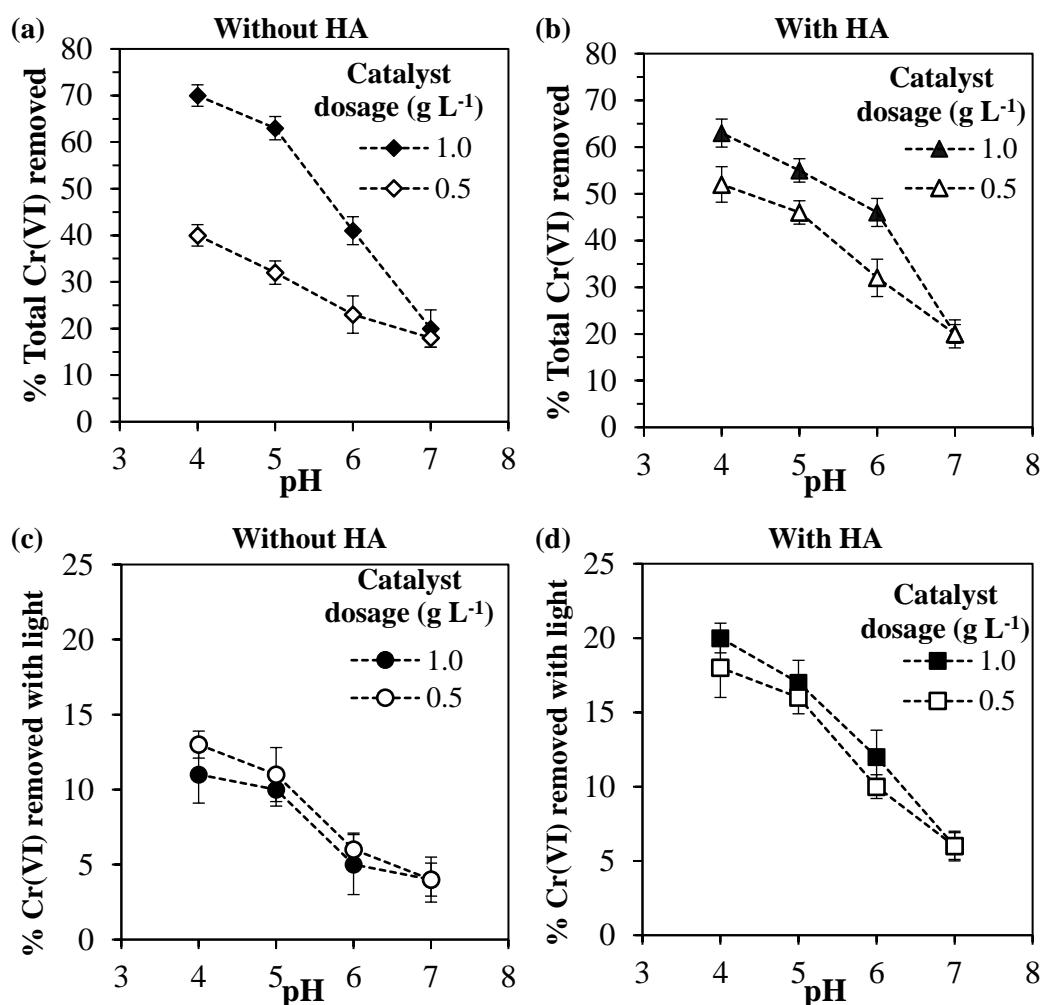


Fig. 2.5. (a, b) Total Cr(VI) removed and (c, d) Cr(VI) removed by photoreduction for different pH values and catalyst dosages for the systems: (a, c) without humic acid and (b, d) with 10 mg L⁻¹ of humic acid.

There are many reasons explaining this phenomenon:

The Cr(VI) photocatalytic reduction is controlled by a surface-reaction step [158,198,202] thus, lowering the pH favours the Cr(VI) adsorption and then increases the Cr(VI) reduction;

As shown in **Fig. 2.6**, the reduction potential of HCrO_4^- ($E^\circ = 1.35 \text{ V}$) is higher than that of CrO_4^{2-} ($E^\circ = -0.13 \text{ V}$) [203]. Since at lower pH values HCrO_4^- is the predominant species, the Cr(VI) reduction is favoured;

The photocatalytic reduction of Cr(VI) is driven by the difference between the potential of the photo-induced electron at the catalyst CB and the reduction potential of Cr(VI) [158,172]. From Equations (1) and (2), it can be observed that the reduction potentials become more negative for lower pH values, while the potential of the photo-generated electron at CB shifts to more

positive potentials [204], therefore the driving force for the Cr(VI) photocatalytic reduction increases in acid media.

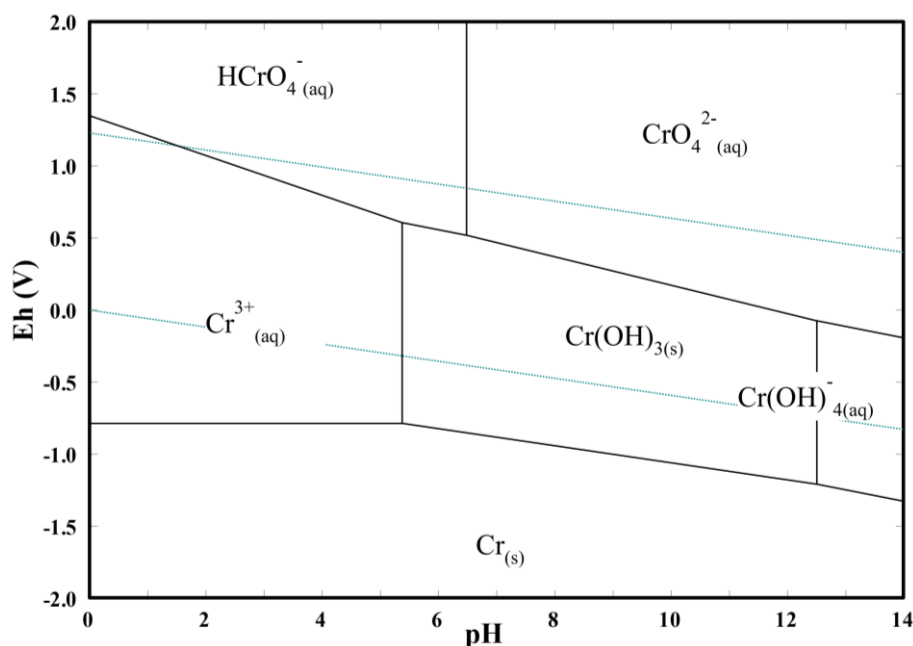
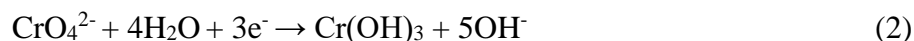
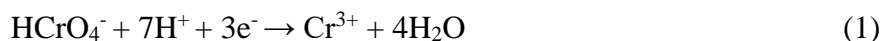


Fig. 2.6. Potential in respect to the standard hydrogen electrode (Eh) versus pH diagram of Cr-H₂O system at 25°C for a total chromium concentration of 10 mg L⁻¹.

In the presence of humic acid (**Fig. 2.5b**), for the catalyst dosage of 0.5 g L⁻¹, higher Cr(VI) total removal percentages were obtained in comparison with the systems without HA (**Fig. 2.5a**), but for the catalyst dosage of 1.0 g L⁻¹, the presence of HA did not change significantly the Cr(VI) total removal. The important effect of HA was to increase the percentages of the Cr(VI) removed by photocatalytic reduction (**Fig. 2.5c, 2.5d**) for both catalyst dosages. In addition, when HA was present, the Cr(VI) photocatalytic reduction was less affected by the pH and the catalyst dosage.

In order to explain these results, it should be considered that HA is involved in two different processes with opposite effects:

HA is adsorbed at the photocatalyst surface, occupying the active sites for Cr(VI) adsorption and reduction, decreasing Cr(VI) removal efficiency;

The adsorbed HA, being an electron-rich molecule, acts as a scavenger for positive holes at the ZrO₂ valence band, which reduces the electron-hole recombination rate [199] and consequently increases the Cr(VI) photocatalytic reduction efficiency. This was also reported for Cr(VI) photocatalytic reduction using TiO₂ in the presence of organic compounds, such as humic acid [158,173], phenol [173,205], ethanol [198,206], and citric acid [172].

Therefore, the final effect of HA on Cr(VI) removal is a balance between these two effects, which depends on the solid loading, pH, and HA concentration. For the zirconia loading of 0.5 g L⁻¹, the HA increases both Cr(VI) adsorption and photocatalytic reduction, which leads to higher Cr(VI) total removals. For a loading of 1.0 g L⁻¹, the Cr(VI) adsorption is hindered because HA is preferably adsorbed and occupies the active sites of the catalyst, but still HA increases the Cr(VI) photocatalytic reduction by scavenging the holes on the VB. In agreement with these statements, the observed rate constants, considering a first-order reaction, were 0.11 and 0.16 h⁻¹ for Cr(VI) and Cr(VI)+HA systems, respectively, using 1.0 g L⁻¹ of catalyst. It is worth noting that in all the tests the removal of HA after the end of the irradiation was higher than 90 % (data not shown).

In view of the experimental results and previous works with zirconia [102,108,110] and Cr(VI)+TiO₂ works [158,161,205], a simplified mechanism was proposed in **Fig. 2.7**.

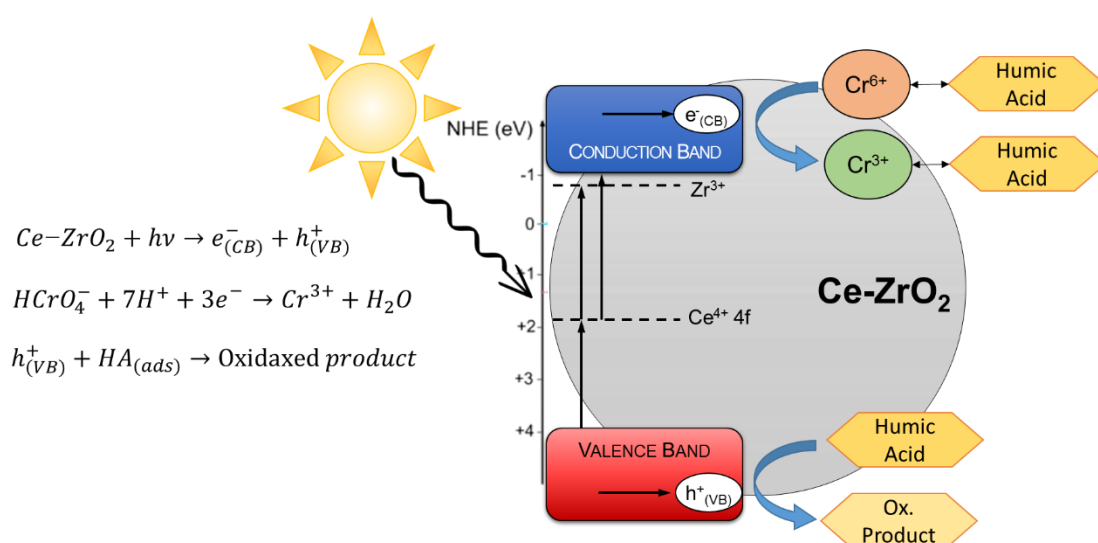


Fig. 2.7. Proposed mechanism for the photocatalytic reduction of Cr(VI) in the presence of HA using Ce-ZrO₂ under visible light irradiation.

In order to evaluate the fate of the adsorbed Cr species on Ce-ZrO₂, the catalysts used for the experiments shown in **Fig. 2.4b** (1 g L⁻¹ of Ce-ZrO₂ and initial pH of 4) were recovered and washed with a strong basic solutions to promote the complete desorption. Then, the washing solutions were analysed in order to determine the amount of Cr(VI) released. Once knowing the initial and final Cr(VI) concentrations, and the amount that was adsorbed, it was calculated, through a mass balance, how much Cr(VI) was reduced to Cr(III). As a result, it was observed that ~60 % of the adsorbed chromium was reduced to Cr(III) and the rest remained as Cr(VI). For the non-adsorbed Cr(VI), which remained in the starting solution, 36 % was reduced to Cr(III) in the presence of HA, whereas this value dropped to 25 % without HA. This result corroborates with the proposed mechanism, in which the photocatalytic reduction depends on the adsorption of the Cr(VI) species at the catalyst surface and that the HA favours the photoreduction by acting as a

hole scavenger. In addition, the presence of HA can be considered beneficial since, in its presence, Cr(III)-HA complexes are formed when Cr(VI) is reduced to Cr(III). These complexes are less toxic than Cr(III) species [182].

Another positive effect of HA reported in literature, is the direct electron transfer from the light-excited HA to Cr(VI), promoting the metal reduction, which would require lower energies than the semiconductor band gap [199]. However when experiments without Ce-ZrO₂, only with Cr(VI) and humic acid, were performed, very low Cr(VI) removals were observed, which confirms the actual photocatalytic activity of Ce-ZrO₂.

2.3.2. Immobilized Ce-ZrO₂

In order to increase the photocatalytic reduction efficiency and avoid the use of suspended nanoparticles, hard to recover, Ce-ZrO₂ was immobilized on a silicon carbide support coated with ZrO₂ as intermediate layer (**Fig. 2.8a**). The FE-SEM analysis of the Ce-ZrO₂ immobilized on the support (**Fig. 2.8b**) indicated the presence of nanometric particles and a layer thickness of around 2 μm. Previous TEM analysis confirmed that Ce-ZrO₂ nanoparticles are a mix of nanometric grains of about 10 nm with twinned grains of a relatively larger dimension (from 15 to 60 nm) and some bigger crystals of about 100 nm [120].

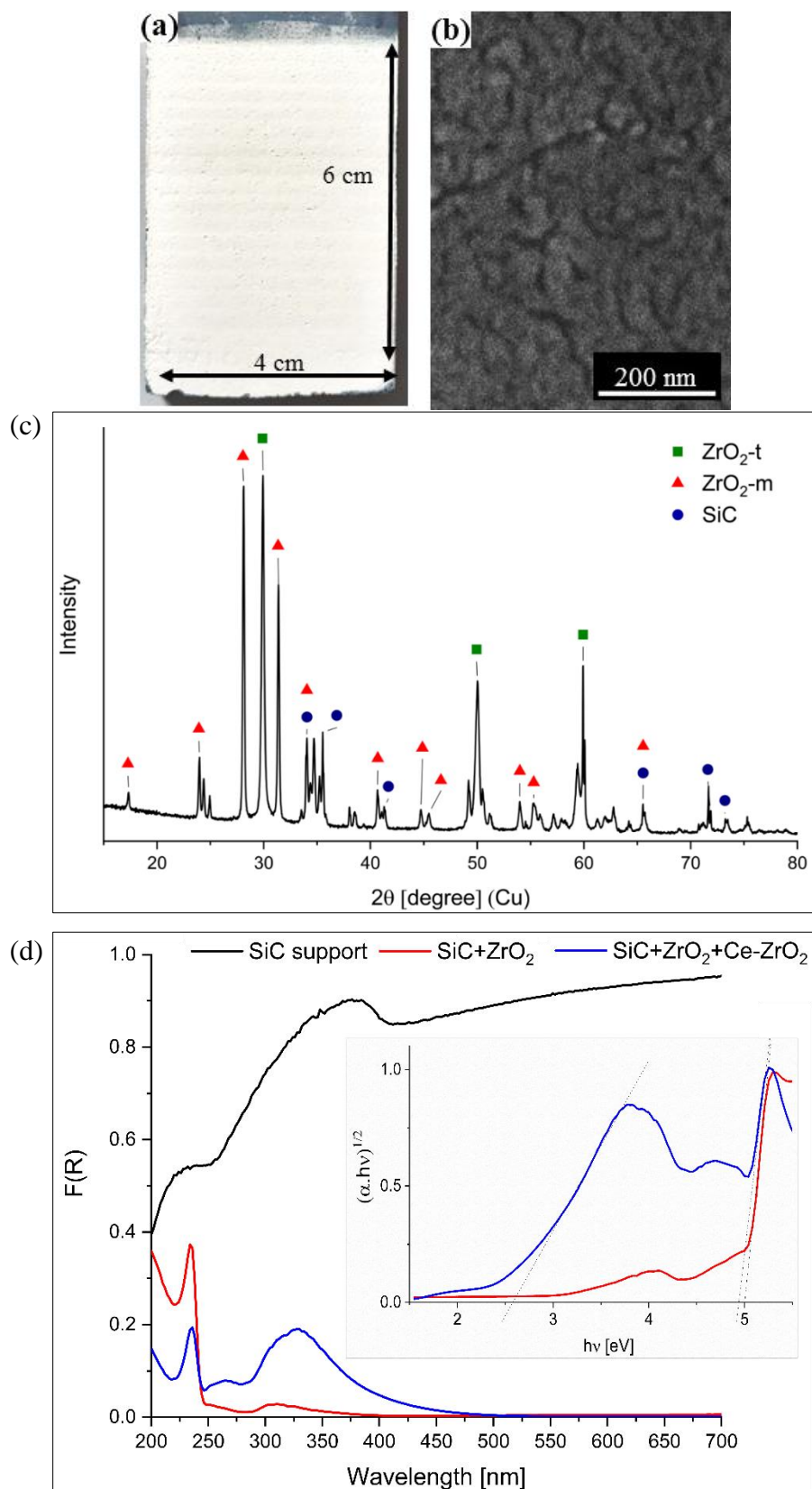


Fig. 2.8. (a) Photo, (b) FE-SEM image, and (c) X-ray diffractogram of the immobilized Ce- ZrO_2 on the SiC support. (d) Absorbance spectra of the samples obtained by applying the Kubelka-Munk function, $F(R)$, to the diffuse reflectance spectra. The inset is the Tauc plot of the SiC support+ ZrO_2 intermediate layer and the immobilized Ce- ZrO_2 .

In the X-ray diffractogram of the immobilized Ce-ZrO₂ (**Fig. 2.8c**), it is possible to identify a SiC phase (ICDD Ref. code 00-049-1428), which corresponds to the silicon carbide support. The zirconia phases observed correspond to the ZrO₂ intermediate layer and to the immobilized Ce-ZrO₂. As obtained from previous XRD analysis of the unsupported Ce-doped zirconia [110], both monoclinic (ZrO₂-m, ICSD #658755) and tetragonal (ZrO₂-t, ICSD #66781) phases form during the synthesis. No evidences related to a preferred phase for the photocatalytic activity were reported, however the presence of both phases could enhance the charge separation at the interface between the two polymorphs [120] reducing the charge recombination probability, similarly to what proposed for anatase and rutile in TiO₂ P25 (Evonik) [207].

Fig. 2.8d presents the UV-Vis absorption spectra obtained by Diffuse Reflectance Spectroscopy (DRS) of the SiC support, the SiC support with the ZrO₂ intermediate layer and the immobilized Ce-ZrO₂. Since the silicon carbide support is black, it absorbs light in the whole UV-Vis spectra, whereas when coated with the white ZrO₂ intermediate layer, only UV light is absorbed. The spectrum obtained for ZrO₂ layer matches that reported for pristine ZrO₂ [108,109,119], in which the band gap transition occurring at about 250 nm (5 eV) is due to the excitation of the electrons from the VB to the CB of this oxide. A weak absorption between 250 nm and 350 nm is caused by some point defects present in the material [125]. In the spectrum of the Ce-ZrO₂ immobilized on the SiC support with the ZrO₂ intermediate layer, it is observed an absorption shoulder centred at ca. 330 nm with a tail in the visible region. Analysing the band gap transitions, two E_{gap} values are reported, 4.9 and 2.6 eV. The first value is associated with the fundamental VB→CB transition of ZrO₂, which was practically unaffected by the Ce doping, the second value is due to the absorption band associated to the VB → Ce 4f charge transfer transition [119]: this result indicates that the immobilized Ce-doped zirconia has the potential to work as a photocatalyst under visible light irradiation.

2.3.2.1. Experiments using a solution containing Cr(VI)

In **Fig. 2.9a**, it is shown that, using the immobilized Ce-ZrO₂ on the silicon carbide support, the removal of Cr(VI) reached 77 % for a model solution containing 10 mg L⁻¹ of Cr(VI), no humic acid, and at an initial pH of 4. It can be observed that a strong adsorption of Cr(VI) occurred in the dark period, as reported for the suspended catalyst. However, a direct comparison with the powdery catalyst is not possible since it is difficult to determine the amount of Ce-ZrO₂ that was immobilized on the support and the related active fraction. Nevertheless, when the visible-light irradiation started, it was clearly observed that the photocatalytic reduction of Cr(VI) occurred. Considering a first-order reaction, the observed rate constant (K_{obs}) was 0.13 h⁻¹, value compatible with the ones obtained in the presence of suspended catalyst.

The effect of the initial Cr(VI) concentration on the Cr(VI) removal with immobilized Ce-ZrO₂ at pH 4 is shown in **Fig. 2.9b**. It can be observed that for an initial Cr(VI) concentration of 10 mg L⁻¹, a high removal of chromium was achieved, whereas for the concentrations of 50 and 100 mg L⁻¹, the Cr(IV) removal did not overcome the values around 11 %. Thus, it can be concluded that the removal of Cr(VI) is significantly dependent on the initial Cr(VI) concentration in the feed and follows an inverse relationship with the concentration, as reported by other authors [138,161,208]. The main reason for that is that increasing the concentration of Cr(VI) more light is absorbed by the solution, and therefore, less photons reach the catalyst surface to promote the charge separation and consequently the Cr(VI) reduction [161].

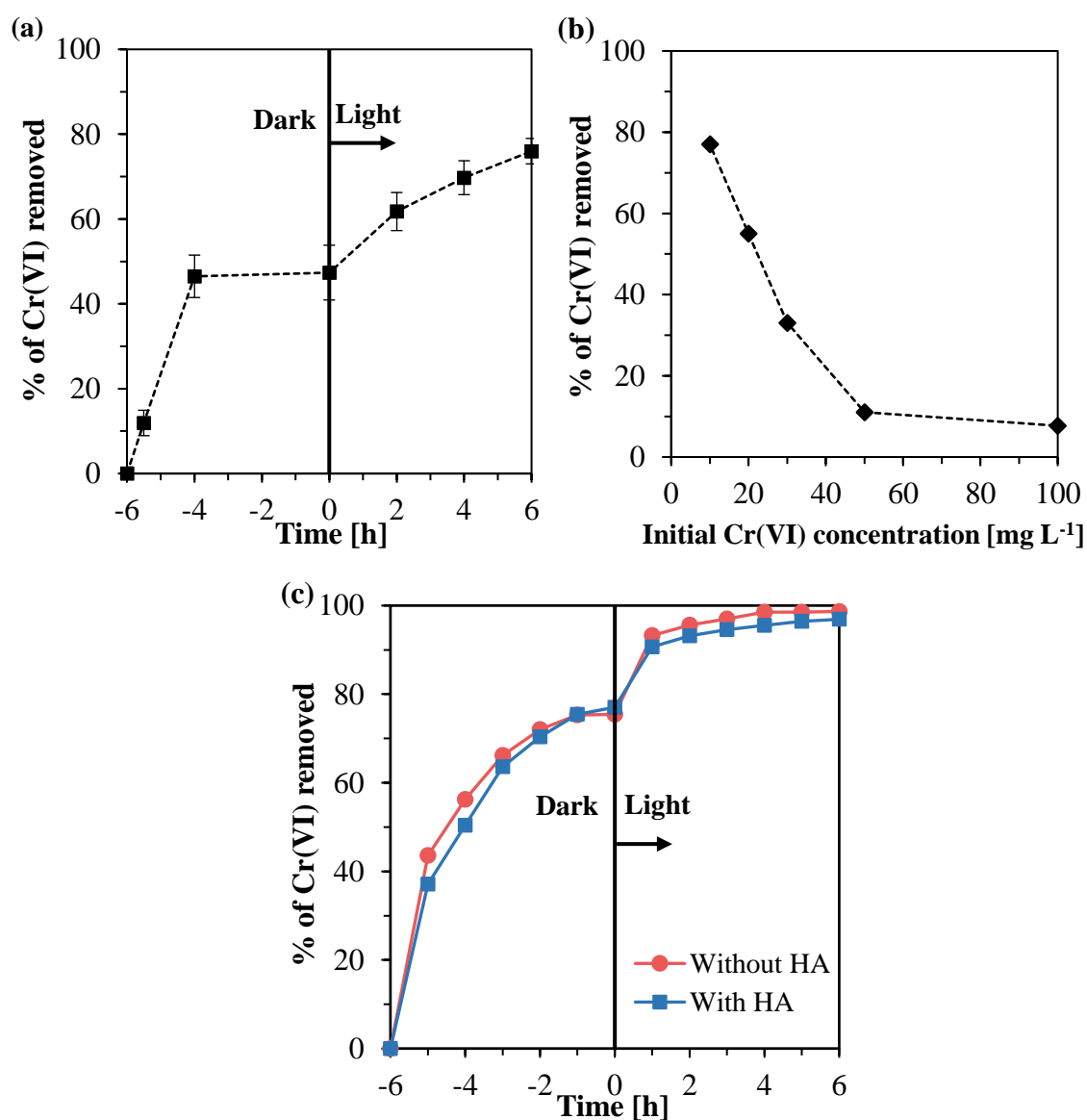


Fig. 2.9. Percentages of Cr(VI) removed using immobilized Ce-ZrO₂ in the tests with: **(a)** model solution containing 10 mg L⁻¹ of Cr(VI); **(b)** model solutions containing different initial Cr(VI) concentrations; **(c)** diluted galvanizing industry effluent.

2.3.2.2. Experiments with the galvanizing industry effluent

In view of the satisfactory results obtained with the supported Ce-ZrO₂ for the model Cr(VI) solution, the next step was to evaluate the efficiency of this material in the treatment of a real Cr(VI) effluent, since complex matrixes can affect significantly the photocatalytic mechanism [209,210].

The galvanizing industry effluent studied here contains a high concentration of Zn and Cr(VI), 1789 and 77 mg L⁻¹, respectively. As reported in the previous item, the Cr(VI) removal efficiency decreases considerably at higher Cr(VI) concentrations. Therefore, prior to the experiments, the effluent was diluted 7 times in order to achieve a Cr(VI) concentration of 11 mg L⁻¹. It is worth noting that the total Cr concentration in the effluent is 89 mg L⁻¹, which means that a small amount of dissolved Cr(III) is also present. Since the effluent does not contain dissolved organic matter, one test was made with the diluted effluent spiked with HA. The results of the photocatalytic reduction of Cr(VI) using immobilized Ce-ZrO₂ are shown in **Table 2.1**.

Table 2.1. Removals of total Cr, Cr(VI), and Zn for the diluted effluent treatment with the immobilized Ce-ZrO₂.

	Without HA		With HA (10 mg L ⁻¹)	
	After 6 h in dark	After 6 h of irradiation	After 6 h in dark	After 6 h of irradiation
Removal of Cr total [%]	77.1	98.4	75.5	98.8
Removal of Cr(VI) [%]	77.1	97.2	75.5	97.3
Removal of Zn [%]	13.6	19.9	12.6	17.6

As shown in **Table 2.2**, the variations in Zn concentration due to its adsorption are 4 times greater than the ones obtained for Cr(VI). From this table, it can also be seen that 4 to 5 % of the zinc was removed after light irradiation. However, there is no evidence to confirm that this zinc removal was due to adsorption or photocatalytic reduction, since the standard reduction potential of Zn²⁺ (-0.76 V) is much lower than the one of Cr(VI)[203].

Table 2.2. Concentrations of zinc in samples from the experiments with the diluted galvanizing effluent with and without humic acid.

	Without HA		With HA (10 mg L ⁻¹)	
	Cr(VI) [mg L ⁻¹]	Zn [mg L ⁻¹]	Cr(VI) [mg L ⁻¹]	Zn [mg L ⁻¹]
Initial	11	254	11	254
After 6 h in dark	2.5	219	2.2	222
After 6 h of irradiation	0.1	205	0.3	211

The Cr(VI) removal efficiencies for the model Cr(VI) solution and the diluted galvanizing effluent were ~76 % and >97 %, respectively. The first reason for the higher removal of Cr(VI) with the galvanizing effluent is that the effluent pH value is lower (~3.5) than the one tested for the model solution (4.0). As discussed previously, the Cr(VI) photoreduction is strongly favoured in more acidic medias. Another reason for the higher removals of Cr(VI) is the presence of Cr(III) and Zn(II) in the galvanizing effluent, which help maintaining the pH stable by forming hydroxo-complexes acting as pH buffer [208].

On the contrary, the presence of HA does not seem to have significant effect on Cr(VI) removal, even if the effect was clearly visible when it was used the suspended catalyst powder. Actually, in the case of the diluted effluent spiked with HA, the humic acid was no longer detectable by the UV-Vis analyses carried out after 1 h of experiment in the dark, as it was completely adsorbed by the immobilized Ce-ZrO₂ and also by the mesoporous silicon carbide support. Therefore, there was no humic acid available anymore to participate the reaction and affect the Cr(VI) removal.

Analysing the final concentrations of Cr(VI) in the samples (**Table 2.2**), it can be seen that more than 97 % of chromium was removed from the galvanizing industry effluent. The limit of discharge of Cr(VI) species for industrial waste streams to be discharged to surface water varies by country, but in general, this limit is in the range 0.1 and 0.5 mg L⁻¹ [211,212]. Therefore, the diluted effluent after photocatalytic treatment with immobilized Ce-ZrO₂ would be within the discharge limit for Cr(VI).

2.4. Conclusions

In the present chapter, it was studied the removal of Cr(VI) by photocatalytic reduction promoted by suspended and immobilized Ce-ZrO₂ under visible light irradiation. For the model Cr(VI) solution, it was observed that higher catalyst dosages and lower initial pH values favours

Cr(VI) adsorption and photoreduction. The reason is that in more acidic media, the electrostatic repulsion between zirconia surface and Cr species are limited. At the same time, the driving force for the reaction is increased because CrO_4^{2-} converts to HCrO_4^- , which has a higher reduction potential and less repulsion by the zirconia surface.

Regarding the effects of humic acid, there is a balance between beneficial and detrimental effects. Since HA is preferably adsorbed by Ce-ZrO₂, it reduces Cr(VI) adsorption by occupying the active sites. On the other hand, HA act as holes scavenger, reducing the electron-hole recombination, favouring then the photocatalytic reduction of Cr(VI). Therefore, the combination of these effects on the total Cr(VI) removal was dependent on the catalyst dosage, but in all cases the amounts of Cr(VI) reduced with the irradiation were higher in the presence of HA, even at higher pH values. In the best condition, it was possible to remove 70 % of Cr(VI) from the model solution containing only Cr(VI) at an initial pH of 4, using 1.0 g L⁻¹ of Ce-ZrO₂.

The experiments with the supported Ce-ZrO₂ demonstrated the feasibility of immobilizing this catalyst without changing its photocatalytic properties. The immobilized Ce-ZrO₂ was able to treat a diluted galvanizing industry effluent with a high concentration of zinc, achieving Cr(VI) removals greater than 97 % after visible light irradiation, which would allow its discharge into surface waters. The presence of HA did not affect the processes.

From a technical point of view, these results indicate that immobilized Ce-doped zirconia could be applied to treat Cr(VI) effluents even in the presence of other metals and naturally occurring organic matter, such as humic-like substances. The advantages of this material are its great chemical and mechanical resistances and the chance to avoid nanoparticle recovery. In addition, there is the possibility to use visible light sources, such as solar light, which contributes to the development of more sustainable, cleaner, and cost-effective wastewater treatments. Nevertheless, as all new technologies, an economic analysis should be performed in order to verify the feasibility of the proposed treatment in comparison to consolidated technologies.

3. ZrO₂/SiC ULTRAFILTRATION MEMBRANE

3.1. Introduction

Few are the works devoted to the development of ZrO₂ membranes on SiC support [12,213] considering that there are several challenges in the ceramic processing (slurry) and sol-gel routes used in its fabrication. This process needs to overcome the following issues: to form a homogeneous thin layer of ZrO₂ by controlling the viscosity of the dipping fluid and its particle/sol size to avoid excessive infiltration into the support [35,214,215]; and to avoid the cracks that can occur during the high temperature sintering because of ZrO₂ and SiC different thermal expansion coefficients [216] and the big volume variation that zirconia undergoes in the monoclinic/tetragonal phase transition [18,36].

Li et al. [213] reported a modified colloidal sol-gel method to obtain a ZrO₂ membrane on a self-made SiC support (average pore size 5.2 μm). Sintering the membranes at 700 and 900 °C, they obtained average pore sizes of 63 and 48 nm, respectively, with pure water permeability of 355 and 273 L m⁻² h⁻¹ bar⁻¹, respectively. Although the sol-gel method results in the formation of smooth and defect-free membranes, usually it requires expensive precursors, such as zirconium alkoxides, and organic solvents, which increase the cost and the environmental footprint [48,217]. In addition, sol-gel processes involve several steps like hydrolysis and polymerization under controlled pH [217,218], which makes it more difficult for its industrial scale-up compared to ceramic processing. This process is significantly simpler than the sol-gel method and does not involve the use of metal alkoxides making it cost-effective. Ceramic processing allows obtaining uniform UF membrane layers with tailor-made pore size [47]. Li et al. [12] prepared a 3-YSZ (yttria-stabilized zirconia with 3% molar Y₂O₃) UF membrane by dip coating a SiC support (pore size of 1-2 μm) with a suspension of particles (average diameter 50 nm). In order to achieve that, the authors firstly coated the support with a SiC intermediate layer with a pore size of 0.9 μm. The membrane sintered at 800 °C for 45 min presented an average pore size of 82 nm with a water flux of 850 L m⁻² h⁻¹. However, no filtration tests under real conditions were performed whereas the performance of developed membranes in their actual application setting needs to be tested to achieve a complete evaluation.

In this regard, an interesting procedure to evaluate zirconia membranes is in the wastewater treatment, specially hazardous effluents containing oils from many industrial processes, such as petrochemical, tanning, and leather industries, as well as cosmetics and food production [58]. It is known that ZrO₂ membranes, own to its especial surface properties [38,219], have superior performance in the treatment of stable oil in water emulsions. Specifically when chemical methods

are ineffective, *i.e.* the oil droplets have a diameter less than 10-20 μm and are in a low concentration [219,220], separations higher than 99% [220] can be achieved by filtration.

In view of what was exposed, the present chapter focuses on the development and characterization of an ultrastable ultrafiltration zirconia membrane on tubular multi-channelled SiC supports. The ceramic processing was the technique applied for fabricating the monoclinic zirconia membrane, which was then characterized focusing on material properties and filtration aspects. A pilot-scale filtration test was carried out with a simulated wastewater containing olive oil to evaluate the performance of the new membrane in potential applications for oil removal.

3.2. Materials and Methods

3.2.1. Powder characterization and dispersion studies

Two types of commercially available monoclinic zirconia (ZrO_2) powders with different particle sizes were selected to fabricate the membranes. According to the manufacturer (Imerys Fused Minerals, Germany), one powder has particle size below 1 μm (denoted as Z-1) while the other one below 2 μm (denoted as Z-2). They consist of fused zirconia ($\text{ZrO}_2 + \text{HfO}_2 \geq 98.30 \text{ \%wt}$) produced from zircon sand in an electric arc furnace at 2,600 $^\circ\text{C}$.

X-ray diffraction (XRD) patterns of the starting powders and sintered membranes were obtained with the diffractometer PW3040/60 X'Pert PRO MPD (Malvern Panalytical, Netherlands), operated at 45 kV and 40 mA with Cu-K α radiation ($\lambda = 1.5418 \text{ \AA}$).

Nitrogen adsorption-desorption isotherms were obtained on a Micromeritics ASAP 2020 (Micromeritics, USA) equipment for the determination of surface area, using the Brunauer–Emmett–Teller (BET) model, and pore size distribution, using the Barrett-Joyner-Halenda (BJH) model applied to the adsorption branch of the isotherms. Before the adsorption run, all the samples were outgassed under vacuum (residual pressure 10^{-2} mbar) at 300 $^\circ\text{C}$ for 8 h to make surface and pores available for the subsequent N_2 adsorption.

Scanning electron microscopy (SEM) analyses were carried out by using a ZEISS EVO 50 XVP microscope with LaB_6 source, equipped with detectors for backscattered electrons, secondary electrons, and energy dispersive X-ray Spectroscopy (EDS). SEM micrographs were obtained after sputtering samples with a 10-15 nm thick gold film.

Since the ceramic processing was the technique applied to prepare the zirconia membranes, the first required condition was to obtain a stable suspension of the ZrO_2 powders in water. Then, in order to determine the influence of pH, dispersant concentration, and ball milling time on the suspension stability, several zeta potential and particle size analyses were performed. Particle size was determined by laser diffraction on a S3500 equipment (Microtrac Retsch GmbH, Germany).

Dynamic Light Scattering (DLS) and Zeta potential measurements were performed on a Zetasizer Nano ZS (Malvern Instruments, United Kingdom). Briefly, powder suspensions (0.1% w/v) were prepared in ultrapure water and ultrasonicated for 10 min before the analysis. The pH was adjusted with solutions of NaOH and HCl.

As dispersants, two commercial products were selected based on previous works on zirconia dispersions [221,222]. According to the manufacturers, Dolapix CE 64 (Zschimmer and Schwarz GmbH, Germany) is a carboxylic acid-based polyelectrolyte, free from alkali, with a molecular weight 320 Da, and an active matter of 65% [223]. Duramax™ D-3005 (Dow, USA) is an ammonium salt of a polyacrylic acid with a molecular weight of 2400 Da and active matter of 35%.

3.2.2. Membrane fabrication

The ZrO₂ membrane layer was coated on highly porous multi-channeled SiC tubular supports supplied by Liqtech Ceramics A/S (Denmark). Each support has 25 ± 1 mm of outer diameter, a total length of 305 ± 1 mm, and 30 cylindrical channels of 3 mm diameter each (**Figs. 3.2a and 3.2b**). Initial screening of processing parameters and harness characterization were conducted on flat sheet SiC supports with same pore characteristics of the tubular supports. Once optimized the ZrO₂ membrane layer preparation, tubular multi-channeled SiC supports were used for the coating.

The coating suspensions were a mixture of the fine (Z-1) and the coarse (Z-2) zirconia powders (in an equal mass ratio) dispersed in deionized water added with the dispersant and the binder. Solid contents between 10 and 30 wt% were investigated. The dispersant dosage was 2 wt% in relation to the mass of added powder. Temporary binders provided by Zschimmer and Schwarz GmbH (Germany), Optapix CS 76, a polysaccharide dicarbonic acid polymer, and Optapix PAF 2, a polyvinyl alcohol preparation were investigated to allow the formation of a film in the dip coating process as well as to increase the strength of the green body (membrane layer before sintering).

All suspensions were prepared by the following method. First, deionized water and the required content of dispersant (Dolapix CE 64) were mixed in a beaker, the fine (Z-1) and the coarse (Z-2) ZrO₂ powders were then added. The suspension was kept under continuous mechanical stirring with a propeller RW 16 (IKA, China) and the pH was adjusted to 10 using a concentrated NH₄OH (30% NH₃, CAS 1336-21-6, Sigma-Aldrich, USA) solution. Next, the suspension was poured in a polyethylene bottle and milled for 24 hours with spherical 9 mm alumina milling beads to ensure homogenization. After the homogenization step, the coating suspension was poured into a beaker and the required amount of binder was added. The mixtures

were stirred continuously with a magnetic stirrer at room temperature until the end of the coating process.

The prepared ZrO₂ suspensions were deposited by dip coating on the porous multi-channelled SiC tubular supports using a homemade set-up. In brief, in the case of multi-channel membranes, the suspension were dipped into the channels of the SiC support for 30 s and then pulled out of the suspension at a controlled speed, and in flat sheet membranes the SiC support were dipped into the suspension for 30s and after that pulled out from the suspension at a controlled speed. Afterwards, the green membranes were dried overnight at 40 °C in a drying cabinet. In the case of double-coated membranes, the dip coating-drying cycle was repeated twice. Once dried, the membranes were sintered in a furnace in air atmosphere. The holding times at the set point temperature were 30 or 1 min. A sintering study was performed to find the optimum temperature to produce good grain joining and appropriate pore size. Own to confidentiality issues, the three different sintering temperatures, in the range between 1000 and 1300 °C, are reported as T-10 °C, T, and T+50 °C. This temperature range was chosen in order to guarantee the proper ZrO₂ sintering and its adhesion to the SiC support but trying to avoid cracks caused by the volume variation occurring above 1173 °C during the ZrO₂ phase transformation monoclinic→tetragonal [18,36].

Unsupported membranes were prepared from the dried suspensions, sintered under the same conditions above described. The obtained powders were characterized (specific surface area, pore size distribution, and zeta potential) using the same equipment and procedures described in item 3.2.1.

3.2.3. Membrane characterization and testing

The morphology, elemental and phase composition of the developed membrane were analysed by SEM, EDS, and XRD according to the same procedures described above. The pore size distributions of the fabricated membranes were analysed by the capillary flow porometry 3G zh (Quantachrome Instruments, USA). Prior to the measurement, 25 mm long membrane samples were filled with the wetting liquid Porofil™ (Quantachrome Instruments, USA), a fluorinated hydrocarbon with a surface tension of 16 dynes.cm⁻¹. The pore size distribution was calculated from the curves of the airflow through the wet and dry membrane as a function of the air pressure applied with a shape factor of 0.715 measured following the standard ASTM F316_03.

For scratch analyses a TABER 5900 reciprocating abramer (Taber Industries, USA) was utilized equipped with a conical diamond indenter with an angle of 120 °, with three different loads and a constant speed of 200 mm min⁻¹. Three scratch tests were done for each load and three measurements of each scratch were done by SEM.

The filtration tests were performed on a commercial pilot scale filtration set-up (Liqtech LabBrain) provided by Liqtech Ceramics A/S (Denmark). This unit consists of a feed tank, a feed pump, a recirculation pump, and a membrane module, as schematically shown in **Fig. 3.1**. The membranes were sealed using silicon O-rings and placed in a cross flow stainless-steel module. First, the permeability of the membrane was measured using pure deionized water in order to evaluate its performance at different transmembrane pressure with a cross flow of 1527 L.h⁻¹ for 10 minutes. Then, 50 L of feeds with different solutes were filtered in order to evaluate membrane performances in terms of rejection. These experiments were run at a constant transmembrane pressure of 1 bar, and cross flow of 1527 L.h⁻¹ for 15 minutes. Recovery factor was set to 90%. Samples from the feed were taken at the beginning of the experiments while samples from membrane permeate were collected at the end of the experiments. The compounds chosen for retention studies were: hemoglobin, a protein with high molecular weight that is expected to be retained by UF membranes considering their pore size; indigo blue, a dye present in many industrial wastewaters; and humic acid, a model compound for natural organic matter in the water and a model foulant. The hemoglobin concentration in retentates and permeates were determined by size exclusion chromatography (SEC) using an isocratic Agilent 1100 pump (Agilent, CA, USA) equipped with an evaporative light scattering detector ELSD D 2000 (Mandel Scientific, Canada). A gel permeation chromatography (GPC) column (300 × 7.8 mm) PolySep-GFC-P 4000 (Phenomenex, CA, USA) was used with water as the mobile phase, flow rate of 1 mL min⁻¹, and injection volumes of 20 µL. The concentrations of humic acid and indigo blue were determined considering the absorbance of the samples at 254 and 660 nm, respectively, measured with the UV-vis spectrophotometer Cary 50 (Agilent, CA, USA).

Filtration experiments to evaluate the oil removal and possible water reuse were carried out with a simulated oily wastewater. For that, an olive oil/water emulsion was prepared with 500 mg L⁻¹ of unprocessed olive oil from the Cooperativa Virgen de la Estrella (Badajoz, Spain) and distilled water. The emulsion was prepared by firstly keeping the oil and the water at high mechanical stirring for 24 h, followed by ultrasonication for 30 min. The stable oil/water emulsion was characterized by measuring droplet size distribution measured by the Dispersion analyser LUMiSizer (LUM GmbH, Germany). Initially, experiments with recirculation of the feed were carried out for determining the critical flux. Then, concentration experiments were performed to separate the olive oil from the water under the optimal condition previously determined. Samples of the feed, retentate and permeate were collected and analysed according to the standards methods for: oil content (ISO 9377-2:2000), total organic carbon ((DS/EN 1484:1997), chemical oxygen demand (DS/ISO 15705), and turbidity (DS/EN ISO 7027-1:2016).

Corrosion tests are typically performed in acid and alkaline baths in the pH range of 1-2 and 12-14, respectively [224]. These conditions are more extreme than the ones used in many industrial applications [27]. However, aggressive cleaning conditions, such as high NaOH concentrations, may be used for disinfection and fouling removal [22]. Therefore, highly aggressive conditions were applied in the tests to guarantee that the membranes are not damaged during the cleaning procedures. The corrosion experiments were carried out by placing small pieces of the membrane in two water baths at 60 °C under stirring, one containing 10 %wt of NaOH (pH>14) and the other 10 %wt of H₂SO₄ (pH<0). Samples were collected from each bath every week and characterized by SEM/EDS analysis and pore size distribution.

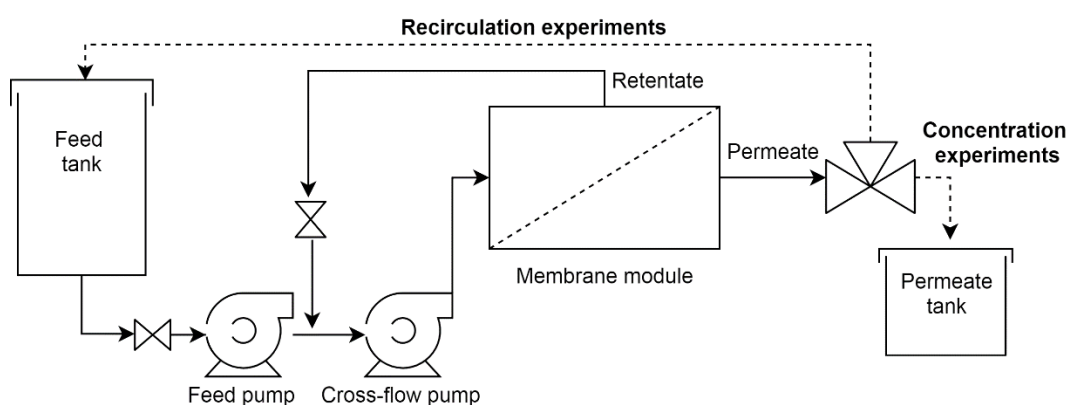


Fig. 3.1. Schematic diagram of cross-flow filtration set-up, Liqtech LabBrain.

3.3. Results and Discussion

3.3.1. Characterization of ZrO₂ powder and SiC support

The two ZrO₂ powders were used as received by the supplier: their particle size distributions were determined by DLS and shown in **Fig. A2.1a**. The average particle size of the powders Z-1 and Z-2 are 0.36 and 0.50 μm, respectively. Their specific surface areas, determined by N₂ adsorption-desorption isotherms (**Fig. A2.1b**), are presented in **Table 3.1**. These powders have a relatively low surface area as expected for fused zirconia (obtained at high-temperature arc furnace) in comparison with other kinds of synthesised zirconia [225]. No micro or mesoporosity was observed, the macroporosity responsible for the hysteresis loops observed at very high p/p^o values should be mainly caused by the empty spaces between particles.

X-ray diffraction analysis (**Fig. A2.2**) with Rietveld refinement demonstrated that the raw powders are composed mainly of monoclinic zirconia with less than 1% wt of the tetragonal phase (**Table 3.1**), in accordance with manufacturer information. Since these ZrO₂ polymorphs have different thermal expansion coefficients, it is important to have a single-phase powder to avoid cracks during sintering of the membrane. The crystallite size of the monoclinic phase are 25 nm

and 37 nm for the powders Z-1 and Z-2, respectively. Concerning the morphology of the raw zirconia powders (**Figs. 3.2c and 3.2d**), both presented relatively round particles, with a size compatible with the ones determined by DLS measurements.

Table 3.1. Characterization of the raw ZrO₂ powders.

Analysis	Particle size		X-ray Diffraction		Zeta potential		N ₂ adsorption	
	ZrO ₂ powder	D ₅₀ (µm)	D ₉₀ (µm)	%wt monoclinic	%wt tetragonal	Isoelectric point	ζ-potential at pH 10 (mV)	BET surface area (m ² g ⁻¹)
Z-1		0.32	0.62	99.1	0.9	3.8	-39.4	12.8±0.6
Z-2		0.61	0.98	99.2	0.8	3.5	-36.7	8.5±0.4

The electrical behaviour of the particles in water was similar for both Z-1 and Z-2 powders (**Fig. A2.1d**), for pH values higher than ~4, the particles were negatively charged (**Table 3.1**). The surface of ZrO₂ is rich in acid OH groups [124], which explains the negative charge observed increasing the pH.

The silicon carbide supports used for depositing the ZrO₂ layer were homogenous and free of macro-defects (cracks and pinholes), as shown in **Fig. 3.2**. According to supplier information, these supports are highly porous (around 40%) and have average pore size of 15 µm. The support pure water permeability is 12000 L m⁻² h⁻¹ bar⁻¹ [195].

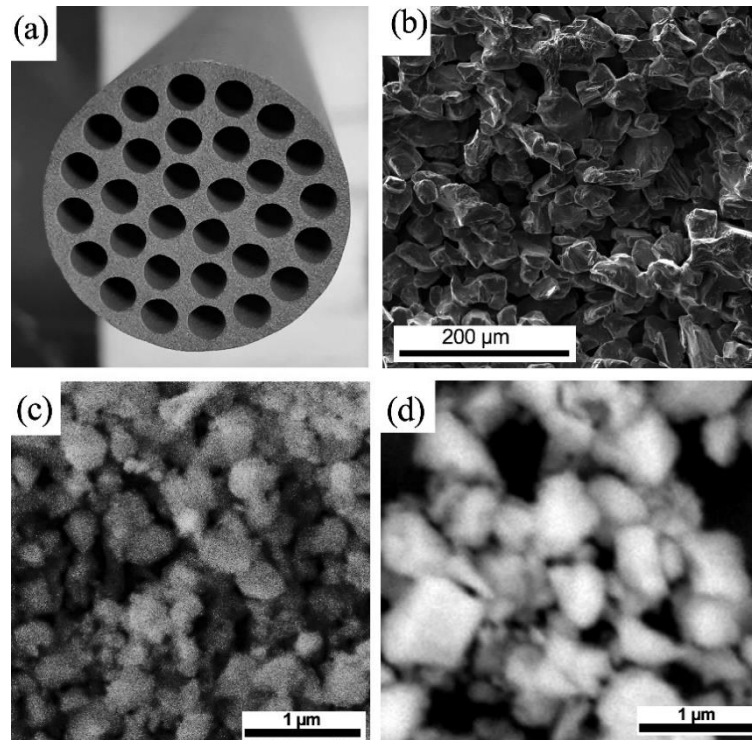


Fig. 2. (a) Multichannel tubular SiC support, (b) SEM image of the silicon carbide tubular support, (c) SEM image of the raw zirconia powder Z-1, (d) SEM image of the raw zirconia powder Z-2.

3.3.2. Optimization of the suspension

For the membrane fabrication by ceramic processing, it is essential to prepare a homogeneous and stable suspension of the starting powders, since well-dispersed particles produce higher average packing densities and a narrower pore size distribution, compared with aggregated suspensions [226] that show different shrinkages during sintering [227]. In order to optimize the ZrO₂ powder suspension, several parameters were investigated, such as the time of ball milling and the dosage of dispersant.

Particles in aqueous media tend to agglomerate because of the ubiquitous attractive van der Waals force between them [222]. A good dispersion requires to balance this force with strong repulsive forces, which can be achieved following three different procedures: i) increasing the charge at the particles surface and/or altering the pH (electrostatic stabilization), ii) adding a polymeric molecule, which is adsorbed onto the powder surface and prevents the particles physically coming close enough (steric stabilization, or iii) applying together these two effects (electrosteric stabilisation) [222,228].

The electrical stabilization generally is obtained when the absolute value of the zeta potential of the colloidal particles is 40 mV or over [228]. Analysing the zeta potential of the ZrO₂ powders (**Fig. A2.1d**), the charge is close to -40 mV at pH 10. However, without dispersant, this charge is not enough to ensure a good dispersion of the mix of Z-1 and Z-2 powders, as shown in

Fig. 3.3a, because the negatively charged zirconia particles bind with water molecules by hydrogen bonds, creating a sort of energetic interconnection leading to particle agglomeration [226]. Thus, the addition of a dispersant is necessary.

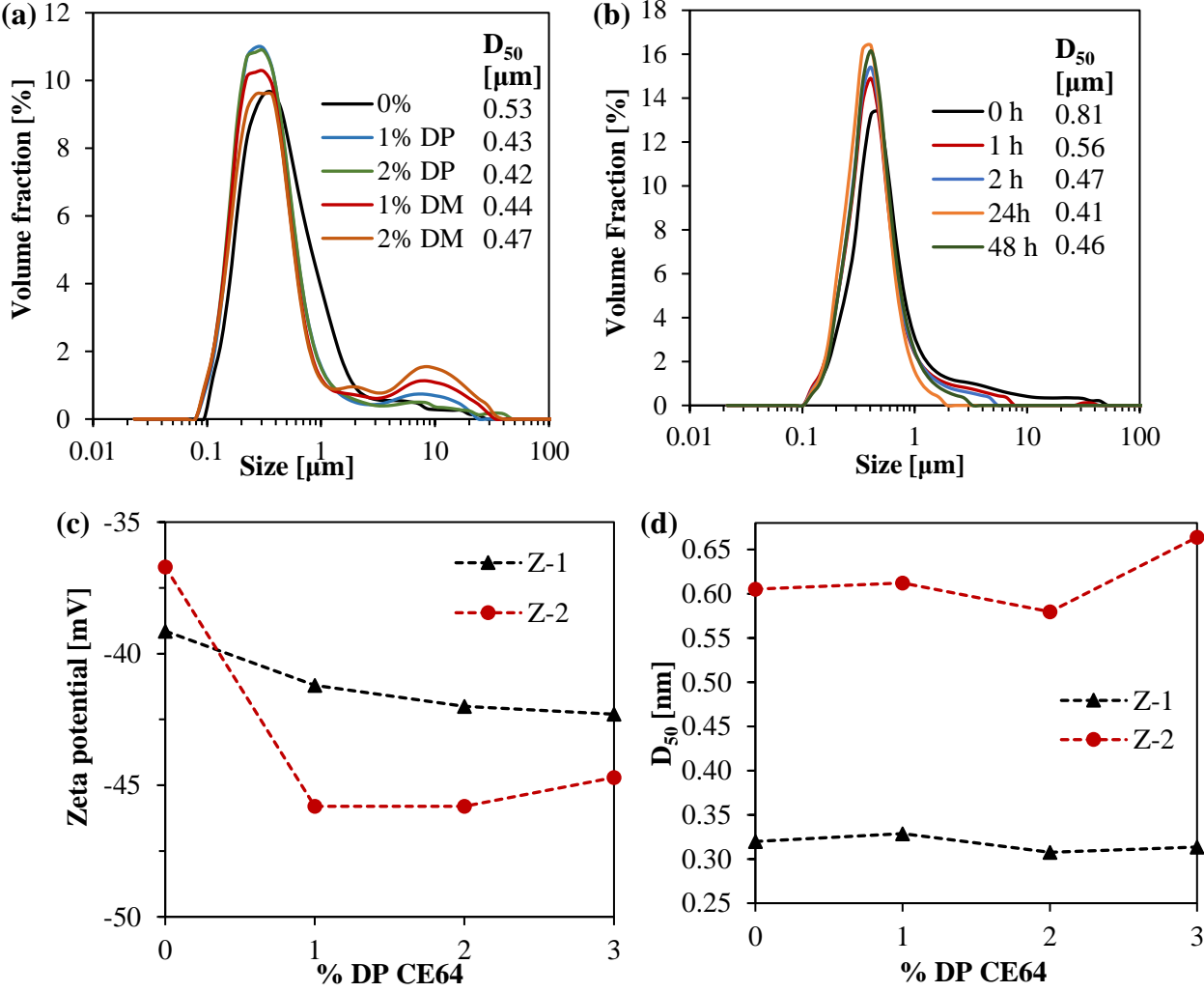


Fig. 3.3. Particle size distributions for a suspension (2.5 % wt) of the powders Z-1 and Z-2 prepared with different: (a) dispersant concentrations, at pH 10 and 24 h of milling; (b) ball milling time, at pH 10 with 2 %wt of DP. Effects of the dispersant Dolapix CE 64 (DP) dosage on the: (c) zeta potential at pH 10 and (d) D_{50} of the raw zirconia powders at pH 10. (DM: Duramax™ D-3005, DP: Dolapix CE 64).

According to the literature, several compounds can be used to disperse zirconia particles, among others: sodium or ammonium salts of polyacrylic (PAA) or polymethacrylic (PMAA) acids [50,225,229], which are fully dissociated at pH 8.5-9 [230], and carboxylic acid-based polyelectrolyte [48,49,223]. One dispersant of each class was therefore tested for obtaining a stable suspension of the mix of zirconia powders, namely Duramax™ D-3005 (ammonium polyacrylate) and Dolapix CE 64 (carboxylic acid-based). As shown in **Fig. 3.3a**, the dispersant Duramax™ D-

3005 was not adequate since it led to the formation of agglomerates with a diameter of c.a.10 μm . On the other side, the addition of Dolapix CE 64 led to a reduction of the aggregate size, and thus this dispersant was chosen for further experiments.

Since ball milling was chosen as the method of dispersing the zirconia powders mix, a study of the effect of the time of milling was performed. According to **Fig. 3.3b**, after 2 h of milling the larger agglomerates disappear, but the best interval time for homogenising the suspension achieving the proper dispersion, avoiding a too large energy consumption, was 24 h, which was chosen for the rest of the experiments.

In order to determine the optimum dosage of the chosen dispersant (Dolapix CE 64), zeta potential and particle size of the powders Z-1 and Z-2 were measured for different dispersant concentrations. For both powders, the absolute zeta potential value increased to more than 40 mV increasing the dispersant concentration (**Fig. 3.3c**), but for the powder Z-2, there was a reduction of the surface charge for concentrations higher than 2 %wt. This suggests that Dolapix CE 64 was adsorbed onto the zirconia surface, so the surface characteristics of the powder were dominated by the features of the polyelectrolyte [222], saturating the particle surface at 2% wt of concentration [223]. At the same dispersant concentration the minimum particle size of the powders was observed (**Fig. 3.3d**), whereas a higher concentration seemed to promote flocculation. The dispersant concentration of 2 %wt was therefore chosen for fabricating the membranes.

3.3.3. Membrane coating and sintering

Once obtained a good suspension, other parameters related to the coating of the support (*e.g.* binders and plasticizers, solid loading, number of coatings) were evaluated for obtaining the smallest pore size possible and a homogeneous and defect-free membrane layer, *i.e.* the basic behaviours for achieving an efficient separation by ceramic membranes [12].

The solid loading was adjusted to obtain a suspension with a specific viscosity that allows dip coating the support to form a homogeneous layer with adequate thickness. Solid loadings of 10, 15, 20, 25, and 30 %wt of the ZrO_2 powder mix (Z-1 and Z-2) were tested. Higher solid loadings led to a great increase of the suspension viscosity, as also reported by other works [223,225]. As a result, it was observed that for solid loadings lower than 20 %wt, no layer was formed after 2 cycles of support coating (**Fig. A2.3a**), caused by the excessive infiltration of the coating into the SiC support. The best results were obtained for solid loadings between 25 and 30 %wt and two coating cycles (**Table 3.2**). Two coating cycles were chosen in order to obtain a completely formed and non-defective layer (one cycle allowed producing a very thin and non-homogeneous layer, as reported in **Fig. A2.3b**), with a good permeability and no cracks (three

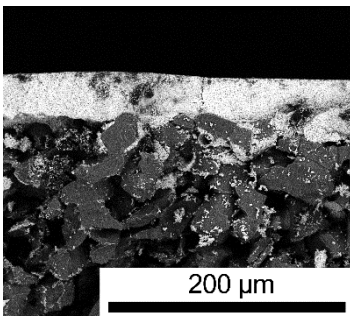
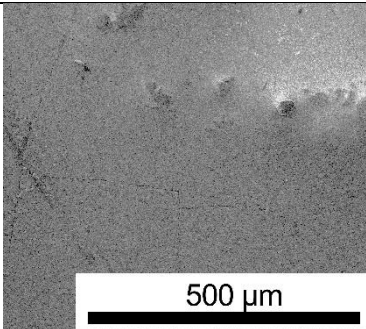
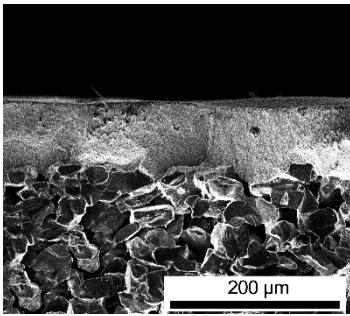
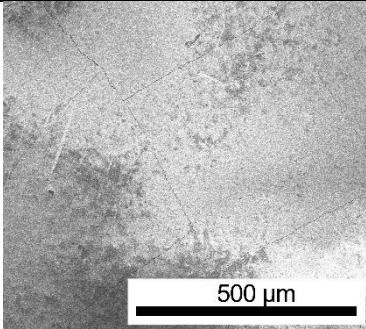
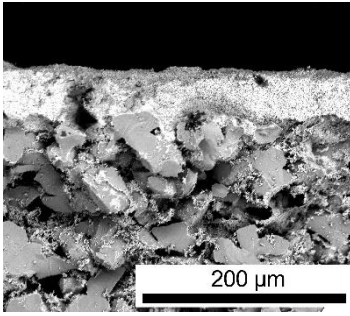
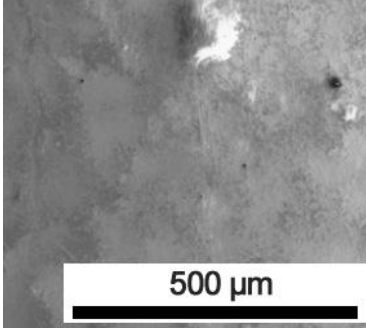
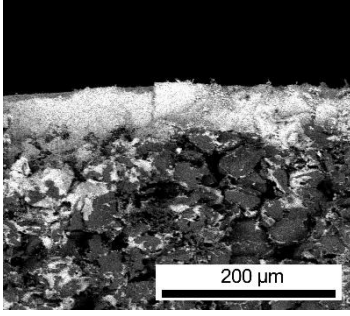
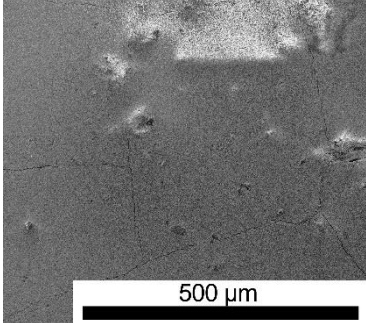
cycles allowed producing a layer quite thick, low permeable and prone to cracks during drying and/or sintering steps, as shown in **Fig. A2.3c** [231]).

In order to improve the film formation during the dip coating process, as well as to increase the green body strength and flexibility, temporary binders were added to the suspension [232]. Organic binders usually burn out above 300°C and they should burn gradually without leaving ashes. Cellulose-based (*e.g.* carboxyl methylcellulose, hydroxy-propyl cellulose) [12,233], starch-based [234,235], and polyvinyl alcohol (PVA) preparations [50,236–239] are the most used binders for fabricating zirconia membranes. The characterization of the ZrO₂ membranes obtained with the evaluated commercial binders, Optapix PAF 2 (PVA) and Optapix CS 76 (starch-based) are shown in **Table 3.2**.

It can be seen that the increase of the binder PAF 2 dosage from 2 to 4 % wt almost doubled the membrane thickness, causing more cracks and increasing the average pore size. This phenomenon is not new, as it is known that thicker layers are more prone to crack because of the critical thickness. In fact, when a wet film containing suspended colloidal particles dries on a substrate, water evaporation causes the adhesion of a film of particles on the substrate, film which resists against the deformation in the plane, although generating tensile stresses [240], only in the case the thickness is limited. Cracks are formed if the tensile stress exceeds a critical value [241] and, in general, there is a critical thickness favouring the spontaneous formation of cracks independently on the drying rate [47]. In addition to this aspect, it is known that PVA produces large pores [242], and in fact the addition of PVA-based PAF 2 caused the formation of very large pores which is disadvantageous for the performance of the membranes in the studied application.

Regarding the membranes obtained with the binder CS 76, they presented smaller thickness and smaller pores than the ones obtained with PAF 2. The optimum binder dosage was 2 % wt, leading to a membrane with the smallest average pore size (64 nm) and the smallest layer thickness ($43 \pm 3 \mu\text{m}$), homogeneous and without cracks. Given the results of these attempts, 2 %wt of CS 76 binder was chosen for fabricating the ZrO₂ membrane on the SiC supports. It can also be observed in **Table 3.2** that although the different nature of the materials used as support (SiC) and top layer (ZrO₂), the boundary between them is dense and straight, demonstrating the strong junction between these adjacent layers, for sure improving the membrane lifetime, the resistance to chemical corrosion and water hammering for fouling prevention [12].

Table 3.2. Membranes obtained with different binder and binder dosages.

Binder	Cross section	Layer thickness (μm)	Surface	Average pore size (nm)
PAF 2		49 ± 5		166
		79 ± 10		220
CS 76		43 ± 3		64
		51 ± 4		80

Once established the best binder and its dosage, a sintering study was carried out. The XRD diffractograms of the membranes sintered at the maximum temperatures of T-10, T, T+50 °C and holding times, at these temperatures, of 1 and 30 min, are shown in **Fig. 3.4** and their Rietveld refinements are presented in **Table 3.3**.

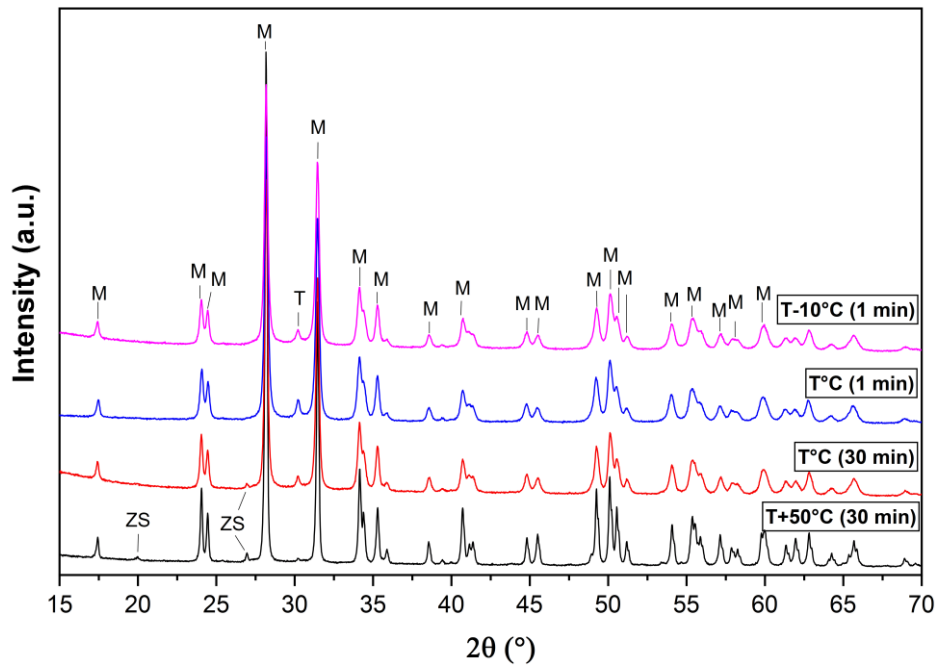


Fig. 3.4. XRD diffractograms of the membranes sintered under different temperatures and holding times (in brackets). M: monoclinic zirconia, T: tetragonal zirconia, ZS: zirconium silicate.

Table 3.3. Phase composition and size of the deposited crystals for the membranes sintered at different temperatures and holding times.

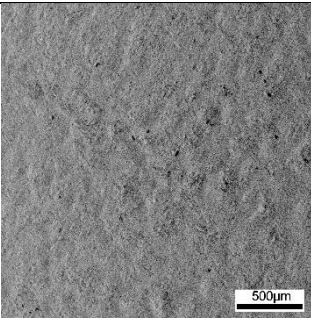
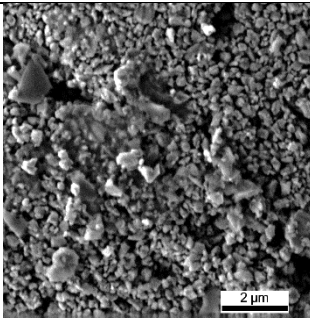
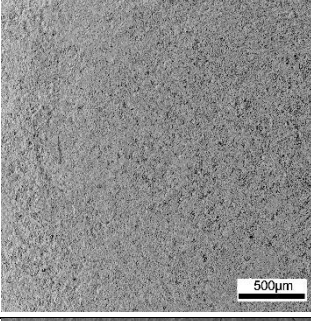
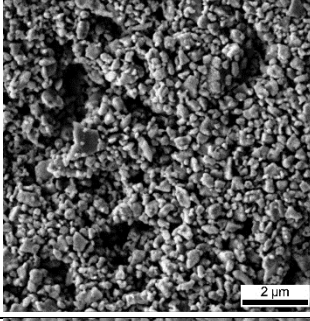
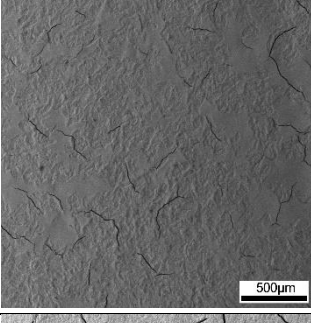
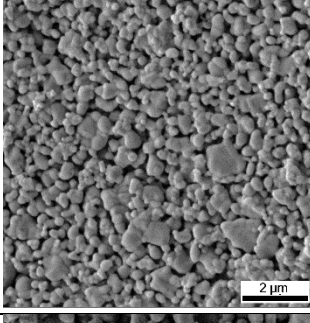
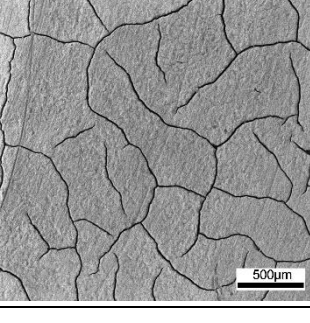
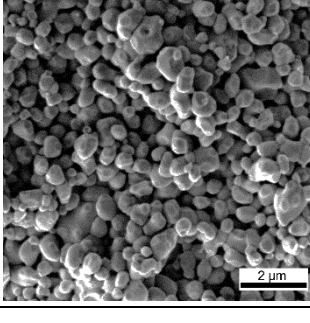
Sintering temperature (°C)	Holding time (min)	ZrO ₂		Zirconium silicate (%wt)	Crystallite size (m-ZrO ₂) (nm)
		Monoclinic (%wt)	Tetragonal (%wt)		
T-10	1	98.0	2.0	0	70
T	1	97.7	2.3	0	77
T	30	97.7	1.7	0.6	98
T+50	30	98.3	0.6	1.1	228

It can be observed that monoclinic zirconia remained the predominant phase in the membranes after sintering under the different conditions tested. The raw powders contained around 1 %wt of the tetragonal phase (**Table 3.1**). However, the increase of the sintering temperature from T-10 to T °C favoured the phase transformation from monoclinic to tetragonal zirconia, as expected considering the tetragonal polymorph is the thermodynamically stable phase at high temperature [227]. On the other hand, for the holding time of 30 min and temperatures of T and T+50, a decrease of the percentage of the tetragonal zirconia to form a third phase was observed (**Fig. A2.4**). The third phase was identified as zirconium silicate (ZrSiO₄) and it probably forms in the reaction between the ZrO₂ and small amounts of SiO₂ present in the SiC support at temperatures higher than 900 °C [243,244]. Also crystallite size increased after sintering at high

temperatures and long times, as results clearly after treatment at $T+50$ °C for 30 min (**Tables 3.3 and 3.4**).

Concerning the morphology of the membranes, it can be seen in **Table 3.4** that for sintering temperatures in the range $T-10/T$ °C with 1 min of holding time, grain coarsening mainly occurred, but the volume variation remained low enough to avoid crack generation in the resulting top layer. On the contrary, in the temperature range $T/T+50$ °C after 30 min treatment, grain coarsening and densification were observed, the particle size increased and their shape changed to reduce the surface area [227], with a consequent large dimensional shrinkage responsible for the cracks observed in these membranes (**Table 3.4**). In addition, the monoclinic phase transformation led to a considerable dimensional variation largely exceeding the maximum stress limit, causing an extensive fragmentation of the layer [227].

Table 3.4. SEM images of the surface of the membranes sintered under different conditions and their respective average pore sizes.

Sintering temperature (°C)	Holding time (min)	Surface		Pore size D ₅₀ (nm)
T-10	1			53
T	1			58
T	30			74
T+50	30			138

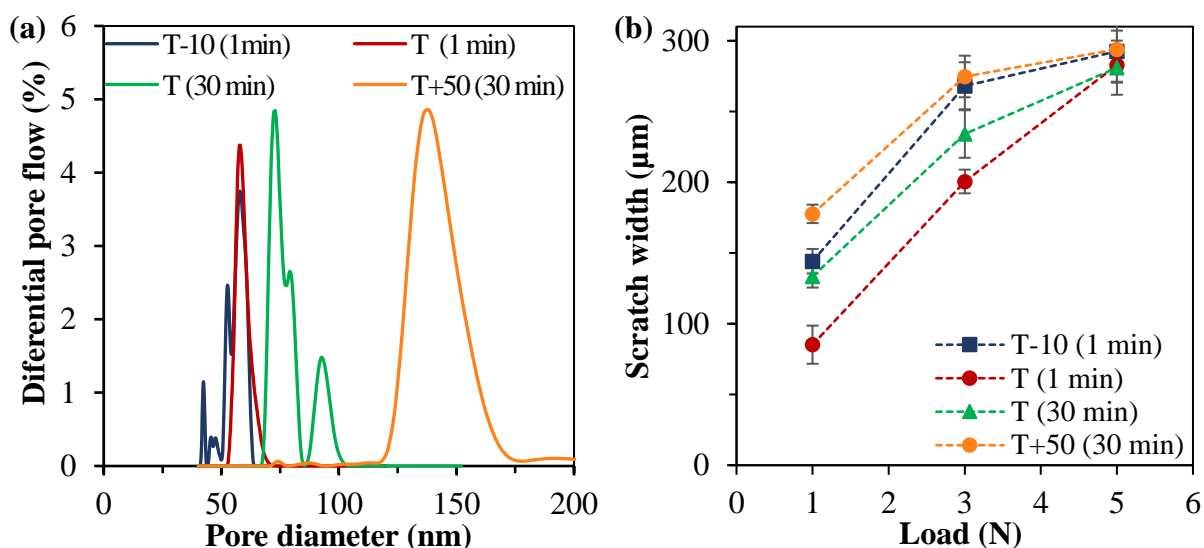


Fig. 3.5. Effect of the sintering temperatures and holding time on the: (a) pore size distribution and (b) scratch width for different loads applied.

Analogous considerations were achieved analysing the pore size distribution (**Fig. 3.5a**) and the scratch test results (**Fig. 3.5b**) of the membranes obtained at different sintering conditions. It can be seen that at T-10 °C, the sintering was not complete since a multimodal distribution of pore sizes is observed. In addition, at this temperature the membrane presented a lower scratch resistance. On the other hand, as showed in **Table 3.4**, the temperatures of T and T+50 for 30 min led to an excessive crack of the membrane, which reduces its mechanical strength and causes the larger pore size values observed in **Fig 3.5a**. In conclusion, the optimal sintering condition was at temperature T for 1 min, allowing to complete the sintering of the particles without excessive densification nor phase transformation, resulting in a pore size with a narrow Gaussian distribution and in a mechanically resistant layer.

3.3.4. Characterization of the membrane

As discussed before, the optimum membrane was obtained using a suspension with 2 %wt of binder (Optapix CS 2), performing two coatings, applying a sintering at T temperature with a holding time of 1 min. The morphological characterization of this membrane was presented in **Table 3.4**. The top layer is homogeneous, without defects (cracks and pinholes), and it has a thickness of $45 \pm 5 \mu\text{m}$ (**Fig. A2.5a**). This membrane also presented an average pore size of 60 nm (**Fig. 3.6a**), with D_{50} and D_{90} equal to 58 and 63 nm, respectively. Thus, in order to verify the composition of the developed membrane, EDS analysis was performed on the membrane surface and on its section (**Fig. A2.5bc**). The elemental analysis of the surface was 21 %wt of O and 77 %wt of Zr, indicating that the top layer is composed by pure zirconia.

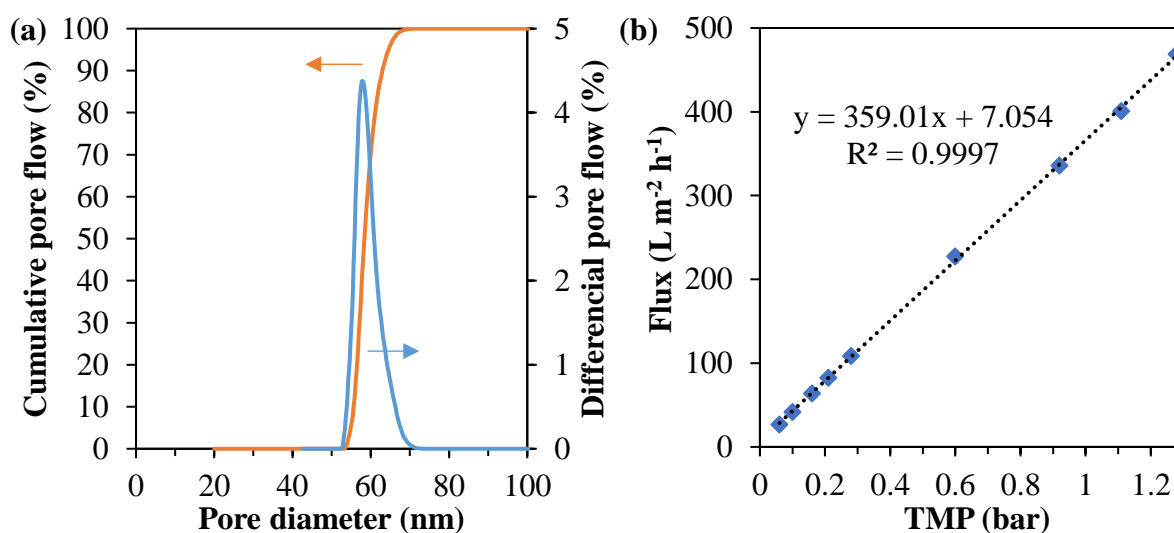


Fig. 3.6. (a) Pore size distribution of the ZrO₂/SiC membrane. (b) Pure water flux at different transmembrane pressures (TMP).

In **Fig. 3.6b** the permeate flux obtained for pure water filtration at different transmembrane pressures (TMP) is shown. A linear pressure-depended regime was obtained, as expected for pure water (non-fouling) filtration [245]. Under this regime, it was possible to calculate the membrane permeability, which is around $360 \text{ L m}^{-2} \text{ h}^{-1} \text{ bar}^{-1}$ (LMH/bar). The value obtained is similar to the permeability reported by Li et al. [213] for a zirconia ultrafiltration membrane deposited by a sol-gel route on a silicon support with pore size of $5 \mu\text{m}$. On the other hand, by ceramic processing, Li et al. [12] obtained higher clean water permeability values for a $21 \mu\text{m}$ thick ZrO₂ ultrafiltration membrane obtained on SiC supports. The result is not surprising, as thinner layers allow increasing the permeability, nevertheless in that case an additional intermediate SiC layer, increasing the fabrication cost, was considered. In the present work, a relatively thick ZrO₂ separation layer ($45 \mu\text{m}$) was required for decreasing the pore size of SiC support (corresponding to $15 \mu\text{m}$), but no intermediate layer was required.

The retention of selected compounds is presented on **Table 3.5**. Large molecules such as humic acid and hemoglobin can be easily separated, as expected considering their large size and the repulsion between their negative charge and the negatively charged ZrO₂ particles forming the filtering layer (see the zeta potential of the unsupported powder in **Fig. A2.1d**). However, also indigo blue, a quite small molecule, has a high retention, even higher than haemoglobin one, probably because it is scarcely soluble in water and forms micelles that can be easily retained by the membrane. In conclusion, the membrane under study is efficient in removing contaminants different in nature and this suggests they do not separate for simple sieving effect, but probably electrostatic interactions and dispersion forces can play additional and significant roles [246]. In

order to evaluate these roles, and taking advantage of the high hydrophilicity of zirconia [220], also oil/water separation trials were performed.

Table 3.5. Retention of selected compounds and oil removal of oil in water emulsions prepared with different oils.

Compound	MW (kDa)	Isoelectric point [247–249]	Charge at pH 7	Retention (%)
Humic Acid	4.7–30.4	3	negative	98
Indigo blue	0.262	N.A.	neutral	88
Hemoglobin	64.5	5-7	negative	82
Oil/Water emulsion with				Oil removal (%)
Motor oil				91
Crude oil (North sea)				84

These oil/water emulsions were prepared with 1 g L⁻¹ of motor oil or crude oil from the North Sea and 0.1 g L⁻¹ of the surfactant Tween 80. As a result, 91% of motor oil and 84 % of crude oil were removed. The good results obtained indicated that this membrane is also efficient for the treatment of wastewaters containing oil, such as effluents from petrochemical and metallurgical industries, as well as cosmetics and food production, tanning and leather processing [220]. Therefore, more tests were carried out in real conditions for the recovery of olive oil from water.

3.3.5. Olive oil recovery (Oil/water separation)

The olive oil/water emulsion prepared by ultrasonication was stable for several days and presented an average droplet size of 1.35 μm with the oil droplets between the limit of 0.3 and 2.7 μm (**Figure A2.6a**).

Prior to the actual olive oil/water emulsion filtration, the critical permeate flux should be determined in order to minimize the fouling during the emulsion filtration. For that, experiments were carried out with the recirculation of the permeate by setting constant permeate flowrates and assessing the variation of transmembrane pressure (TMP) for intervals of 15 minutes (**Fig. A2.6b**). The permeate flux was plotted according to the TMP (**Fig. 3.7a**): the trend observed allowed to evidence the critical flux (150 L m⁻² h⁻¹), i.e. the maximum flux that can be applied without causing significant fouling.

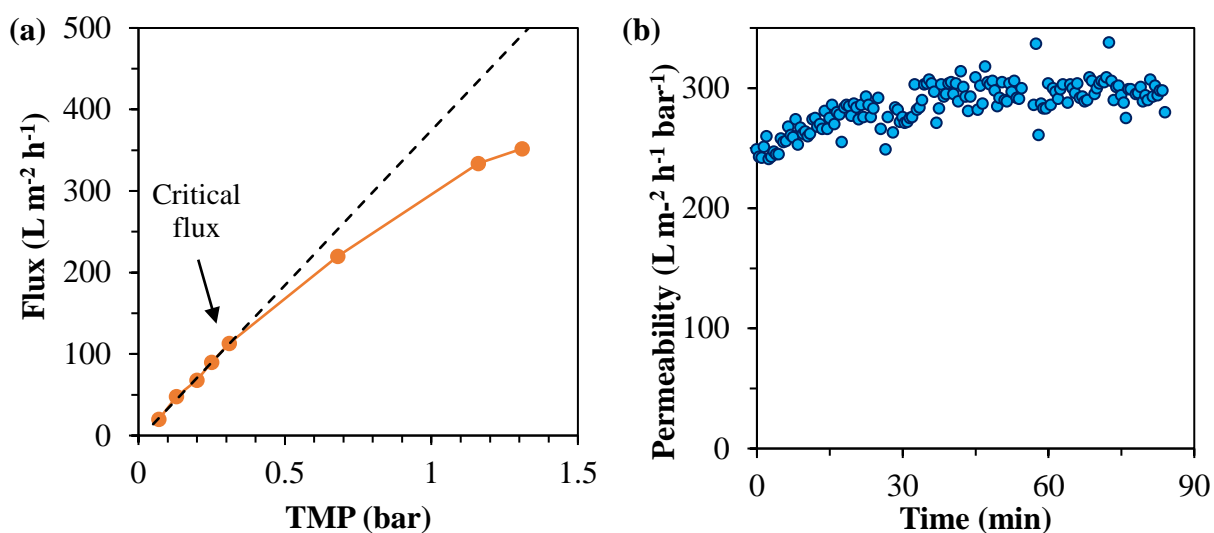


Fig. 3.7. (a) Permeate flux as a function of the transmembrane pressure (TMP) applied in the filtration under recirculation. The arrow indicates the critical flux. (b) Permeability obtained in the oil/water separation experiments with a permeate flux of 90 L m⁻² h⁻¹.

Once determined the critical flux, filtration experiments (with no recirculation of the permeate) were performed to promote the olive oil separation from the emulsion with a permeate flux of 90 L m⁻² h⁻¹. The transmembrane pressure during this test was recorded (**Fig. A2.7**) and used to calculate the water permeability, which was around 300 L m⁻² h⁻¹ bar⁻¹. As show in **Fig. 3.7b**, no considerable fouling was observed during the filtration of olive oil/water emulsion and therefore the permeability was almost constant. The analysis of the feed, retentate and permeate are shown in **Table 3.6**.

Table 3.6. Characteristics of the feed, retentate and permeate obtained in the olive oil/water emulsion filtration under the optimal condition.

	Feed	Retentate	Permeate	Removal (%)
COD (mg L⁻¹)	1,430	13,024	10.3	99.28
TOC (mg L⁻¹)	35	311	1.2	96.57
Turbidity (NTU)	89	253	1.1	98.76
Oil Content	500	4,895	0.45	99.91

As it can be observed, a removal of 99.91 % of olive oil was achieved, implying in high removals of COD (chemical oxygen demand), TOC (total organic carbon), and turbidity, which would allow the water reuse or its disposal into watercourses according to European regulations

[58]. Moreover, a retentate with a concentration factor of 9.8 was obtained, which could be processes for recovering the olive oil. In **Table 3.7**, it is presented a comparison between the membrane developed in this work and other membranes tested for oil/water separation.

Table 3.7. Comparison of different membranes applied in oil/water separation.

Reference	Type	Composition	Initial Oil concentration (mg L ⁻¹)	Water permeability (L.m ⁻² .h ⁻¹ .bar ⁻¹)	Oil removal
Present work	UF	ZrO ₂ /SiC	500	300	99.91
Fraga et al. 2017 [58]	UF	SiC	275	130	99
Eom et al. 2014 [250]	MF	Clay modified with Carbon black	100	216	96.7
Zhang et al. 2011 [251]	NF	S-Y-ZrO ₂ /PSF	80	110	99.16
Zhou et al. 2010 [219]	MF	Al ₂ O ₃ modified with ZrO ₂	1000	750	97-99.2
Chang et al. 2010 [252]	MF	Al ₂ O ₃ modified with Al ₂ O ₃	1000	250	98.5
Yang et al. 1998 [38]	MF	ZrO ₂ /Al ₂ O ₃	5000	93	99.8

As it can be seen in this table, high retentions of oil were reported by other authors, but in most of those works, the permeate flux is lower than the ones obtained with the membranes here developed. For instance, Yang et al. [38] obtained 99.8 % of oil rejection with a ZrO₂ membrane, on a α -Al₂O₃ support, with pore size of 0.2 μ m, but with a permeability of the membrane of 97 L m⁻² h⁻¹ bar⁻¹, much lower than the 300 L m⁻² h⁻¹ bar⁻¹ obtained with our ZrO₂/SiC membrane. Fraga et al. [58] tested pure SiC UF membranes but still the permeate flux was moderate. The reason for the high water permeability achieved in the present work is the unique combination of the highly porous and super hydrophilic SiC support with the ZrO₂ that is also highly hydrophilic. Although Zhou et al. [219] observed a higher permeate flux, these authors utilized a microfiltration membrane, with pores size much larger than the ones reported in the present work. In addition, a great part of the membranes applied for the oil/water separation are made of alumina (or use alumina supports), which do not have the high chemical and mechanical resistance [54] of the developed ZrO₂/SiC membrane.

3.3.6. Corrosion

The main advantage in using a SiC support with a ZrO₂ selective layer for fabricating an ultrafiltration membrane stands in the fact that both components have outstanding chemical, thermic and mechanical resistances. In order to verify the membrane resistance to highly acid and alkaline media, samples were submerged for several weeks under NaOH and H₂SO₄ solutions. As it can be seen in **Fig. 3.8**, the D₉₀ of the membranes remained almost unaffected by the treatments, proving the corrosion resistance of the membrane. Other authors [35] reported similar results for zirconia membranes, even after treatment in hydrothermal conditions, but often yttria-stabilised zirconia was used and yttrium can be easily leached in acid environment, with consequent destabilization of the material [253].

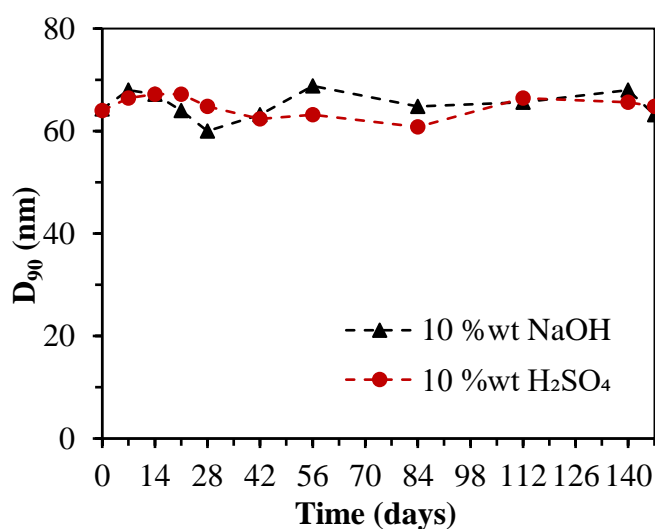


Fig. 3.8. D₉₀ (diameter in which 90 % of the pores are below this value) of the membranes subjected to acid and basic corrosion tests.

With the purpose of verifying these results, SEM imaging with EDS analysis were performed in the samples. As it can be seen in **Table 3.8**, the chemical composition of the membranes did not suffer relevant reduction of the Zr percentage, as expected for this material [253]. Furthermore, the EDS probe only detect the elements Zr, O, Si, and C (**Fig. A2.8**), confirming that the zirconia layer is chemically inert to H₂SO₄ and NaOH under the conditions tested. Although a small reduction of the C and Si amounts was noticed after the acid and alkaline baths, these changes should be related to the removal of residual C and SiO₂ present in the SiC support [156,195]. In addition, no significant changes were observed in the morphology of the samples after the corrosion tests, as shown in **Fig. 3.9**. Other authors [35] reported similar results for zirconia membranes, even after treatment in hydrothermal conditions.

Table 3.8. EDS elemental analysis of the membrane before and after 142 days in the acid and alkaline baths.

Element	Weight percentage (%)		
	Membrane after sintering	10 % H ₂ SO ₄	10 % NaOH
Zr	76.9 ±2.2	76.8 ±1.9	76.6 ±2.1
O	21.5 ±1.3	21.9 ±1.5	22.0 ±1.7
C	0.9 ±0.1	0.6 ±0.1	0.8 ±0.1
Si	0.7 ±0.1	0.7 ±0.1	0.6 ±0.2
Na	N.D.	N.D.	N.D.
S	N.D.	N.D.	N.D.

N.D. = non-detected

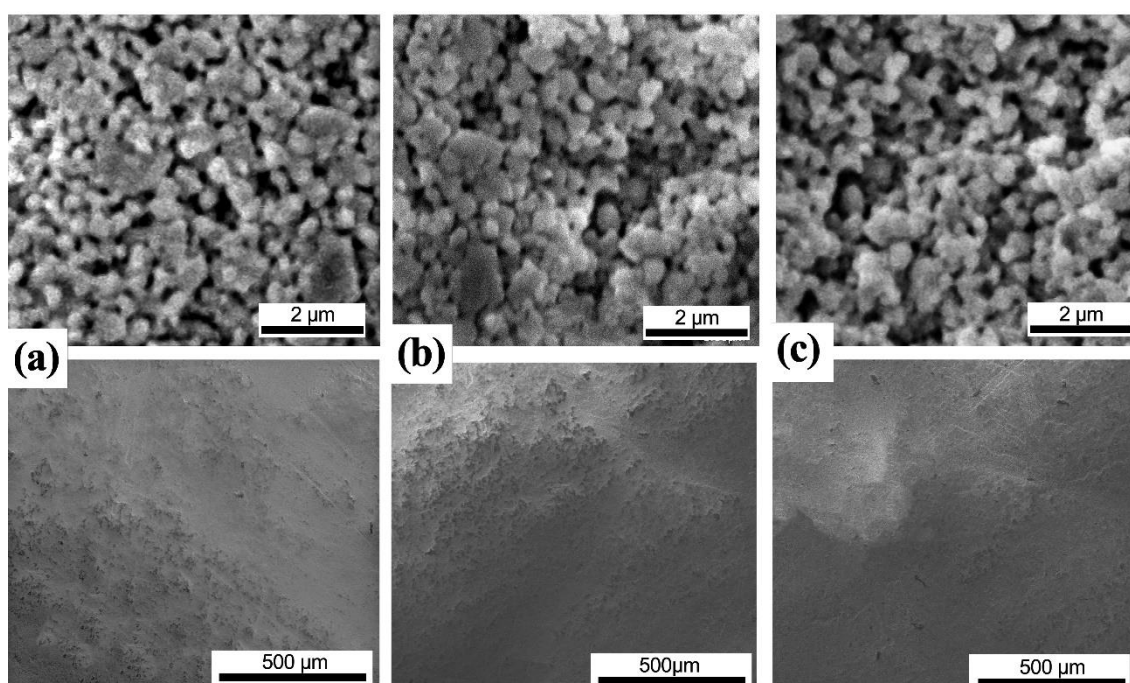


Fig. 3.9. SEM images of the membrane (a) before the corrosion test and after 142 days in the (a) acid bath and (b) alkaline bath.

In order to summarize the results obtained in this work and compare the performance of the ZrO₂ membrane here developed, it was elaborated **Table 3.9** with the few UF zirconia membranes reported in literature.

Table 3.9. Comparison of ultrafiltration zirconia membranes.

Reference	Preparation method	Support		Top layer		Sintering Temperature (°C)	Average Pore size (nm)	Water Permeability (LMH.bar ⁻¹)
		Type	Pore size (µm)	Composition	Thickness (µm)			
This work	Particle suspension	SiC	15	Monoclinic ZrO ₂	45	1000- 1300	60	360
Li et al. 2019 [213]	Sol-gel	SiC	5	Tetragonal Y-ZrO ₂	60	700	63	355
						800	57	302
						900	48	273
Li et al. 2020 [12]	Particle suspension	I- SiC	I- 1-2	Monoclinic/Tetragonal ZrO ₂	21	800	82	708
		II- SiC	II- 0.9			900	67	658
Dey et al. 2018 [48]	Particle suspension	Clay-Al ₂ O ₃	0.8	Tetragonal Y-ZrO ₂	3	700	40	48

Commercial membranes				
Company	Product	Support	Top layer composition	Average pore size (nm)
Pall Food and Drink	Membralox®	α-Al ₂ O ₃	ZrO ₂	20; 50; 100
TAMI industries	INSIDE C6RAM™	α-Al ₂ O ₃	ZrO ₂	5 to 30
Inopor	inopor® ultra	α-Al ₂ O ₃	ZrO ₂	3; 110

From this table it can be observed that the largest part of zirconia membranes is fabricated on alumina supports, which does not have the high chemical stability of the silicon carbide used in the present work [54,254]. In addition, our ZrO₂/SiC has higher water permeability in comparison to ZrO₂/Al₂O₃ membranes with similar pore size. Even though Li et al. [12] fabricated a ZrO₂ membrane using ceramic processing on SiC supports, achieving a really high water permeability, these authors needed an intermediate SiC layer before the top ZrO₂ layer, which increases the fabrication cost. On the other hand, Li et al. [213] used a sol-gel method for the direct deposition of Y-ZrO₂ layer on a SiC support but this process is more complex, expensive and has a larger footprint. In addition, yttria-doped zirconia does not have the same thermal stability of the monoclinic ZrO₂ used in this work, since yttrium can be easily leached in acid environment, with consequent destabilization of the material [253,254]. In summary, the membranes developed in the present work stands up for being fabricated by ceramic processing on SiC supports and guaranteeing corrosion resistance and high water permeability.

3.4. Conclusions

In the present work, an ultrafiltration composite membrane made of monoclinic zirconia on silicon carbide supports was developed. The optimised formulation allows to maintain the high mechanical-chemical properties of SiC, but also to reduce production costs in comparison with pure SiC UF membranes, since zirconia can be sintered in air at lower temperatures than SiC. The

composite membrane was manufactured by coating a high porous SiC support with a zirconia particles slurry prepared by ceramic processing. The optimum slurry was obtained with the aid of 2 %wt of the dispersant Dolapix CE64 followed by ball milling for 24 h and addition of 2 %wt of the binder Optapix CS 76. With two dip coating-drying cycles, a homogenous and defect free separation layer was obtained on top of the SiC supports. The green membranes were calcined in a temperature range between 1000 and 1300 °C in air, obtaining a pore size around 60 nm and a pure water permeability of 360 L m⁻² h⁻¹ bar⁻¹ after treatment at the optimal temperature. The membrane presented good retention of humic acid, indigo dye, and hemoglobin, which indicated the possibility to use this membrane in treating wastewater containing organic matter, from tanning and food industries. In a real application condition, the membrane was able to remove 99.91 % of oil from an olive oil/water emulsion, reducing also TOC, COD, and turbidity values, which would allow the water reuse. Finally, the developed membrane is mechanically strong and resistant to corrosion at basic and acid baths without changing the pore size during the time. These results indicates that the ZrO₂/SiC membrane has potential to operate in harsh conditions, such as for the treatment of heavily contaminated industrial effluents, or in food applications that require severe membrane cleaning.

3.5. Annex 2

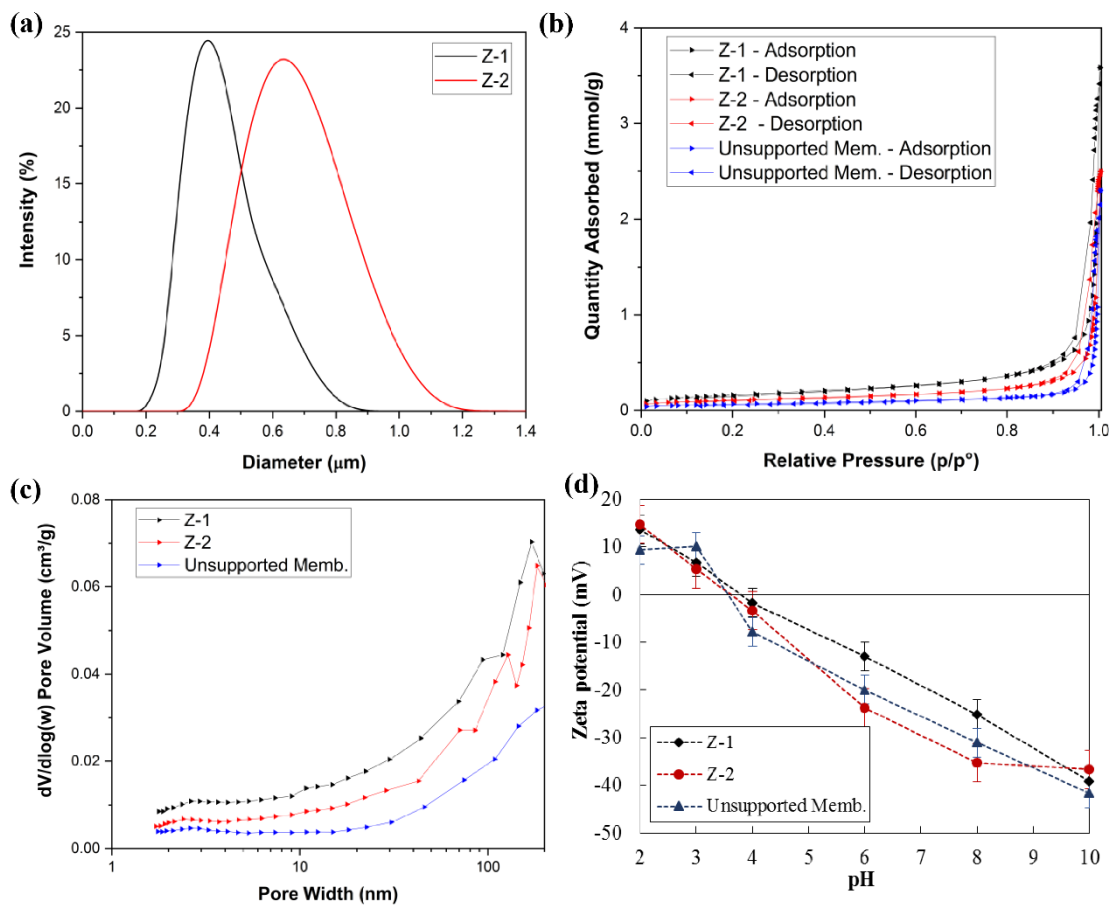


Fig. A2.1. Characterization of raw zirconia powders and unsupported membrane: (a) particle size distribution, (b) N_2 adsorption-desorption isotherms, (c) pore size distribution, (d) zeta potential curves.

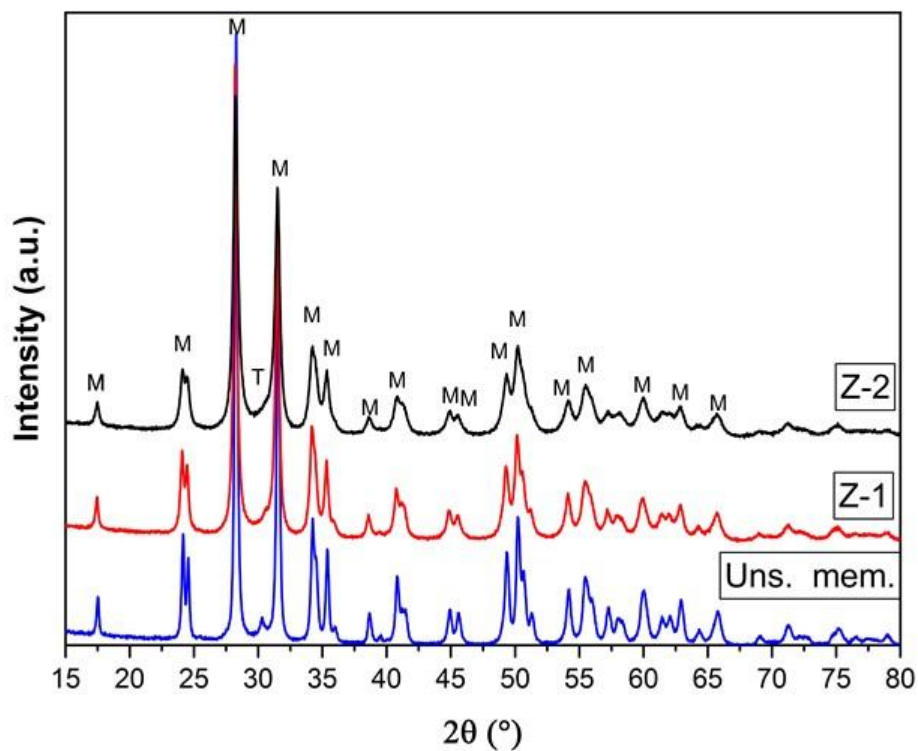


Fig. A2.2. XRD diffractograms of the raw zirconia powders Z-1, Z-2, and unsupported membrane.

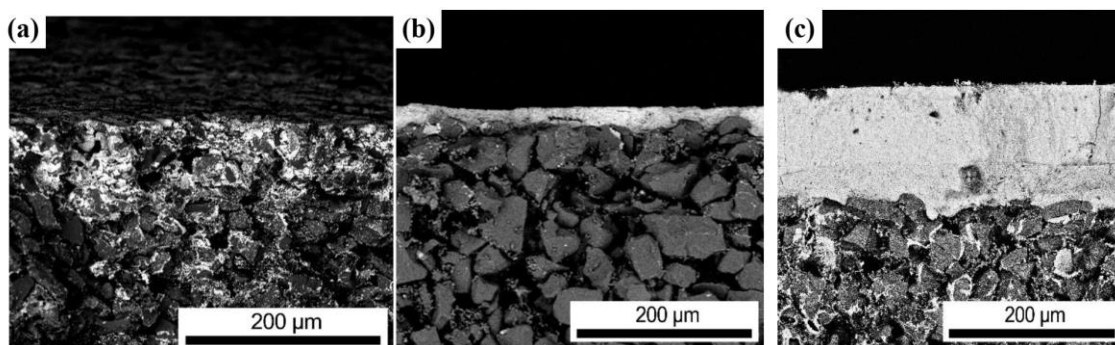


Fig. A2.3. SEM images of the cross sections of membrane obtained with a: (a) solid loading of 15 %wt and 2 coatings; (b) solid loading of 30 %wt and 1 coating; (c) solid loading of 30 %wt and 3 coatings.

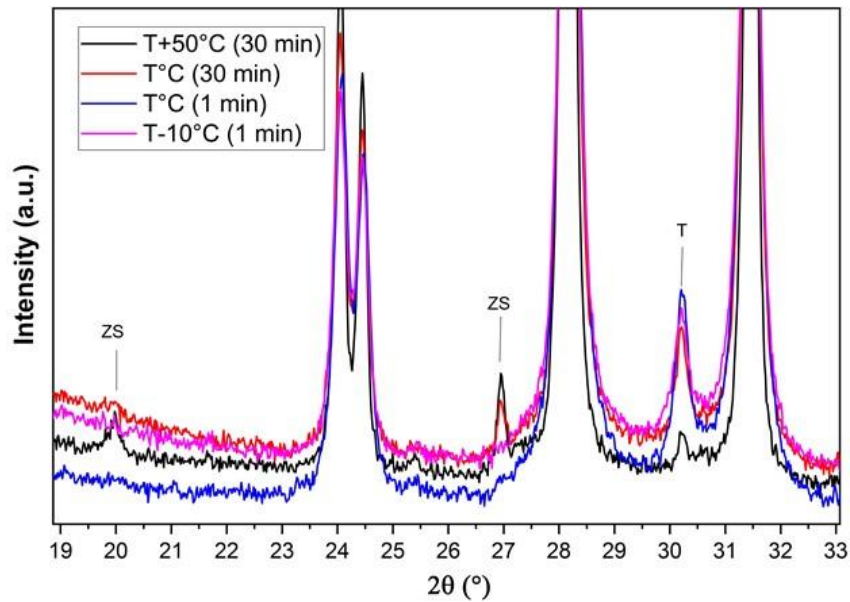


Fig. A2.4. XRD diffractograms of the membranes sintered under different temperatures and holding times (in brackets). T: tetragonal zirconia, ZS: zirconium silicate.

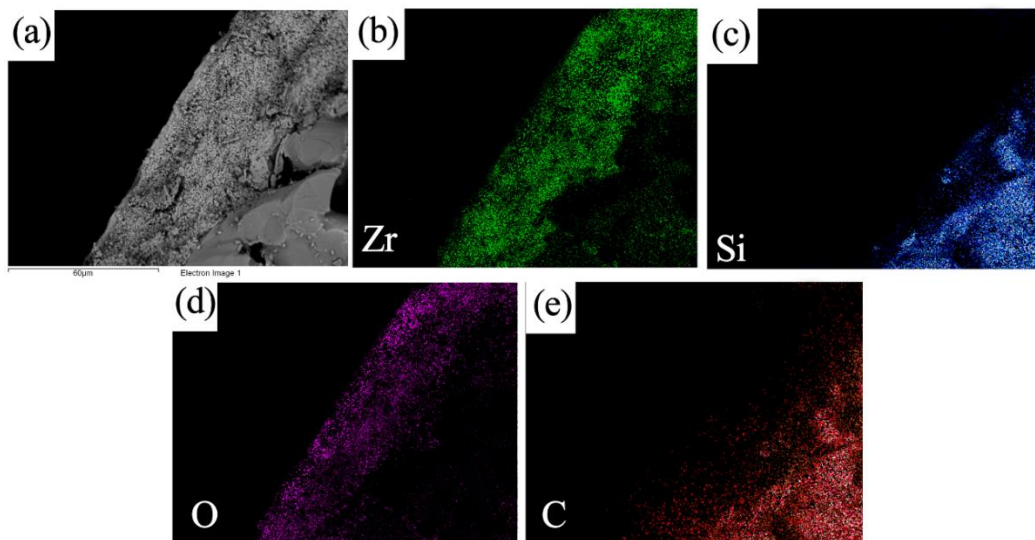
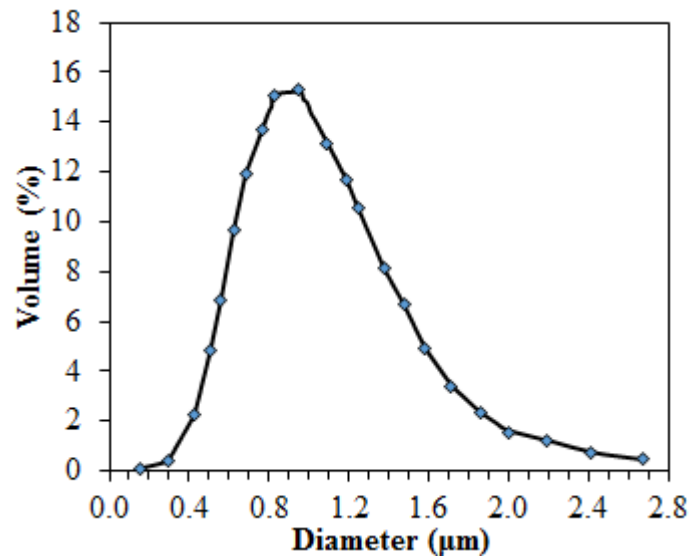


Fig. A2.5. EDS elemental analysis of the cross section of the ZrO₂/SiC membrane: (a) SEM image, (b) zirconium map, (c) silicon map, (d) oxygen map, (e) carbon map.

(a)



(b)

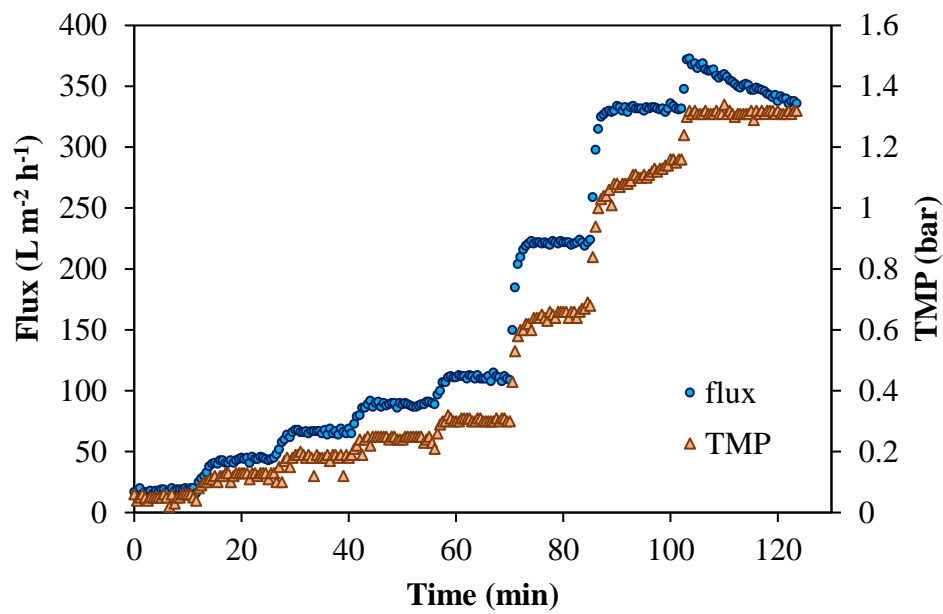


Fig. A2.6. (a) Droplet size distribution of olive oil/water emulsion; (b) Filtration of olive oil/ water emulsion under recirculation of the permeate for determining the critical flux

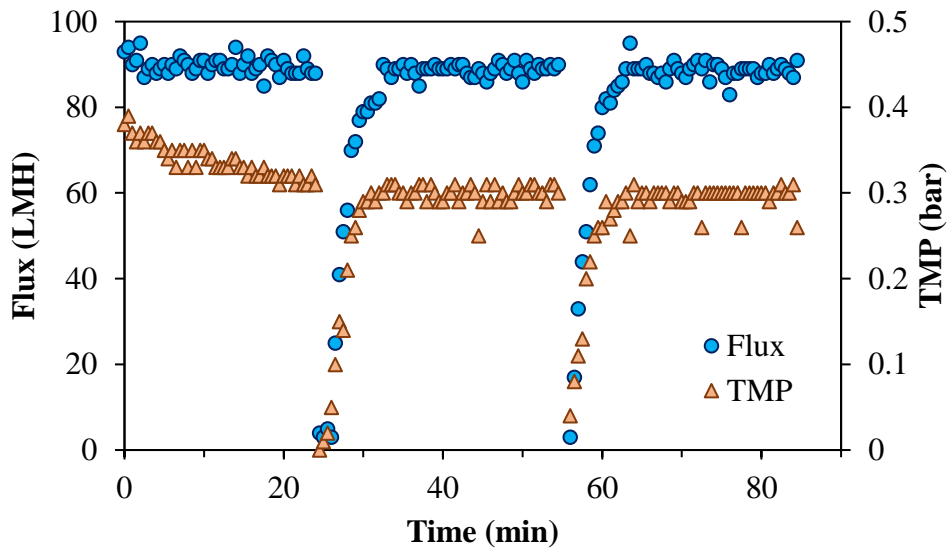


Fig. A2.7. Filtration of olive oil/ water emulsion under recirculation of the permeate for determining the critical flux.

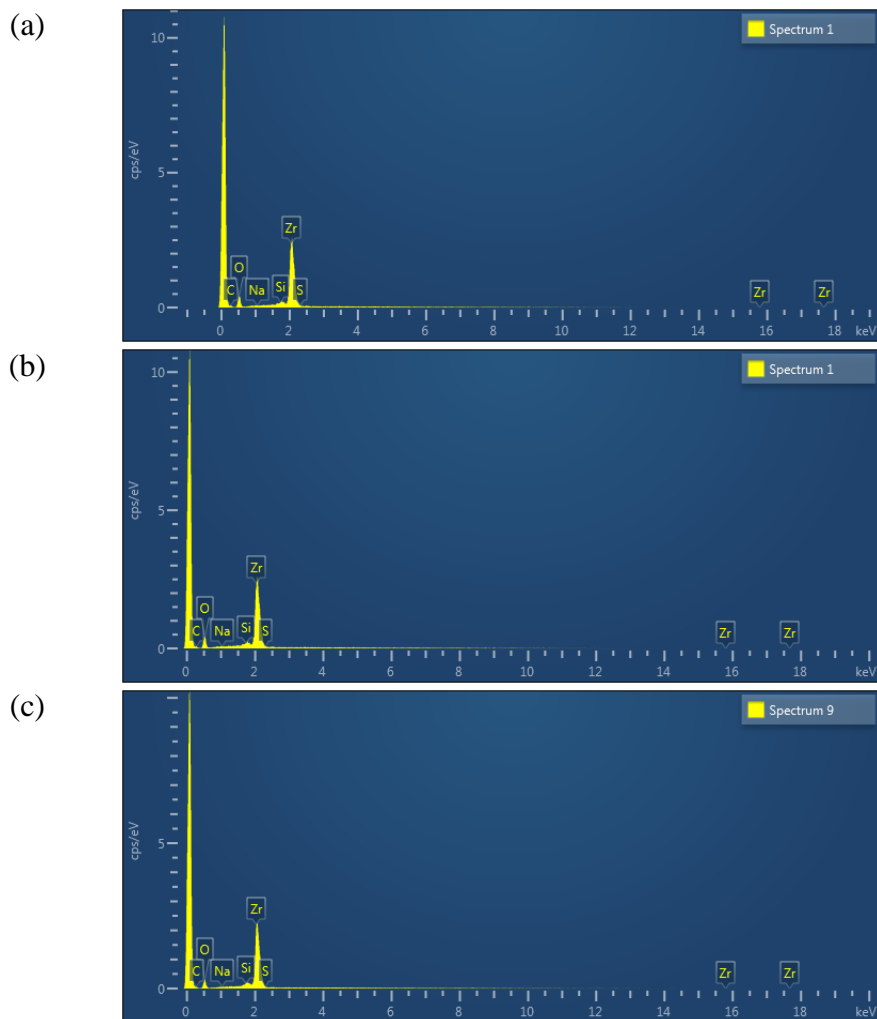


Fig. A2.8. EDS spectra of the membrane surface(a) before corrosion test and after 142 days in the: (b) acid bath and (c) alkaline bath.

4. Ce-ZrO₂/TiO₂ PHOTOCATALYTIC MEMBRANE

4.1. Introduction

To the best of our knowledge, there is no preceding study that has specifically explored the fabrication of photocatalytic membranes on SiC supports. Therefore, in the present chapter, it was studied the development of a photocatalytic membrane based on a mixture of oxides, namely cerium-doped zirconia (Ce-ZrO₂) and titanium dioxide (TiO₂) on top of the ZrO₂/SiC ultrafiltration membrane, in which the development was reported in the previous chapter. An important challenge in the preparation of small pore size membranes by sol-gel technique is the excessive infiltration of the sol particles into the support framework [255], which usually has elevated surface roughness, favouring cracks and pinholes in the membrane layer [256]. In order to solve this problem, TiO₂ P25 nanoparticles were added to the gel to prevent penetration of the sol allowing the formation of a homogeneous layer.

In this context, the present chapter has three main objectives. First, to investigate the deposition of a Ce-Y-ZrO₂/TiO₂ photocatalytic ultrafiltration membrane on a ZrO₂/SiC support, optimizing the coating and sintering conditions. Second, to characterize the membrane morphology, pore size, permeability, retention and photocatalytic activity towards phenol, a molecule that does not suffer direct photolysis [257], as model contaminant instead of the more classically used dyes [83,85,86,89,90]. Third, to evaluate the anti-fouling and self-cleaning properties of the developed membrane using humic acid as a model foulant.

4.2. Materials and Methods

4.2.1. Membrane fabrication

4.2.1.1. Support materials

The membranes were coated on highly porous multi-channelled SiC flat sheet supports with a monoclinic ZrO₂ intermediate layer supplied by Liqtech Ceramics A/S (Denmark). Each support has 100 ± 1 mm of width, a total length of 150 ± 2 mm, and 25 channels of 2 × 2 mm each (**Figs. 4.1a and 4.1b**). The support and the intermediate layer have pore sizes of 15 μm and 60 nm, respectively, no cracks or pinholes, and a smooth surface. This support is made for submerged outside-in filtration, being able to operate in a pH range from 0 to 14 and temperatures up to 800 °C, according to the manufacturer.

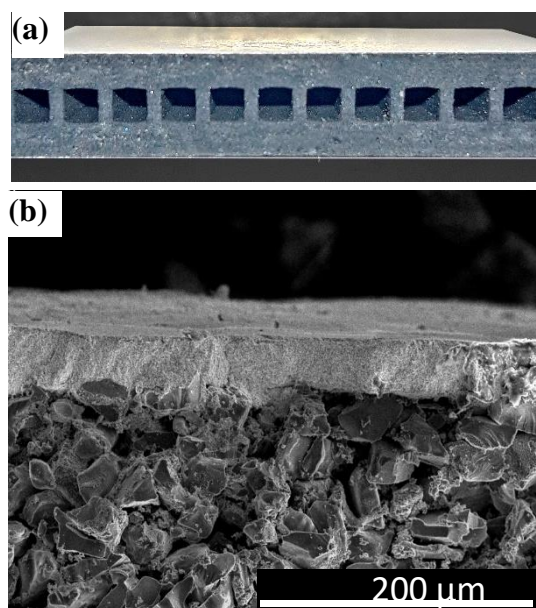


Fig. 4.1. (a) ZrO_2/SiC support and its (b) cross-section SEM image.

4.2.1.2. *Zr/Ti sols preparation and coating*

A modified colloidal sol-gel process (**Fig. A3.1**) was used to fabricate the photocatalytic ultrafiltration membrane. In a beaker, $\text{Ce}(\text{NH}_4)_2(\text{NO}_3)_6$ (CAS 16774-21-3, >98.5%, Aldrich) was dissolved in 2-propanol (CAS 67-63-0, >99.5%, Sigma-Aldrich). Next, titanium isopropoxide $\text{Ti}(\text{OCH}(\text{CH}_3)_2)_4$ (CAS 546-68-9, 97%, Sigma-Aldrich) and zirconium propoxide $\text{Zr}(\text{OC}_3\text{H}_7)_4$ (CAS 23519-77-9, 70%, Sigma-Aldrich) were added to mixture. The hydrolysis and peptization of these alcoxides were carried out with the addition of HNO_3 (CAS 7697-37-2, 65%, Sigma-Aldrich) under strong stirring. This system was brought to ebullition and kept under reflux until a completely transparent bluish sol was obtained. Yttrium nitrate ($\text{Y}(\text{NO}_3)_3 \cdot 6\text{H}_2\text{O}$) (CAS 13494-98-9, 99.8%, Sigma-Aldrich) was then added to the sol. Part of this sol was dried and the resulting gel calcined for characterization. Next, AEROXIDE[®] TiO_2 P25 powder (Evonik, Germany) was dispersed into this sol by ultrasonication. A temporary binder, based on polyvinyl alcohol (PVA), was added to adjust the coating fluid viscosity, control the infiltration of the coating into the support, and increase the strength of the green body (membrane layer before sintering). Unsupported membranes were obtained by the dried coating fluid after calcination at different temperatures ($400 < T < 700$ °C).

The Ce-Y- $\text{ZrO}_2/\text{TiO}_2$ top layer was fabricated by dip coating the ZrO_2/SiC supports into the coating fluid for a determined interval of time. The green membrane was dried overnight at room temperature and kept 1 h in a drying cabinet at 40 °C. A second dip coating and drying cycle was performed and the green membranes were sintered in air in three different temperatures (T-

50, T, T+50 °C), within the range of $400 < T < 700$ °C, with a heating rate of 1 °C min^{-1} , in order to minimize the crack formation.

The obtained sol, fired gel, coating fluid, and unsupported membrane were characterized in terms of phase composition, particle size, zeta potential and UV-Vis absorption. X-rays diffraction (XRD) patterns were obtained with a diffractometer PW3040/60 X'Pert PRO MPD (Malvern Panalytical, Netherlands), operating at 45 kV, 40 mA, with a Cu K α radiation source ($\lambda = 1.5418$ Å) and a Bragg Brentano geometry over the range $10^\circ < 2\theta < 80^\circ$. Particle size analysis and zeta potential measurements were performed on a Zetasizer Nano ZS (Malvern Panalytical, Netherlands) using principles of laser Doppler velocitometry and phase analysis light scattering (M3-PALS technique). 0.1% w/v suspensions were prepared, their pH adjusted with HCl or NaOH solution, and then ultrasonicated for 10 minutes before the analysis. Diffuse Reflectance Spectroscopy (DRS) data were recorded in the 200–800 nm range using a Cary 5000 spectrometer (Agilent, CA, USA), coupled with an integration sphere for diffuse reflectance studies, using a Cary win-UV/scan software. A sample of PTFE with 100% reflectance was used as the reference. The optical band gap energy has been calculated from the Tauc plot.

4.2.2. Membrane characterization

The morphology of the developed membranes was analysed by Scanning electron microscopy (SEM) using a microscope EVO 50 XVP (ZEISS, Germany) with a LaB $_6$ source, equipped with detectors for backscattered electrons, secondary electrons collection, and energy dispersive X-ray Spectroscopy (EDS). SEM micrographs were obtained after sputtering samples with a 10-15 nm thick gold film.

Filtration experiments were carried out in a pilot scale filtration unit, which consists of a feed tank, a recirculation pump, a vacuum pump, and a membrane module, as schematically shown in **Fig. 4.2**. The recirculation pump ensures a continuous cross flow outside the membrane, while a vacuum pump applies the transmembrane pressure to drive the filtration and collect the permeate from the internal membrane channels. The membranes were placed in a 5 L module with the top side open. First, the permeability of the membrane was measured using pure deionized water in order to evaluate its performance at different transmembrane pressures. The permeate flux was measured gravimetrically. Then, 50 L of feeds with different solutes were filtered in order to evaluate membrane performances in terms of rejection. These experiments were run at a constant transmembrane pressure of 1 bar, and cross flow of 240 L.h^{-1} for 15 minutes. Samples from the feed and permeate were taken at the beginning and during the experiments.

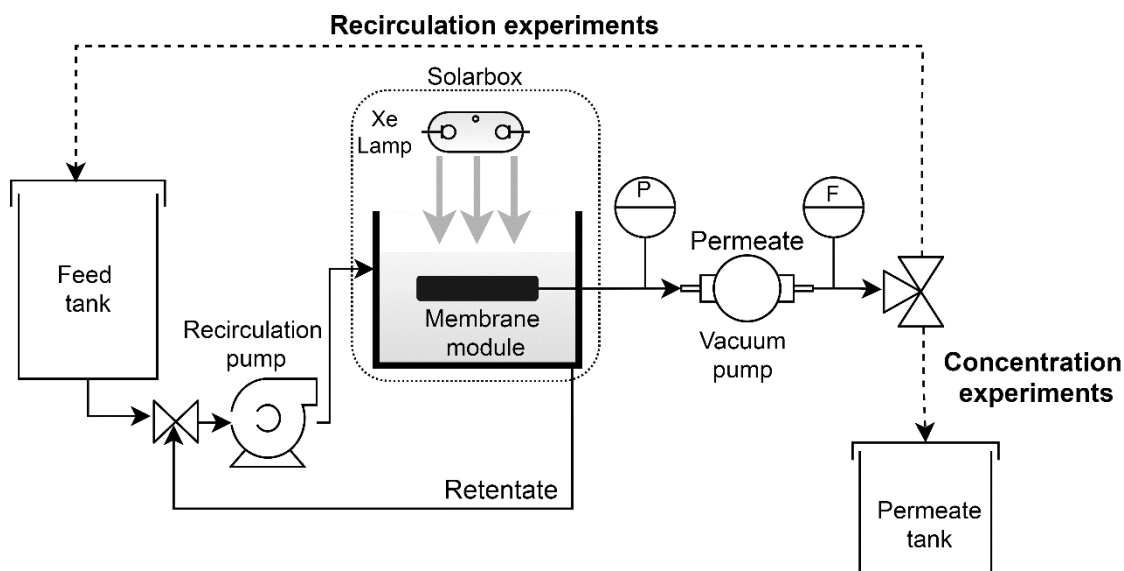


Fig. 4.2. Scheme of the experimental filtration set-up.

For the experiments of polyethylene glycol (CAS 25322-68-3, Sigma-Aldrich) retention, solutions containing 1 g L^{-1} of PEG with molecular weights of 3, 8, 20, 35, 100, and 200 kg mol^{-1} were filtered. For humic acid (CAS 1415-93-6, Sigma-Aldrich) and indigo blue (CAS 482-89-3, Sigma-Aldrich) the initial feed concentration was 20 mg L^{-1} , while for bovine serum albumin (CAS 9048-46-8, >98%, Sigma-Aldrich), hemoglobin from bovine blood (CAS 9008-02-0, Sigma-Aldrich) and whey protein from cow milk ($\geq 11\%$ protein basis, Sigma-Aldrich), 1 g L^{-1} was used. In all the tests, the initial pH was adjusted to 7, with solutions of HCl and NaOH.

The PEG and proteins concentration in retentates and permeates were determined by size exclusion chromatography (SEC) using an isocratic Agilent 1100 pump (Agilent, CA, USA) equipped with an evaporative light scattering detector ELSD D 2000 (Mandel Scientific, Canada). A gel permeation chromatography (GPC) column ($300 \times 7.8 \text{ mm}$) PolySep-GFC-P 4000 (Phenomenex, CA, USA) was used with water as the mobile phase, flow rate of 1 mL min^{-1} , and injection volumes of $20 \mu\text{L}$. The concentrations of humic acid and indigo blue were determined considering the absorbance of the samples at 254 and 660 nm, respectively, measured with the UV-vis spectrophotometer Cary 50 (Agilent, CA, USA).

4.2.3. Photocatalytic tests

4.2.3.1. Batch experiments and filtration with recirculation

The photocatalytic activity of the developed membrane was firstly evaluated in batch tests. For that, a membrane piece (4 cm length by 4 cm width) was placed into a 250 mL beaker containing 50 mL of an aqueous solution with 10 mg L^{-1} of phenol or humic acid. This system was then placed in the solar simulator SunTest XLS+ (Atlas-Ametek, IL, USA) and irradiated by a

xenon lamp, with a daylight filter, that provided a total light radiation of 365 W m^{-2} (300–800 nm), of which 30 W m^{-2} was UV radiation (300–400 nm), under continuous ventilation to keep the temperature at $25 \text{ }^\circ\text{C}$. Samples were collected in specific intervals and analysed by UV-spectroscopy, as described above, for humic acid and by ultra-performance liquid chromatography (UPLC) for phenol quantification. For that, it was used the UPLC 1200 device (Agilent, CA, USA), with a UV-DAD detector and a Poroshell 120 EC-C18 column ($3.0 \times 50 \text{ mm}$). The eluent was 95% water with 25 mM of formic acid and 5% acetonitrile at 1 mL min^{-1} . The injection volume was $100 \text{ }\mu\text{L}$ at a temperature of $30 \text{ }^\circ\text{C}$. Samples were filtered through a hydrophobic PTFE $0.2 \text{ }\mu\text{m}$ (Millipore, MA, USA) syringe filter prior to analysis. In order compare the activity of the photocatalytic membrane with the photo-Fenton reaction and the possibility to combine both processes, a series of experiments was carried out under the same conditions described above, except in the tests with phenol combined to: (i) Fe^{+2} , as a negative control experiment; (ii) Fe^{+2} and H_2O_2 , a homogeneous photo-Fenton reaction; (iii) Fe^{+2} and the photocatalytic membrane. In these experiments the Fe^{+2} concentration was 5.5 mg L^{-1} , added as $\text{FeSO}_4 \cdot 7\text{H}_2\text{O}$, and the H_2O_2 concentration was 50 mg L^{-1} .

In the photocatalytic experiments with recirculation of the permeate, the filtration set-up showed in **Fig. 4.2** was used, with the membrane module placed inside the solar simulator chamber described above. The initial feed volume was 5 L and the concentrations of phenol and humic acid were 10 mg L^{-1} in both cases. Samples of the retentate and permeate phases were collected and analysed by the same above-described procedures.

4.2.3.2. Anti-fouling assessment by humic acid filtration

The fouling behaviour of the photocatalytic membrane was investigated by filtering solutions of humic acid (20 mg L^{-1} , pH 5) in concentration experiments (no recirculation of the permeate) with the set-up, schemed in **Fig. 4.2**, placed inside the sunlight simulator described in the sub-section 4.2.3.1. For that, the permeate flow and the humic acid concentration were measured during filtration. Four types of experiments were performed to investigate the membrane fouling. First, it was carried out separately the filtrations in the dark and under light irradiation. Then, a test with 1 h intervals of filtration in the dark combined with 1 h of light irradiation was carried out. In the last experiment, the filtration was performed initially under dark, until the membrane was fouled; then, the filtration was continued under light irradiation. After each experiment, the membrane was firstly cleaned with a NaOH solution (pH 10), then with an HCl solution (pH 3), and finally rinsed exhaustively with distilled water.

4.3. Results and Discussion

4.3.1. Characterization of the Zr/Ti sols

A homogeneous and defect-less top layer is the basic premise for achieving a selective and high-quality ceramic membrane. To this aim, the coating sols were optimized to avoid the zirconia phase transformation from monoclinic to tetragonal, since the volume variation in this transformation can easily generate cracks during membrane sintering [258]. Yttrium and titanium were therefore added to the zirconia sols as doping elements in order to stabilize the ZrO₂ tetragonal phase. These sols were dried and the resulting gels calcined at the temperature T. Analysing the X-ray diffractograms of the unsupported membrane (**Fig. A3.2**), the pure Ce-ZrO₂ sample presented 90 %wt of the monoclinic and 10 %wt of the tetragonal phases. By adding 20 %mol of Ti into the Zr sols, Ce-ZrO₂/TiO₂ (Zr:Ti = 8:2), the tetragonal phase increased to 30 %wt and TiO₂ patterns was not observed in the XRD diffractogram, as reported elsewhere [97]. It is known that the addition of Ti, up to 40 %mol, to Zr sols results in the formation of a solid solution of Ti into zirconia crystals, favouring the tetragonal polymorph [94]. However, for the full stabilization of the tetragonal zirconia phase, the addition of yttrium (8 %mol Y₂O₃) to the Zr/Ti gels (**Fig. A3.2**) was needed. Ytria-stabilized zirconia (YSZ) is a well-known material crystallised in the tetragonal structure [258] that can be heated up to 1000 °C without any phase transformation [259].

Therefore, for fabricating the photocatalytic membrane, the sol with a Zr:Ti molar ratio of 8:2 and with 8 %molar of Y₂O₃ was chosen. The particle size analysis of this sol (**Fig. 4.3**) indicated nanosized particles between 2-10 nm, adequate for producing small pores ultrafiltration membranes. However, since the ZrO₂ intermediate layer on the SiC support has a pore size of 60 nm, 2 %wt of TiO₂ P25 nanoparticles were added to the coating fluid in order to avoid its excessive infiltration into the support void spaces. Moreover, the addition of solid particles into the gel network allows increasing strength and ductility of the supported layer, avoiding the gel crack during the drying and early stage of sintering [256]. As shown in **Fig. 4.3**, the addition of TiO₂ P25 particles led to the formation of agglomerates of 100 to 500 nm of diameter, as expected for dispersions in water [260].

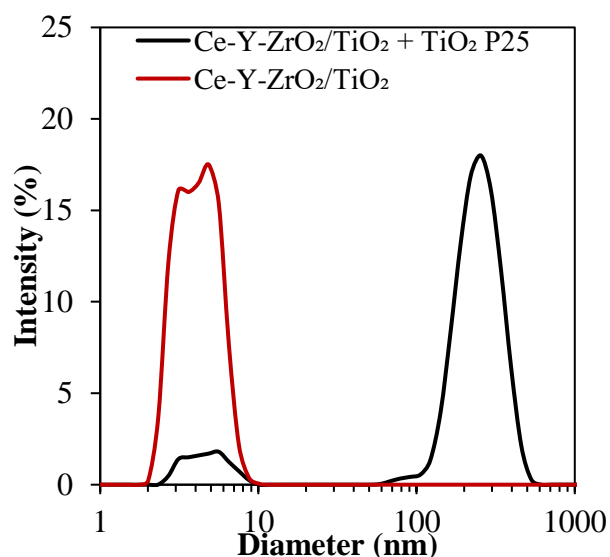


Fig. 4.3. Particle size distribution of the Ce-Y-ZrO₂/TiO₂ sol and the coating fluid, Ce-Y-ZrO₂/TiO₂ + TiO₂ P25, measured by DLS.

The optimised mixture of Ce-Y-ZrO₂/TiO₂ sol and the dried coating fluid were fired at T-50, T, and T+50 °C for studying the effect of sintering temperature. The XRD analysis of the obtained unsupported membranes (**Fig. 4.4**) indicated that the complex system affects the normal behaviours of the single components as described in the following. a) It is known that the presence of Ti causes the increase of zirconia crystallization temperature from 400 to 550 °C [94,97], which allows sintering the material at higher temperatures without losing the small pores. In fact, a firing temperature of T-50 °C was not high enough to promote the crystallization of zirconia. b) TiO₂ was present with both polymorphs, anatase and rutile, for all the tested firing temperatures, nevertheless, as it can be seen in **Table 4.1**, the ratio between anatase and rutile phases for all firing temperatures was 7:1, higher than the raw AEROXIDE[®] TiO₂ P25 ratio of 4:1 [261,262], suggesting the firing process of the complex system favoured the phase modification from anatase to rutile (thermodynamically stable polymorph) but avoiding the complete transformation expected for T > 600 °C [263], probably for a sort of stabilization effect carried out by Zr presence [94,264]. At the end of these experiments, the temperature of T-50 °C was discarded since it was not enough to promote the crystallization of the zirconia phase, required for the photocatalytic activity.

Table 4.1. Phase composition, crystallite size, and band gap (E_g) of the unsupported membrane fired at different temperatures.

Firing temperature (°C)	ZrO ₂		TiO ₂		Anatase: Rutile	Crystallite size (nm)		E _g (eV)
	Tetragonal (wt%)	Anatase (wt%)	Rutile (wt%)			t-ZrO ₂	a-TiO ₂	
T-50	Amorphous	88	12	7:1	-	33	-	
T	18	72	10	7:1	7.0	40	2.5 / 3.1	
T+50	18	72	10	7:1	7.3	48	2.4 / 3.0	

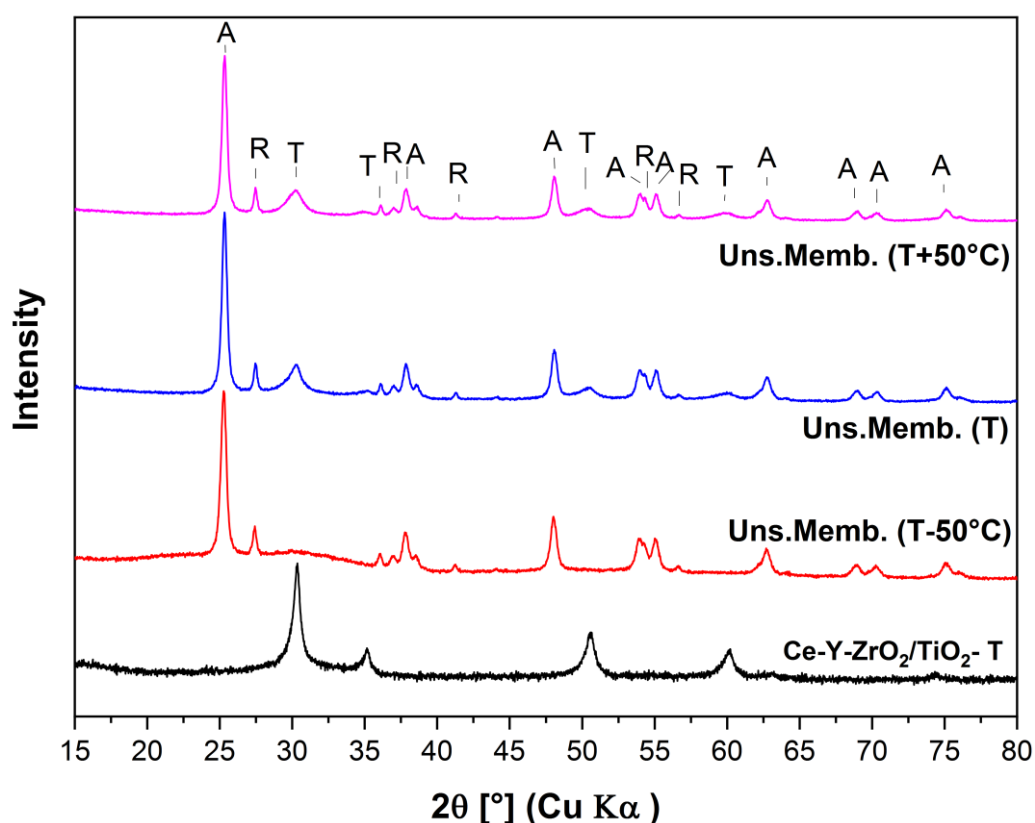


Fig. 4.4. X-ray diffractograms of the Ce-Y-ZrO₂/TiO₂ gel fired at temperature T and unsupported membranes fired at different temperatures. A= anatase TiO₂, R = rutile TiO₂, T = tetragonal ZrO₂.

The optical characterization of the fired Ce-Y-ZrO₂/TiO₂ gels (**Fig. 4.5a**) was used to estimate the band gaps of these samples through a Tauc's plot [265]. Two band gaps were observed, one around 2.5 and the other around 3.6 eV. The first one can be explained by the cerium presence, as Ce promotes a red shift of the absorption within the visible region, as reported for Ce-doped zirconia [108] and titania [266]. The addition of a small amount of cerium introduces intra band gap states that act as a bridge between the valence and the conduction band of zirconia, allowing

the absorption of low-energy photons in a double jump mechanism [108,109]. This shift reaches the visible-light region allowing this photocatalyst to work efficiently under solar light or visible LEDs irradiation [120,267]. The band gap around 3.6 eV is explained by the fact that the addition of Ti to the ZrO₂ gel reduces the pristine zirconia band gap (c.a. 5.0 eV [102]) due to the inclusion of Ti ions into the ZrO₂ lattice [103].

Regarding the unsupported membranes (Ce-Y-ZrO₂/TiO₂ gel with TiO₂ P25 nanoparticles), their optical behaviour is shown on **Fig. 4.5b**. Again, two values of band gap were observed, one around 2.4-2.5 eV caused by the Ce-doping, and another one around 3.0-3.1 eV, which correspond to the values of titania anatase (3.2 eV) and rutile (3.0 eV) [268]. The band gap of zirconia was not observed probably because with the addition of TiO₂ P25 particles, the unsupported membranes contain around 80 % wt of TiO₂ hiding the ZrO₂ signal.

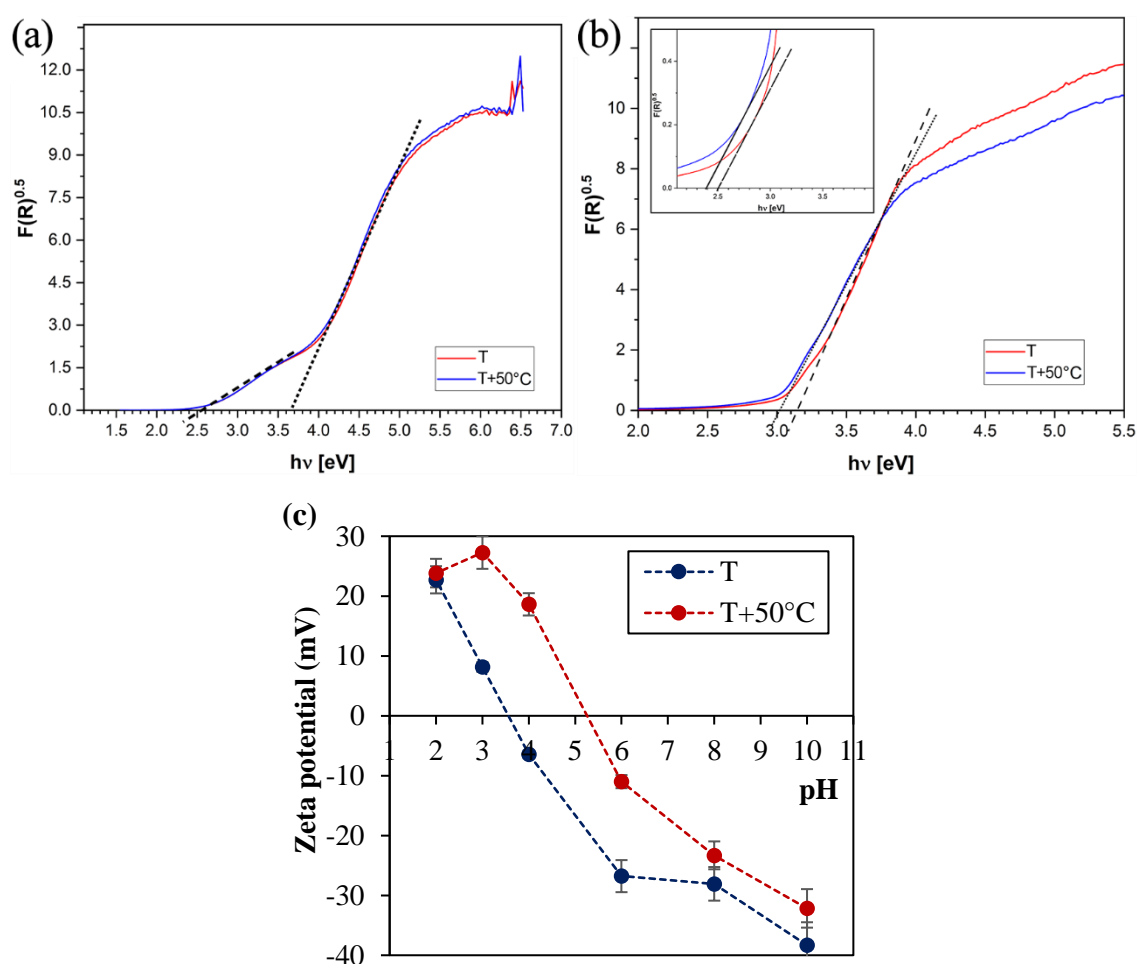


Fig. 4.5. Tauc's plot ($F(R)^{0.5}$) for the UV-vis diffuse reflectance spectroscopy of the fired (a) Ce-Y-ZrO₂/TiO₂ gels and (b) unsupported membranes. (c) Zeta potential of the unsupported membranes fired at different temperatures.

From the zeta potential measurements of the unsupported membranes (**Fig. 5c**), it can be observed that the isoelectric point of these powders is between 3.5 and 5.5, corresponding to the values expected for Ce-ZrO₂, 3.5 [110], and TiO₂, 3.5-6.5 [269]. The isoelectric point moves towards higher pH values increasing the firing temperature from T to T+50 °C. It is known that for TiO₂ nanoparticles synthesized by a sol-gel route [270], residual carbon species from the synthesis forms carbonate groups at the surface of the mixed oxide that shift its isoelectric point to lower pH values [271]. Therefore, higher sintering temperatures remove these carbonate groups and increase the isoelectric point. This effect could be considered during the process of membrane fabrication because the choice of the firing temperature could allow tailoring the membrane surface charge in two directions: improving the retention of oppositely charged molecules or improving the membrane antifouling properties maintaining the membrane at the same charge of fouling compounds (humic substances are typically negatively charged) [272]. For our purposes, a firing temperature of T is preferred in order to fabricate a membrane with a strong negative charge in a wider range of pH, but it should be also considered the possible effect of the temperature on the layer formation. Therefore, the two temperatures of T and T+50 °C will still be investigated in the following.

4.3.2. Optimization of the coating

Once characterized the unsupported membranes, the coating and layer formation processes for fabricating the photocatalytic membrane were investigated. For that, two sintering temperatures were tested, T and T+50 °C. From the SEM images of the obtained membranes (**Fig. 4.6**), it can be seen that at T+50 °C the top layer presented a considerable amount of cracks, which even led to the peeling of the top layer. As shown in **Table 4.1**, no phase transformations were observed after sintering at the temperatures of T and T +50 °C, but there was an increase in the tetragonal ZrO₂ and anatase TiO₂ crystallite sizes, therefore, the cracks observed at 600°C were most likely caused by the dimensional change of the particles in the densification process occurring during the heating. The volumetric shrinking of the layer generates tensile stresses resulting in cracks on the top layer [227]. On the other side, at the sintering temperature of T, the membrane obtained was crack-free and no peeling was observed, this temperature was thus chosen for sintering the membrane after deposition of the top layer.

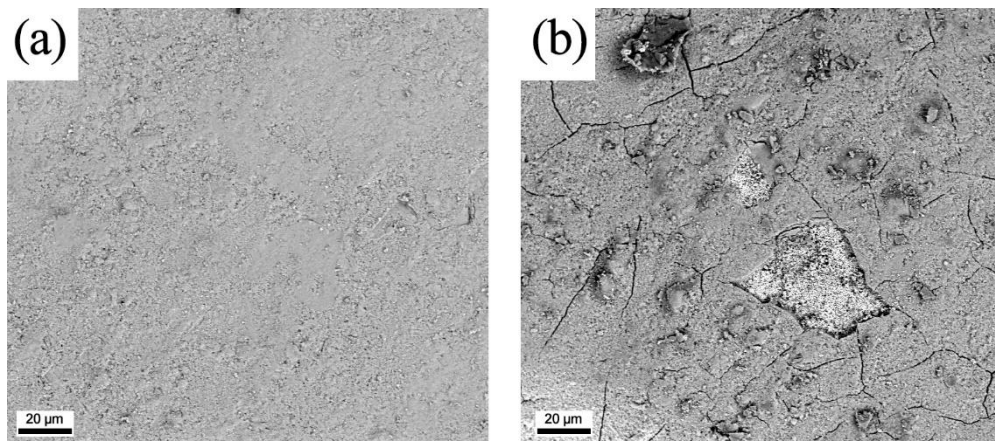
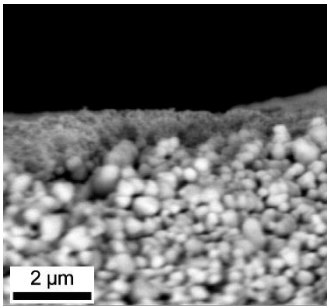
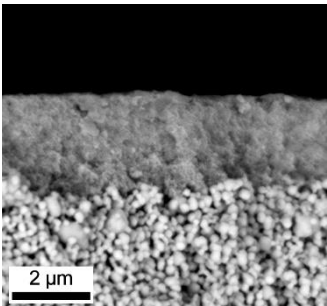
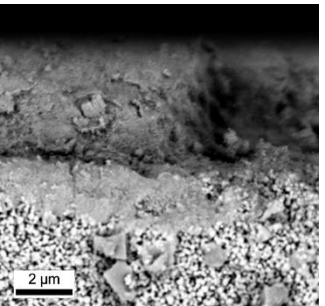


Fig. 4.6. Surface of the photocatalytic top layer sintered at the temperatures of (a) T and (b) T+50 °C. TiO₂ P25 dosage = 2% wt.

Table 4.2 reports the top layer morphology and thickness obtained with the dosages of 1, 2, 3, 5, and 10 %wt of TiO₂ P25 nanoparticles added to the coating fluid. The dosage of 1 %wt led to a thin layer not completely homogeneous and this could compromise the separation capability of the membrane. On the other hand, with 5 %wt of TiO₂, the layer was too thick and with cracks, as expected because the tensile stresses cause deformation of the layer in the plane and the consequent spontaneous formation of cracks [47,240,241]. In addition, the suspension prepared with 10 %wt TiO₂ nanoparticles was not stable. In conclusion, the dosages of 1, 5 and 10 %wt were discarded for the fabrication of the membrane.

The best membrane, homogeneous and defect-free, was obtained with 2 %wt of TiO₂ in the coating fluid, therefore this dosage was chosen for fabricating the top layer.

Table 4.2. Cross section of the membranes obtained with different TiO₂ dosages and fired at temperature T.

TiO ₂ P25 dosage	1 %wt	2 %wt	3 %wt
Layer thickness (μm)	1	2-3	4-5
Cross section			

4.3.3. Characterization of the membrane

Fig. 4.7a shows the membrane top layer, as prepared with the optimised parameters. The surface is smooth and without defects, such as cracks and pinholes. At the higher magnification (**Fig. 4.7b**), it is possible to observe the good sintering of the nanoparticles. In **Fig. 4.7c**, the typical multilayer section of the asymmetric membrane can be observed: the macroporous SiC support, the mesoporous ZrO₂ intermediate layer, and the Ce-Y-ZrO₂/TiO₂ photocatalytic top layer, which looks uniform and appropriately joined with the underneath ZrO₂ layer. The penetration of the coating fluid into the intermediate layer pores was not significant, as it can be verified in the EDS elemental mapping of the membrane cross-section (**Fig. 4.7d**), where it is possible to verify the top layer composition and the homogeneity of the membrane layer, showing a thickness of ~2 μm.

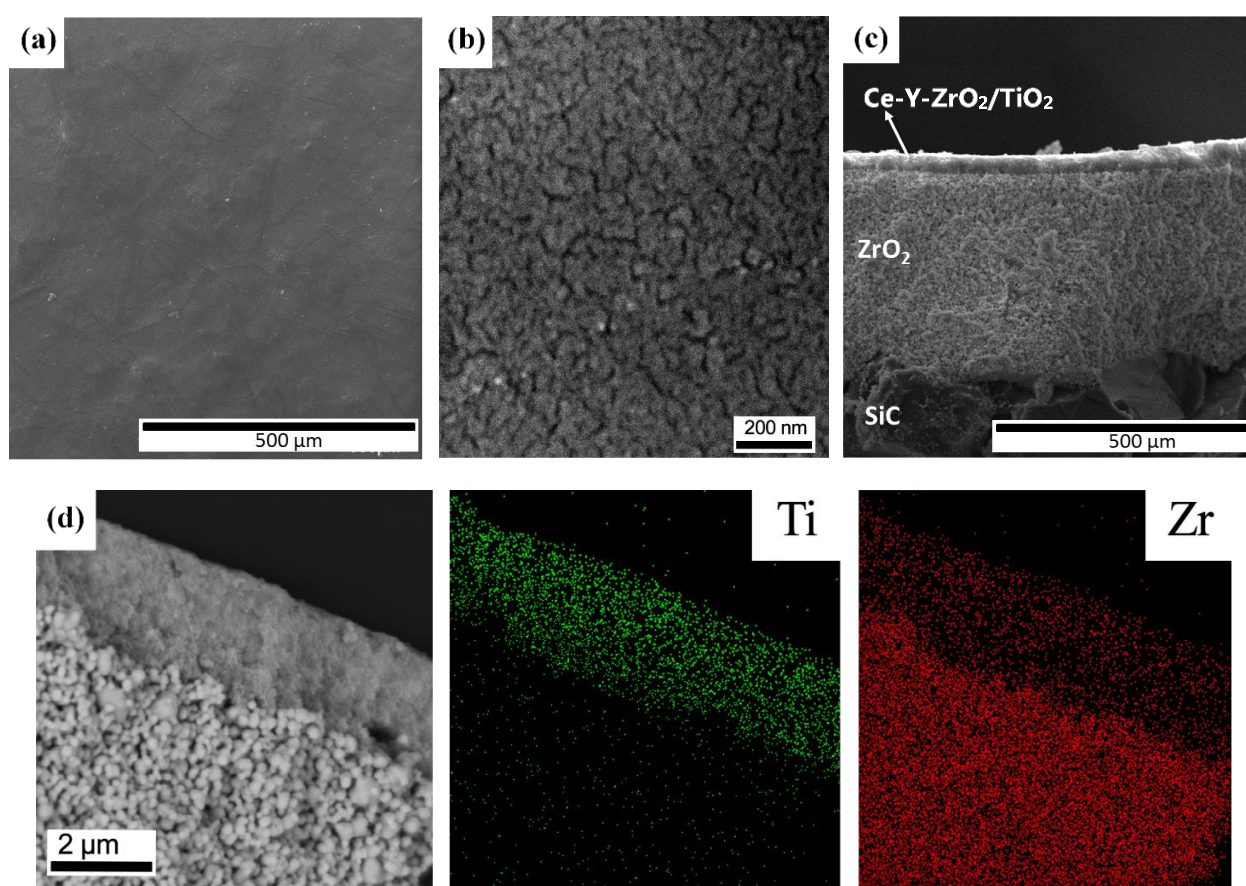


Fig. 4.7. SEM images of the photocatalytic membrane (a) surface, (b) surface at higher magnification, and (c) cross-section showing the SiC support, the ZrO₂ intermediate layer, and the Ce-Y-ZrO₂/TiO₂ top layer. (d) EDS Elemental mapping of the cross section of the membrane.

The molecular weight cut-off (MWCO) of the developed membrane was estimated using the polyethylene glycol (PEG) retention curve (**Fig. 4.8a**), a common procedure for ultrafiltration membranes [49,273]. Therefore, it was obtained a MWCO of 19 kDa, which corresponds to the

PEG molecular weight (MW) for which 90 % of the molecules are retained during filtration. The pore size of the membrane can be estimated using a correlation to convert the PEG molecular weight into pore diameter (Equation 1)[18,36].

$$d_p = 0.085 \cdot (\text{MW})^{0.46} \quad (1)$$

From this equation, it is possible to conclude that 90 % of the pores (D_{90}) of the developed membrane are below 8 nm of diameter and 50 % of the pores (D_{50}) are below 5 nm. The estimated average pore size is 6 nm. Based on these PEG retention data, this system can be classified as an ultrafiltration membrane [1], having pore sizes in the mesoporous range [256].

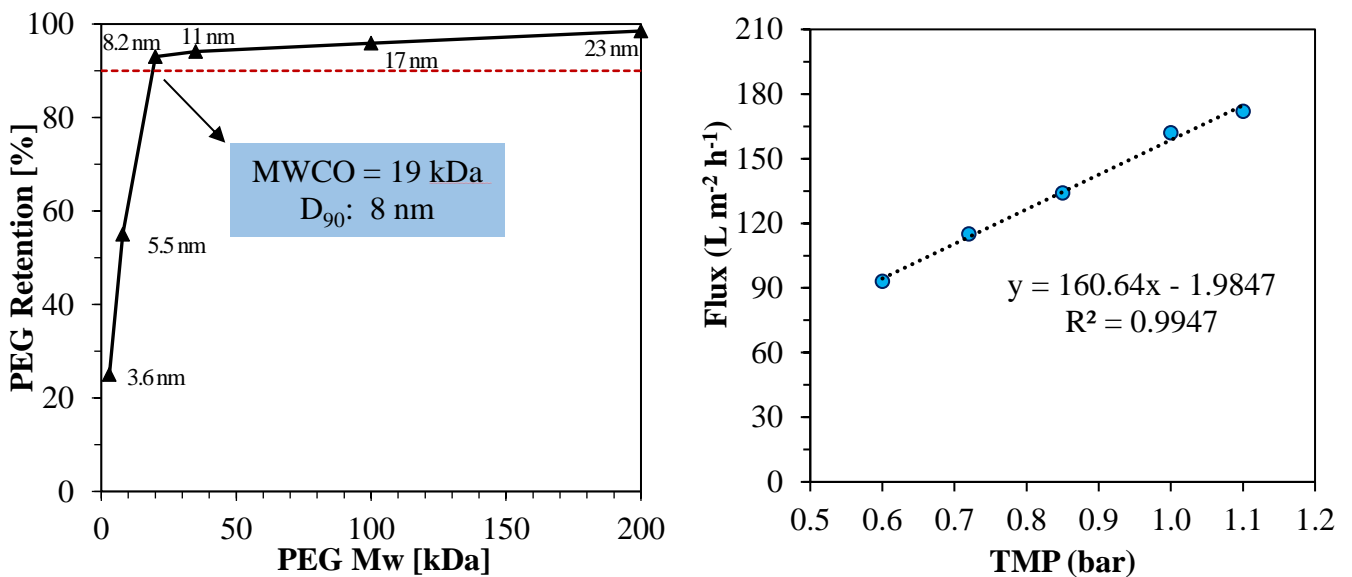


Fig. 4.8. (a) Polyethylene glycol (PEG) retention of the photocatalytic membrane and their correspondent pore diameter calculated by Equation 1. (b) Pure water flux of the membrane at different transmembrane pressures (TMP).

The retentions of selected compounds are shown in **Table 4.3**, in which it is possible to observe the high retentions of humic acid, proteins, and indigo blue. Since the developed membrane has a MWCO of 19 kDa, the sieving mechanism, in which compounds with MW higher than membrane pore size are retained on the membrane surface [274], can explain the good retentions of bovine serum albumin, hemoglobin, and whey protein. However, the sieving mechanism does not seem to be the only one driving the filtration process, as small molecules as indigo blue or the low MW fraction of the humic acid, whose dimensions should be below the membrane MWCO, are totally retained by the membrane [75]. Actually, also interfacial interactions need to be taken into account, namely electrostatic repulsions (charge effect) and

hydrophobic–adsorptive interactions [246] established between membrane surface and the solutes to be separated [274]. Indigo blue is a hydrophobic compound insoluble in water [275,276]: its retention is caused by its strong adsorption onto oxide surfaces [277] and by the consequent formation of a cake blocking the membrane pores [278]. However, the retention of humic acid can be explained by sieving effect and by the electrostatic repulsion generated by the negatively charged humic acid [247,279] and the negatively charged membrane surface at the filtration pH (Fig. 4.5c).

Table 4.3. Retention of selected compounds for the filtration at 1 bar with the photocatalytic membrane. Initial feed concentrations: 20 mg L⁻¹ for humic acid, indigo blue, and 1 g L⁻¹ for bovine serum albumin, hemoglobin, and whey protein.

Compound	MW (kDa)	Isoelectric point [90,247–249,280,281]	Charge at pH 7	Retention (%)
Humic Acid	4.7–30.4	3	negative	100
Indigo blue	0.262	N.A.	neutral	100
Bovine Serum Albumin	66	4.7	negative	92
Hemoglobin	64.5	5-7	negative	87
Whey protein (milk)	14-150	4.5	negative	87

The flux of pure (non-fouling) water was measured at different transmembrane pressures (Fig. 4.8b), resulting in a permeability of 160 L m⁻² h⁻¹ bar⁻¹, similar to the ones reported in the literature for zirconia/titania non-catalytic membranes: Larbot et al. [282] fabricated ZrO₂ membranes with pore sizes from 6 to 10 nm on α-Al₂O₃ supports, achieving water permeabilities from 175 to 210 L m⁻² h⁻¹ bar⁻¹, while Li et al. [256] obtained permeabilities of 128 to 180 L m⁻² h⁻¹ bar⁻¹ with their TiO₂ membranes of pore sizes from 3 to 5 nm on a ZrO₂ support.

4.3.4. Photocatalytic activity

The photocatalytic activity of the unsupported membrane (Ce-Y-ZrO₂/TiO₂ + TiO₂ P25) was evaluated with the photodegradation of phenol (10 mg L⁻¹) in the sun light simulator (Fig. A3.3a), following a standard procedure [87,181,283,284] taking advantage from the fact that phenol does not present significant adsorption nor direct photolysis. The experiment carried out with pure TiO₂ P25 results in 100% of phenol degradation in 150 min, but the unsupported membrane promotes 70 % of degradation in the same time, confirming the photoactivity of the

system. Compared to these data, the catalytic activity of the membrane measured in batch experiments at pH 3 and 6 and reported in **Fig. A3.3b**, is much more limited, nevertheless the results are promising considering the membrane fabrication led to the reduction of the surface area available for the catalytic process. Moreover, the photocatalytic membrane has several advantages compared to the powdery catalysts, mainly the elimination of a separation process to recover the photocatalytic nanoparticles dispersed in water [179,267]. The mechanism governing the photodegradation of organic compounds with TiO₂ has been extensively described in the literature [123,133,151,152], whereas only few works deal with the explanation of Ce-ZrO₂ activity [102,108,119], but in all cases, the semiconductor oxides (Ce-ZrO₂ or TiO₂) absorb photons promoting the photo-induced h⁺/e⁻ charge separation. Once formed, valence band holes (h⁺) can directly oxidize organic molecules and/or react with the ⁻OH anions producing [•]OH radicals that can successively oxidize the organic molecules at the catalyst surface. The superoxide anion radicals ([•]O₂⁻), generated by photo-induced electrons (e⁻) in the valence band, could also participate in degrading the organic compounds [110]. In conclusion, the reaction mechanism passes through the formation of reactive [•]OH radicals, and if we like to improve the reactivity of the system for a scale-up of the process, we should increase the production of these reactive species to increase the abatement rate. To this purpose we considered the possibility to generate hydrogen peroxide by irradiating the TiO₂ present in the membrane [285] and to use the membrane for a photo-Fenton degradation of phenol with in-situ generation of H₂O₂, realizing in heterogeneous conditions the very fast process reported in homogeneous phase in **Fig. 4.9a** [286]. As it can be seen, a great increase of phenol degradation was observed adding Fe⁺² ions to the phenol solution. In this condition the H₂O₂ generated in the membrane reacts with iron ions to generate [•]OH radicals able in degrading phenol, while Fe⁺³ ions are reduced to Fe⁺² completing the Fenton cycle. As control experiments, no degradation was observed after addition of Fe⁺². In **Fig. 4.9b**, it is shown the concentration of phenol in the feed during filtration experiments with recirculation of the permeate. Since phenol is not retained by the developed membrane because of its very small size, its concentration in the permeate remained constant in the dark filtration, but when the irradiation started its concentration decreased thanks to the photocatalytic action of the membrane.

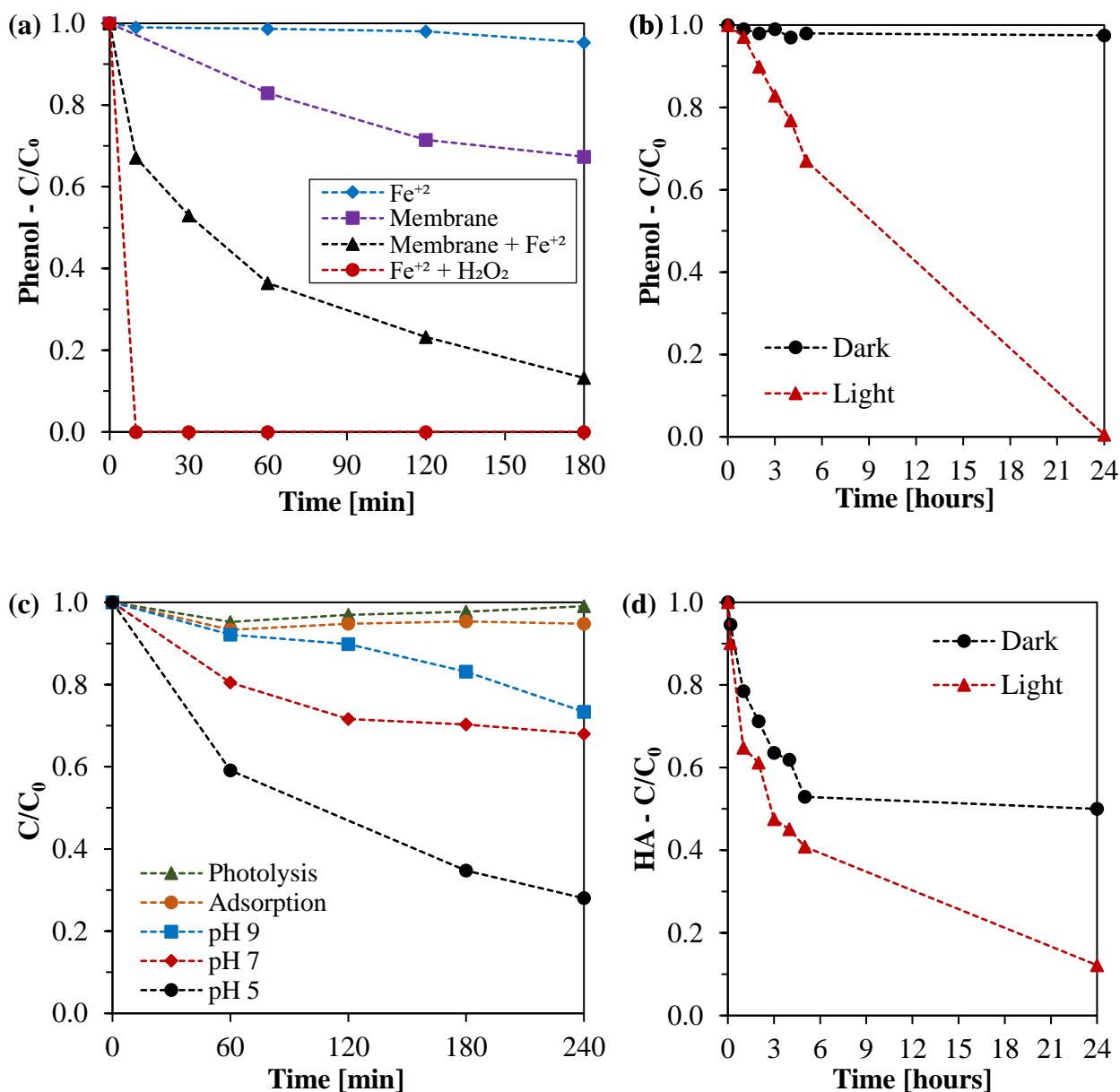


Fig. 4.9. Degradation of phenol in (a) batch experiments and in (b) filtration with recirculation. Initial phenol concentration $C_0 = 10 \text{ mg L}^{-1}$, pH 3. Degradation of humic acid in (c) batch experiments and in (d) filtration with recirculation. Initial HA concentration 20 mg L^{-1} , pH 5.

Regarding the degradation of humic acid (HA), in batch experiments (**Fig. 4.9c**), there was no significant adsorption or photolysis, but a clear effect of the photodegradation carried out by the membrane was observed. Lower pH values favoured the HA degradation, as reported in the literature [110,136]. In filtration experiments with recirculation of the permeate (**Fig. 4.9d**), HA is retained in large amount by the membrane thanks to the cooperative effect of membrane retention and cake formation, as demonstrated by the HA concentration decrease with time in the dark experiment. In the filtration under light irradiation, a higher removal of HA was observed, confirming the photocatalytic activity of the membrane. In summary, these results demonstrate the

potential antifouling effect of the developed membrane, which is able in degrading efficiently organic compounds (and retentates) under solar light irradiation taking advantage of photo-Fenton process.

4.3.5. Anti-fouling properties

Humic acid (HA) was chosen as a model compound for simulating the presence of natural organic matter (NOM) that is a major foulant during ultrafiltration of surface and wastewater [66,71]. The normalized permeate flux (J/J_0) measured in HA filtration using the photocatalytic membrane in the dark and under visible light irradiation is shown in **Fig. 4.10a**. It can be seen that the initial flux recorded in the dark has a fast decline that continues to reduce slower as the filtration continues. This trend can be explained considering the fouling caused by the HA adsorption on the membrane and blockage of the pores, with the formation of a cake- or gel-like layer on the membrane surface, as reported by other authors [71,78,287]. This layer could not be removed by water rinsing and required a chemical cleaning with a NaOH solution. On the other hand, the experiments carried out under simulated sun light exhibited a lower flux decline. After 5 h of filtration, the flux reduced to 85 % of the initial value ($119 \text{ L m}^{-2} \text{ h}^{-1}$), while for the filtration in the dark the flux was reduced to 60 % of the initial one ($105 \text{ L m}^{-2} \text{ h}^{-1}$) in the same time interval. This result can be explained considering two phenomena, both affecting the tendency of the membrane to foul [85]: the defouling caused by the photocatalytic degradation of HA on the membrane surface, expected considering the results of the previous experiments, and causing the decrease of HA in the retentate phase reported in **Fig. A3.4**, and the photo-induced super-hydrophilicity (PSH) of TiO_2 [83,84,288]. In fact, the membrane under light irradiation presents a higher hydrophilicity that favours higher fluxes and prevents fouling tendency compared to the membrane in the dark. The effect concerning the fouling can be visually observed comparing the membrane after the HA filtration in the dark (**Fig. 4.10b**) and under irradiation (**Fig. 4.10c**).

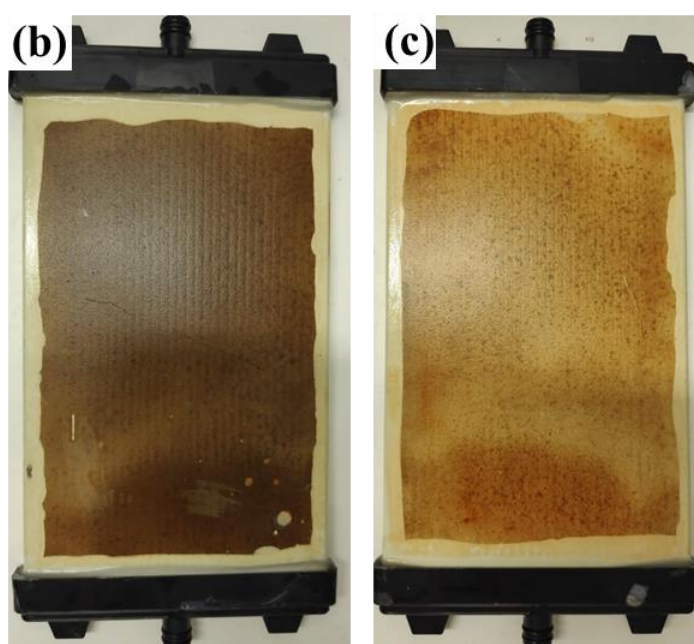
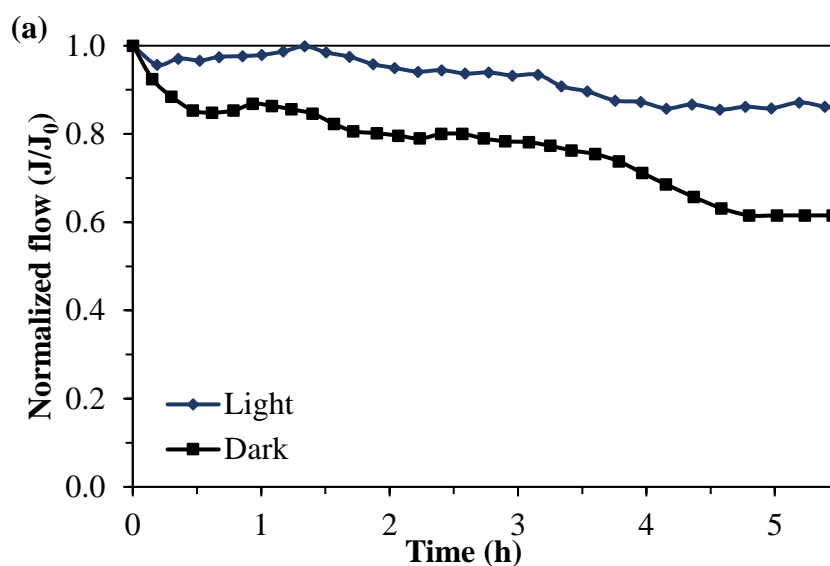


Fig. 4.10. (a) Normalized flow for the humic acid filtration in the dark, under light irradiation. Pictures of the membrane after HA filtration (b) in the dark and (c) under irradiation.

In order to confirm and proof the self-cleaning properties of the membrane, two operational conditions were tested (**Fig. 4.11**): a) approximately one-hour filtration in the dark alternated with 30 min irradiation upon simulated sun light in three following cycles, and b) the filtration carried out in the dark for the first 3 hours and then under irradiation for the following 2 hours. In the first experiment (case a), a strong flux decline was observed during the filtration in the dark caused by the HA fouling. As the membrane was irradiated, the original flux was recovered due to the HA degradation and cleaning of the membrane. In the second and third cycles of dark filtration and photo-induced cleaning, a slight decrease of the flux recovery was observed, but always 97 % of

the initial flux was reached after irradiation. In the second experiment (case b), the decrease of the normalised flux witnessed the membrane fouling observed during the 3 h of dark filtration, whereas the irradiation caused the flux recovery for the higher photo-induced surface hydrophilicity and cleaning of the membrane caused by the HA photodegradation.

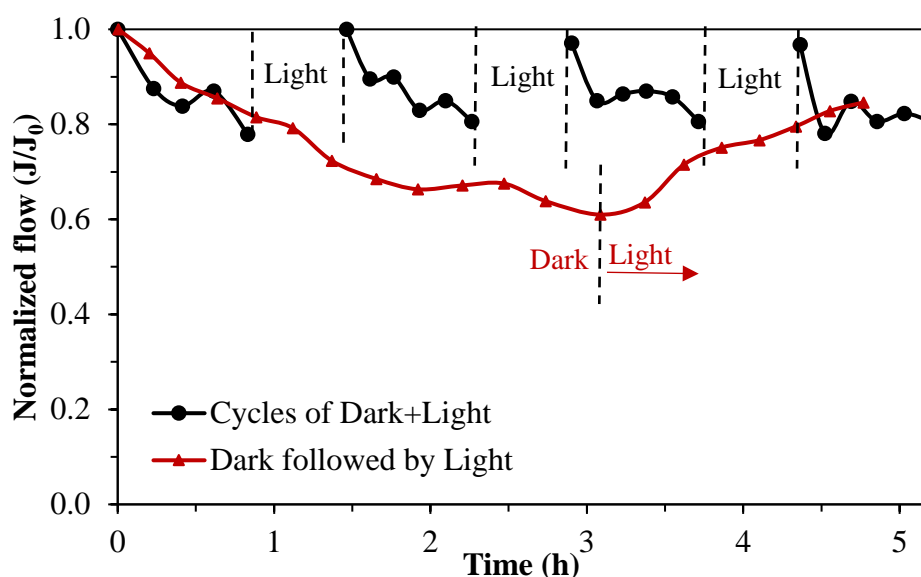


Fig. 4.11. Normalized permeate flow (J/J_0) for the HA filtration experiments with dark and light intervals.

For comparison, the performances of some ZrO_2 and TiO_2 UF photocatalytic membranes reported in literature are listed in **Table 4.4**. Apart some cases, the Ce-Y- ZrO_2/TiO_2 membrane developed in this work presents advantages with respect to most part of the membranes described in the list. In fact, in several works the photoactivity of the membranes was evaluated using dyes, although it is known that they can undergo to direct photolysis under UV light irradiation creating misunderstanding and wrong evaluations on the real activity of the membranes [257]. Also, in several cases the use of pristine TiO_2 implies the use of UV light to activate the photocatalyst. Finally, most part of the membranes present in the list exhibits a lower permeability with respect to the Ce-Y- ZrO_2/TiO_2 membrane developed in this work, although other membranes showed similar pore size range. It seems that most part of the described advantages derives from the use of SiC as membrane support as it can enhance the capacity of the active layer. Moreover, the use of a Ce-doped catalyst allows the use of visible light that favours the use of solar light for membrane anti-fouling and self-cleaning applications.

Table 4.4. Comparison of photocatalytic ceramic membranes

Reference	Top layer	Support (Pore size)	Pore size (nm)	Clean water permeability ($\text{Lm}^{-2}\text{h}^{-1}\text{bar}^{-1}$)	Photocatalytic test	
					Contaminant	Light source
This work	Ce-Y- $\text{ZrO}_2/\text{TiO}_2$	SiC (15 μm) + ZrO_2 (60 nm)	6	160	Phenol and Humic acid	Simulated sunlight (300-800 nm)
Taavoni-Gilan et al. [89]	$\text{TiO}_2/\text{ZrO}_2$	$\alpha\text{-Al}_2\text{O}_3$ + TiO_2	4	5	Methyl violet dye	UV
Goei et al. [83]	TiO_2	Al_2O_3	<10	155	Rhodamine B	
Goei et al. [84]	Ag- TiO_2	Al_2O_3	N.A.	123	Rhodamine B + Bacteria	UV (365 nm)
Mendret et al. [85]	TiO_2 / Al_2O_3	Al_2O_3 (200 nm)	<200	200	Acid Orange 7	
Alias et al. [71]	TiO_2	Al_2O_3 / SiO_2	N.A.	50-100	Humic acid	UV
Zhang et al. [86]	TiO_2	Al_2O_3 (200 nm)	50-100	400	Direct Black 168	UV (365 nm)
Zhang et al. [91]	Si- TiO_2		<60	N.A.		
Manjumol et al. [90]	TiO_2	Al_2O_3 (1 μm)	11	215	Methylene blue	UV

4.4. Conclusions

In the present work, a photocatalytic Ce-Y- $\text{ZrO}_2/\text{TiO}_2$ ultrafiltration membrane on ZrO_2/SiC supports was successfully prepared by a modified sol-gel process. The top active layer was uniform and defect-free with a thickness of 2 μm . Its composition was tetragonal zirconia, anatase and rutile titania. The membrane presented a MWCO of 19 kDa, equivalent to an average pore size of 6 nm, and a high clean water permeability, 160 $\text{L m}^{-2} \text{h}^{-1} \text{bar}^{-1}$. High retention of proteins (bovine serum albumin, whey protein, and hemoglobin), indigo dye, and humic acid were achieved, favoured by the high hydrophilicity and negative surface charge of the membrane. In photocatalytic experiments, the developed membrane was able to degrade phenol and humic acid under simulated sun light irradiation. In humic acid filtration tests, the membrane presented better anti-fouling properties (smaller flux decline) and higher permeate flux under irradiation compared to the filtration in the dark, as a result of the HA photodegradation and the light-induced superhydrophilicity of the TiO_2 top layer. Consequently, the membrane can operate longer without chemical cleaning, reducing the operational cost, and the process footprint. In addition, the membrane presented self-cleaning properties, being able to recover up to 97% of the original flux by exposing the membrane to simulated sun light. In conclusion, these results point to the relevance of deepening the investigation of potential applications of the developed membranes in innovative

treatments for drinking and wastewaters by combining filtration and advanced oxidation processes for the abatement of contaminants of emerging concern in the presence of natural organic matter.

4.5. Annex 3

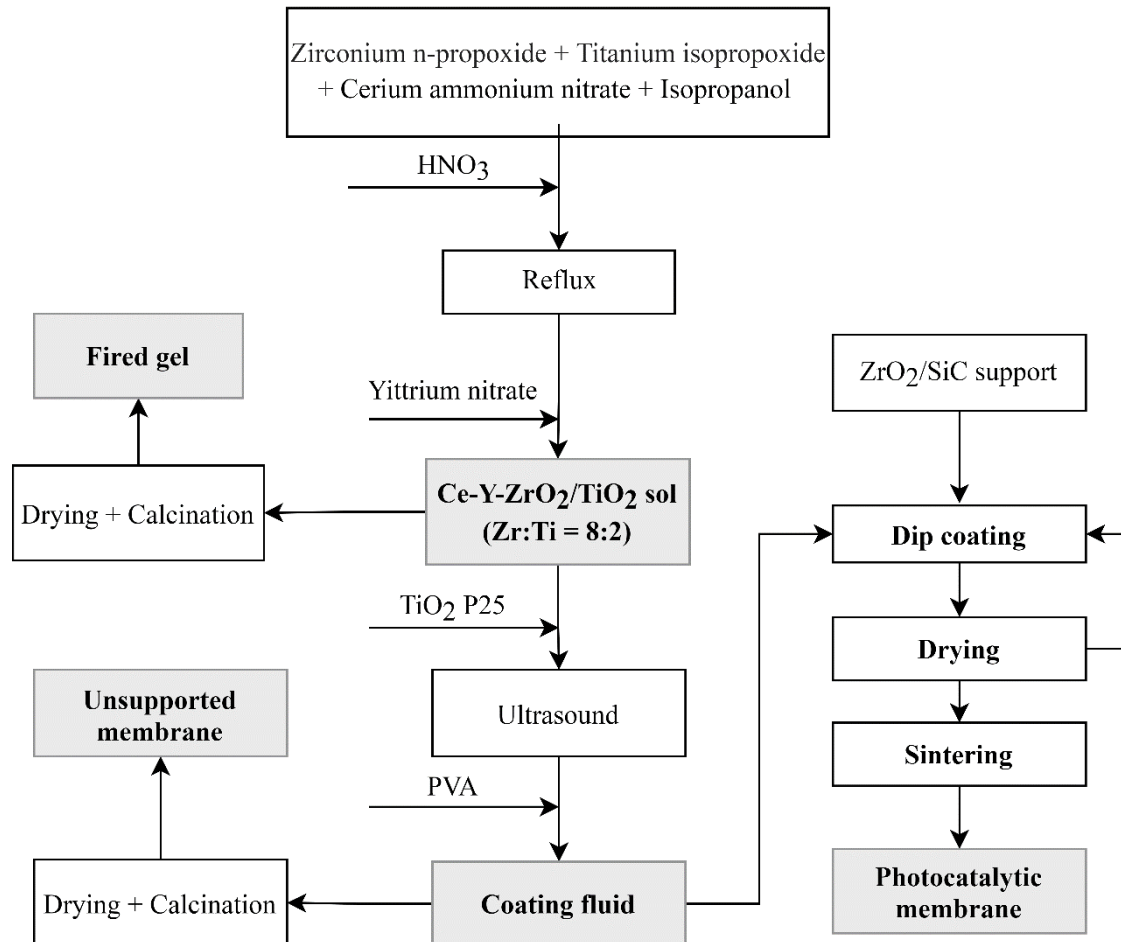


Fig. A3.1. Experimental design for preparation of Zr/Ti sols, fired gel, coating fluid, unsupported membrane, and photocatalytic membrane.

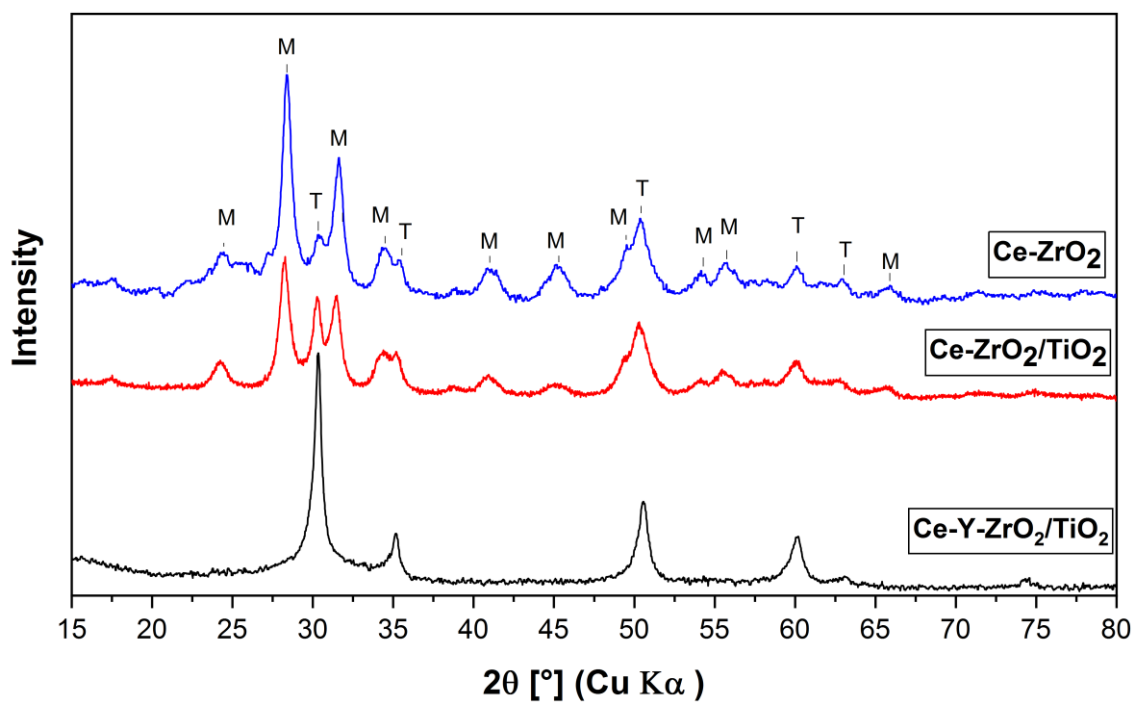


Fig. A3.2. XRD patens of the different zirconia gels calcined at temperature T.

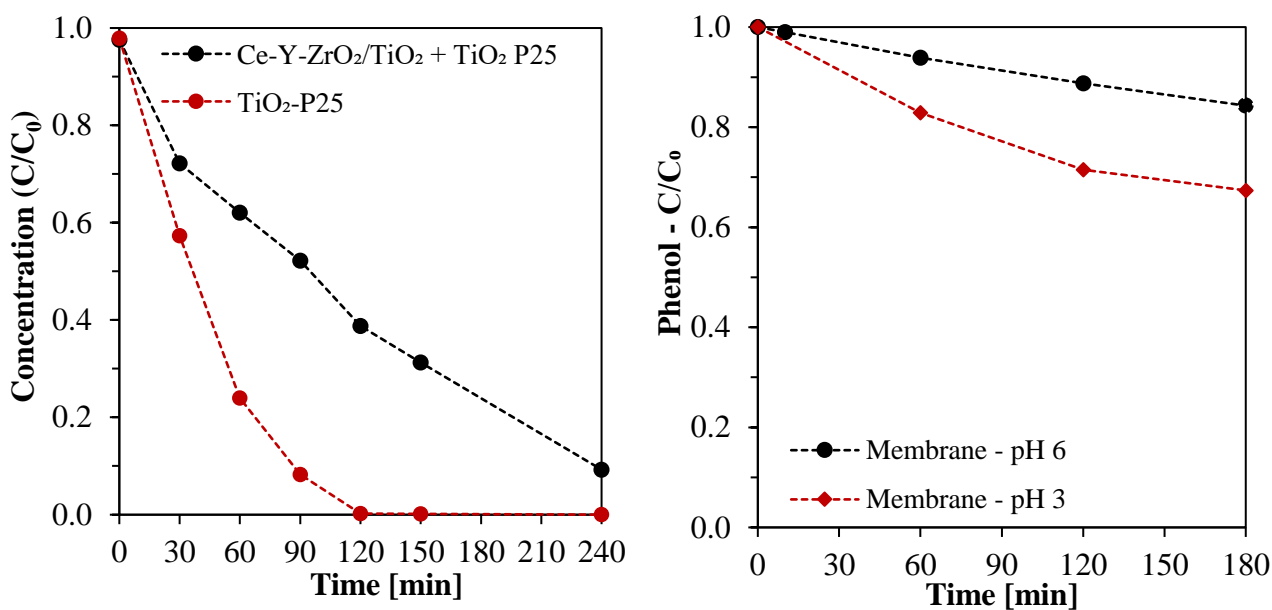


Fig. A3.3. (a) Photodegradation of phenol using as catalyst (1 mg mL^{-1}) the unsupported membrane and AEROXIDE TiO_2 P25 particles. (b) Photodegradation of phenol using the photocatalytic membrane, initial phenol concentration $C_0 = 10 \text{ mg L}^{-1}$.

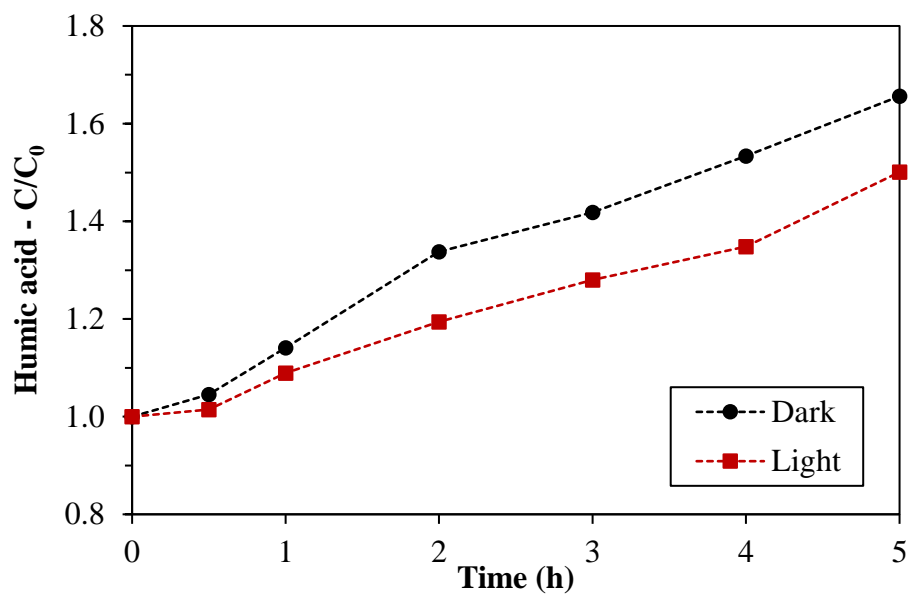


Fig. A3.4. Concentration of humic acid in the retentates obtained in the filtration of humic acid with the photocatalytic membrane in dark and under light irradiation.

5. CONCLUSIONS

The photocatalyst studied in this thesis, cerium-doped zirconia (Ce-ZrO_2), was successfully synthesised by hydrothermal and sol-gel processes. The obtained nanoparticles were fully characterized in terms of phase composition (XRD), porosity and surface area (N_2 absorption/desorption), surface charge (zeta potential), and HA adsorption isotherms. In the photodegradation of HA catalyzed by Ce-ZrO_2 water dispersions, it was observed that the sol-gel prepared Ce-ZrO_2 exhibited the higher HA removal in circumneutral pH, achieving 93% of efficiency in 180 min of adsorption in the dark followed by 180 min under visible-light irradiation using light-emitting diodes (LEDs). Changes in spectral properties and in total organic carbon amounts confirmed the HA degradation and contributed to the proposal of a mechanism for the HA photodegradation.

Ce-ZrO_2 catalyst was immobilized through a sol-gel process on a silicon carbide (SiC) support, to increase the efficiency and avoid using suspended nanoparticles. It was verified that the system was efficient in the photocatalytic reduction of Cr(VI), one of the most dangerous pollutants because of its carcinogenicity and high-toxicity. The influence of initial pH, humic acid (HA), and catalyst dosage was investigated for Cr(VI) containing solutions. Then, a real galvanizing industry effluent ($\text{Cr(VI)}=77\text{mg.L}^{-1}$, $\text{Zn}=1789\text{mg.L}^{-1}$) was treated. It was observed that Cr(VI) adsorption and photoreduction are greatly favoured at low pH values. HA can decrease Cr(VI) adsorption but also acts as holes scavenger, reducing the electron-hole recombination, consequently favouring the photoreduction. With the immobilized Ce-ZrO_2 , more than 97% of Cr(VI) was removed from the diluted effluent. These results indicate that the immobilized catalyst, upon more investigations, could have a potential application of in the treatment of Cr(VI) effluents even in the presence of other metals and natural organic matter.

In the effort to develop the photocatalytic membrane, an ultrafiltration intermediate layer, made of pure zirconia, was fabricated by dip coating the high porous SiC support with a ZrO_2 slurry prepared by ceramic processing. The optimum slurry was obtained with the aid of 2 %wt of the dispersant Dolapix CE64 followed by ball milling for 24 h and addition of 2 %wt of the binder Optapix CS 76. The green membranes were sintered in a temperature range between 1000-1300 °C, in air. With two dip coating-drying cycles and sintering at the optimal temperature, it was obtained a mechanically strong, homogenous, and defect free separation layer with 45 μm of thickness and average pore size of 60 nm. A pure water permeability of $360\text{ L m}^{-2}\text{ h}^{-1}\text{ bar}^{-1}$ and high retentions of humic acid, indigo dye, and hemoglobin were observed, which indicated the possibility to use this membrane in treating wastewater containing organic matter, from tanning and food industries. Owing to the membrane high hydrophilicity, in a pilot test with an olive

oil/water emulsion, 99.91 % of the oil was removed without fouling. Long-term corrosion tests (21 weeks) in basic and acid baths indicated no damages (no change in the pore size) during time. The developed ZrO₂/SiC membrane has the properties required to operate in harsh conditions (*e.g.* heavily contaminated industrial effluents or urban and tanning wastewaters) or in applications that require severe membrane cleaning and disinfection, such as food and pharmaceutical industries.

A photocatalytic Ce-Y-ZrO₂/TiO₂ ultrafiltration membrane was successfully prepared on the ZrO₂/SiC support using a modified sol-gel process. The 2 μm thick top active layer was uniform and defect-free, being composed of tetragonal zirconia, anatase and rutile titania. The membrane presented a molecular weight cut-off (MWCO) of 19 kDa, equivalent to an average pore size of 6 nm, and a high pure water permeability, 160 L m⁻² h⁻¹ bar⁻¹. The high hydrophilicity and negative surface charge of the membrane favoured a great retention of proteins (bovine serum albumin, whey protein, and hemoglobin), indigo dye, and humic acid. In photocatalytic experiments, the developed membrane was able to degrade phenol and humic acid under simulated sun light irradiation. In humic acid filtration tests, the membrane presented better anti-fouling properties (smaller flux decline) and higher permeate flux under irradiation compared to the filtration in the dark, as a result of the HA photodegradation and the light-induced superhydrophilicity of the TiO₂ top layer. Moreover, self-cleaning properties were observed, as the membrane recovered up to 97% of the original flux by irradiation. Consequently, it can operate for long time without chemical cleaning, which could reduce operational costs and the process footprint.

In conclusion, the results obtained indicate that the developed membranes have the potential to be further applied in innovative treatments for drinking and wastewaters by combining filtration and advanced oxidation processes in the abatement of contaminants of emerging concern in the presence of natural organic matter. Furthermore, solar light could be used to drive the process, which contributes to the development of more sustainable, cleaner, and cost-effective wastewater treatments, with important environmental implications.

6. REFERENCES

- [1] Z. He, Z. Lyu, Q. Gu, L. Zhang, J. Wang, Ceramic-based membranes for water and wastewater treatment, *Colloids Surfaces A Physicochem. Eng. Asp.* 578 (2019) 123513. <https://doi.org/10.1016/j.colsurfa.2019.05.074>.
- [2] M.A. Shannon, P.W. Bohn, M. Elimelech, J.G. Georgiadis, B.J. Marin, A.M. Mayes, Science and technology for water purification in the coming decades, 452 (2008) 301–310. <https://doi.org/10.1038/nature06599>.
- [3] M. Campinas, R.M.C. Viegas, R. Coelho, H. Lucas, M.J. Rosa, Adsorption/Coagulation/Ceramic Microfiltration for Treating Challenging Waters for Drinking Water Production, *Membr.* 11 (2021). <https://doi.org/10.3390/membranes11020091>.
- [4] T. Nawaz, S. Sengupta, Contaminants of Emerging Concern: Occurrence, Fate, and Remediation, in: *Adv. Water Purif. Tech.*, Elsevier, 2019: pp. 67–114. <https://doi.org/10.1016/B978-0-12-814790-0.00004-1>.
- [5] S. Kim, K.H. Chu, Y.A.J. Al-Hamadani, C.M. Park, M. Jang, D.-H. Kim, M. Yu, J. Heo, Y. Yoon, Removal of contaminants of emerging concern by membranes in water and wastewater: A review, *Chem. Eng. J.* (2017). <https://doi.org/10.1016/j.cej.2017.11.044>.
- [6] J. Hou, G. Dong, Y. Ye, V. Chen, Enzymatic degradation of bisphenol-A with immobilized laccase on TiO₂ sol-gel coated PVDF membrane, *J. Memb. Sci.* 469 (2014) 19–30. <https://doi.org/10.1016/j.memsci.2014.06.027>.
- [7] A.S. Mestre, A.P. Carvalho, Photocatalytic Degradation of Pharmaceuticals Carbamazepine, Diclofenac, and Sulfamethoxazole by Semiconductor and Carbon Materials: A Review, *Molecules.* 24 (2019) 3702. <https://doi.org/10.3390/molecules24203702>.
- [8] X. Zhang, L. Fan, F.A. Roddick, Effect of feedwater pre-treatment using UV/H₂O₂ for mitigating the fouling of a ceramic MF membrane caused by soluble algal organic matter, *J. Memb. Sci.* 493 (2015) 683–689. <https://doi.org/10.1016/j.memsci.2015.07.024>.
- [9] E.A. Serna-Galvis, A.M. Botero-Coy, D. Martínez-Pachón, A. Moncayo-Lasso, M. Ibáñez, F. Hernández, R.A. Torres-Palma, Degradation of seventeen contaminants of emerging concern in municipal wastewater effluents by sonochemical advanced oxidation processes, *Water Res.* 154 (2019) 349–360. <https://doi.org/10.1016/j.watres.2019.01.045>.
- [10] S. Leong, A. Razmjou, K. Wang, K. Hapgood, X. Zhang, H. Wang, TiO₂based photocatalytic membranes: A review, *J. Memb. Sci.* 472 (2014) 167–184. <https://doi.org/10.1016/j.memsci.2014.08.016>.
- [11] A. Al Mayyahi, H.A.A. Al-asadi, Advanced Oxidation Processes (AOPs) for Wastewater Treatment and Reuse : A Brief Review, 2 (2018) 18–30.
- [12] S. Li, C. Wei, P. Wang, P. Gao, L. Zhou, G. Wen, Zirconia ultrafiltration membranes on silicon carbide substrate: microstructure and water flux, *J. Eur. Ceram. Soc.* 40 (2020) 4290–4298. <https://doi.org/10.1016/j.jeurceramsoc.2020.04.020>.
- [13] Q. Jiang, J. Zhou, Y. Miao, S. Yang, M. Zhou, Z. Zhong, W. Xing, Lower-temperature preparation of SiC ceramic membrane using zeolite residue as sintering aid for oil-in-water separation, *J. Memb. Sci.* 610 (2020) 118238. <https://doi.org/10.1016/j.memsci.2020.118238>.
- [14] D.H. Kim, B.H. Lee, Pilot Study Analysis of Three Different Processes in Drinking Water Treatment, 16 (2011) 237–242. <https://doi.org/10.1109/ITA.2014.6804231>.
- [15] H.C. Duong, M. Duke, S. Gray, P. Cooper, L.D. Nghiem, Membrane scaling and prevention techniques during seawater desalination by air gap membrane distillation, *Desalination.* 397 (2016) 92–100.

- <https://doi.org/10.1016/j.desal.2016.06.025>.
- [16] H. Qin, W. Guo, X. Huang, P. Gao, H. Xiao, Preparation of yttria-stabilized ZrO₂ nanofiltration membrane by reverse micelles-mediated sol-gel process and its application in pesticide wastewater treatment, *J. Eur. Ceram. Soc.* 40 (2020) 145–154. <https://doi.org/10.1016/j.jeurceramsoc.2019.09.023>.
- [17] Y. Feng, K. Wang, C. Davies, H. Wang, Carbon Nanotube/Alumina/Polyethersulfone Hybrid Hollow Fiber Membranes with Enhanced Mechanical and Anti-Fouling Properties, *Nanomaterials*. 5 (2015) 1366–1378. <https://doi.org/10.3390/nano5031366>.
- [18] D. da Silva Biron, V. dos Santos, M. Zeni, *Ceramic Membranes Applied in Separation Processes*, 2018. <https://doi.org/10.1007/978-3-319-58604-5>.
- [19] A. Kayvani Fard, G. McKay, A. Buekenhoudt, H. Al Sulaiti, F. Motmans, M. Khraisheh, M. Atieh, *Inorganic Membranes: Preparation and Application for Water Treatment and Desalination*, *Materials (Basel)*. 11 (2018) 74. <https://doi.org/10.3390/ma11010074>.
- [20] A. Boulkrinat, F. Bouzerara, A. Harabi, K. Harrouche, S. Stelitano, F. Russo, F. Galiano, A. Figoli, Synthesis and characterization of ultrafiltration ceramic membranes used in the separation of macromolecular proteins, *J. Eur. Ceram. Soc.* (2020). <https://doi.org/10.1016/j.jeurceramsoc.2020.06.060>.
- [21] Y. Zhu, D. Wang, L. Jiang, J. Jin, Recent progress in developing advanced membranes for emulsified oil/water separation, *NPG Asia Mater.* 6 (2014) e101–e101. <https://doi.org/10.1038/am.2014.23>.
- [22] B. Hofs, J. Ogier, D. Vries, E.F. Beerendonk, E.R. Cornelissen, Comparison of ceramic and polymeric membrane permeability and fouling using surface water, *Sep. Purif. Technol.* 79 (2011) 365–374. <https://doi.org/10.1016/j.seppur.2011.03.025>.
- [23] M. Padaki, R. Surya Murali, M.S. Abdullah, N. Misdan, A. Moslehyani, M.A. Kassim, N. Hilal, A.F. Ismail, Membrane technology enhancement in oil–water separation. A review, *Desalination*. 357 (2015) 197–207. <https://doi.org/10.1016/j.desal.2014.11.023>.
- [24] T. Tsuru, *Inorganic Porous Membranes For Liquid Phase Separation*, *Sep. Purif. Methods*. 30 (2001) 191–220. <https://doi.org/10.1081/SPM-100108159>.
- [25] M.M. Pendergast, E.M.V. Hoek, A review of water treatment membrane nanotechnologies, *Energy Environ. Sci.* 4 (2011) 1946. <https://doi.org/10.1039/c0ee00541j>.
- [26] X. Zhang, T. Zhang, J. Ng, D.D. Sun, High-Performance Multifunctional TiO₂ Nanowire Ultrafiltration Membrane with a Hierarchical Layer Structure for Water Treatment, *Adv. Funct. Mater.* 19 (2009) 3731–3736. <https://doi.org/10.1002/adfm.200901435>.
- [27] C. Li, W. Sun, Z. Lu, X. Ao, S. Li, Ceramic nanocomposite membranes and membrane fouling: A review, *Water Res.* 175 (2020) 115674. <https://doi.org/10.1016/j.watres.2020.115674>.
- [28] Y. Lu, T. Chen, X. Chen, M. Qiu, Y. Fan, Fabrication of TiO₂-doped ZrO₂ nanofiltration membranes by using a modified colloidal sol-gel process and its application in simulative radioactive effluent, *J. Memb. Sci.* 514 (2016) 476–486. <https://doi.org/10.1016/j.memsci.2016.04.074>.
- [29] S. Benfer, P. Árki, G. Tomandl, *Ceramic Membranes for Filtration Applications— Preparation and Characterization*, *Adv. Eng. Mater.* 6 (2004) 495–500. <https://doi.org/10.1002/adem.200400577>.
- [30] A. Basile, F. Gallucci, *Membranes for membrane reactors: preparation, optimization and selection*, John Wiley & Sons, 2010.
- [31] T. Van Gestel, D. Sebold, Hydrothermally stable mesoporous ZrO₂ membranes prepared by a facile nanoparticle deposition process, *Sep. Purif. Technol.* 221 (2019) 399–407. <https://doi.org/10.1016/j.seppur.2019.03.066>.

- [32] H. Verweij, Inorganic membranes, *Curr. Opin. Chem. Eng.* 1 (2012) 156–162. <https://doi.org/10.1016/j.coche.2012.03.006>.
- [33] X. Da, X. Chen, B. Sun, J. Wen, M. Qiu, Y. Fan, Preparation of zirconia nanofiltration membranes through an aqueous sol–gel process modified by glycerol for the treatment of wastewater with high salinity, *J. Memb. Sci.* 504 (2016) 29–39. <https://doi.org/10.1016/j.memsci.2015.12.068>.
- [34] T. Van Gestel, D. Sebold, H. Kruidhof, H.J.M. Bouwmeester, ZrO₂ and TiO₂ membranes for nanofiltration and pervaporation. Part 2. Development of ZrO₂ and TiO₂ topayers for pervaporation, *J. Memb. Sci.* 318 (2008) 413–421. <https://doi.org/10.1016/j.memsci.2008.03.003>.
- [35] T. Van Gestel, H. Kruidhof, D.H.A. Blank, H.J.M. Bouwmeester, ZrO₂ and TiO₂ membranes for nanofiltration and pervaporation Part 1. Preparation and characterization of a corrosion-resistant ZrO₂ nanofiltration membrane with a MWCO<300, *J. Memb. Sci.* 284 (2006) 128–136. <https://doi.org/10.1016/j.memsci.2006.07.020>.
- [36] V. Gitis, G. Rothenberg, *Ceramic membranes: new opportunities and practical applications*, John Wiley & Sons, 2016.
- [37] M.A. Rahman, M. Ha, D. Othman, A.F. Ismail, Morphological study of yttria-stabilized zirconia hollow fibre membrane prepared using phase inversion / sintering technique, 41 (2015) 12543–12553. <https://doi.org/10.1016/j.ceramint.2015.06.066>.
- [38] C. Yang, G. Zhang, N. Xu, J. Shi, Preparation and application in oil–water separation of ZrO₂/α-Al₂O₃ MF membrane, *J. Memb. Sci.* 142 (1998) 235–243. [https://doi.org/10.1016/S0376-7388\(97\)00336-0](https://doi.org/10.1016/S0376-7388(97)00336-0).
- [39] R.S. Faibish, Y. Cohen, Fouling and rejection behavior of ceramic and polymer-modified ceramic membranes for ultrafiltration of oil-in-water emulsions and microemulsions, *Colloids Surfaces A Physicochem. Eng. Asp.* 191 (2001) 27–40. [https://doi.org/10.1016/S0927-7757\(01\)00761-0](https://doi.org/10.1016/S0927-7757(01)00761-0).
- [40] S. Anisah, W. Puthai, M. Kanezashi, H. Nagasawa, T. Tsuru, Preparation, characterization, and evaluation of TiO₂-ZrO₂ nanofiltration membranes fired at different temperatures, *J. Memb. Sci.* 564 (2018) 691–699. <https://doi.org/10.1016/j.memsci.2018.07.072>.
- [41] R.R. Bhave, *Inorganic Membranes Synthesis, Characteristics and Applications*, Springer Netherlands, Dordrecht, 1991. <https://doi.org/10.1007/978-94-011-6547-1>.
- [42] L. Fei, L. Yanhuai, S. Zhongxiao, X. Kewei, M. Dayan, G. Bo, C. Hong, Grain Growth Characteristics of Hydrothermally Prepared Yttria Stabilized Zirconia Nanocrystals during Calcination, *Rare Met. Mater. Eng.* 46 (2017) 899–905. [https://doi.org/10.1016/S1875-5372\(17\)30119-4](https://doi.org/10.1016/S1875-5372(17)30119-4).
- [43] J. Fan, H. Ohya, T. Suga, H. Ohashi, K. Yamashita, S. Tsuchiya, M. Aihara, T. Takeuchi, Y. Negishi, High flux zirconia composite membrane for hydrogen separation at elevated temperature, *J. Memb. Sci.* 170 (2000) 113–125. [https://doi.org/10.1016/S0376-7388\(99\)00363-4](https://doi.org/10.1016/S0376-7388(99)00363-4).
- [44] M. Asaeda, Y. Sakou, J. Yang, K. Shimasaki, Stability and performance of porous silica–zirconia composite membranes for pervaporation of aqueous organic solutions, *J. Memb. Sci.* 209 (2002) 163–175. [https://doi.org/10.1016/S0376-7388\(02\)00327-7](https://doi.org/10.1016/S0376-7388(02)00327-7).
- [45] T. Tsuru, T. Sudoh, T. Yoshioka, M. Asaeda, Nanofiltration in non-aqueous solutions by porous silica–zirconia membranes, *J. Memb. Sci.* 185 (2001) 253–261. [https://doi.org/10.1016/S0376-7388\(00\)00651-7](https://doi.org/10.1016/S0376-7388(00)00651-7).
- [46] F. Shojai, T.A. Mäntylä, Chemical stability of yttria doped zirconia membranes in acid and basic aqueous solutions: chemical properties, effect of annealing and ageing time, *Ceram. Int.* 27 (2001) 299–307. [https://doi.org/10.1016/S0272-8842\(00\)00080-8](https://doi.org/10.1016/S0272-8842(00)00080-8).
- [47] M. Qiu, Y. Fan, N. Xu, Preparation of supported zirconia ultrafiltration membranes with the aid of polymeric

- additives, *J. Memb. Sci.* 348 (2010) 252–259. <https://doi.org/10.1016/j.memsci.2009.11.009>.
- [48] S. Dey, P. Bhattacharya, S. Bandyopadhyay, S.N. Roy, S. Majumdar, G.C. Sahoo, Single step preparation of zirconia ultrafiltration membrane over clay-alumina based multichannel ceramic support for wastewater treatment, *J. Membr. Sci. Res.* 4 (2018) 28–33. <https://doi.org/10.22079/jmsr.2017.58311.1126>.
- [49] N. Saffaj, R. Mamouni, A. Laknifli, A. Mouna, S.A. Younssi, A. Albizane, Efficiency of Ultrafiltration Ceramic Membranes for Toxic Elements Removal From Wastewaters, *Sci. Study Res. Chem. Chem. Eng.* 11 (2010) 243–254.
- [50] F. Shojai, T.A. Mäntylä, Effect of sintering temperature and holding time on the properties of 3Y-ZrO₂ microfiltration membranes, *J. Mater. Sci.* 36 (2001) 3437–3446. <https://doi.org/10.1023/A:1017908011672>.
- [51] H. Guo, S. Zhao, X. Wu, H. Qi, Fabrication and characterization of TiO₂/ZrO₂ ceramic membranes for nanofiltration, *Microporous Mesoporous Mater.* 260 (2018) 125–131. <https://doi.org/10.1016/j.micromeso.2016.03.011>.
- [52] W. Deng, X. Yu, M. Sahimi, T.T. Tsotsis, Highly permeable porous silicon carbide support tubes for the preparation of nanoporous inorganic membranes, *J. Memb. Sci.* 451 (2014) 192–204. <https://doi.org/10.1016/j.memsci.2013.09.059>.
- [53] M. Facciotti, V. Boffa, G. Magnacca, L.B. Jørgensen, P.K. Kristensen, A. Farsi, K. König, M.L. Christensen, Y. Yue, Deposition of thin ultrafiltration membranes on commercial SiC microfiltration tubes, *Ceram. Int.* 40 (2014) 3277–3285. <https://doi.org/10.1016/j.ceramint.2013.09.107>.
- [54] E. Eray, V.M. Candelario, V. Boffa, H. Safafar, D.N. Østedgaard-Munck, N. Zahrtmann, H. Kadrispahic, M.K. Jørgensen, A roadmap for the development and applications of silicon carbide membranes for liquid filtration: Recent advancements, challenges, and perspectives, *Chem. Eng. J.* 414 (2021) 128826. <https://doi.org/10.1016/j.cej.2021.128826>.
- [55] M.C. Fraga, S. Sanches, V.J. Pereira, J.G. Crespo, L. Yuan, J. Marcher, M.M. de Yuso, E. Rodríguez-Castellón, J. Benavente, Morphological, chemical surface and filtration characterization of a new silicon carbide membrane, *J. Eur. Ceram. Soc.* 37 (2017) 899–905. <https://doi.org/10.1016/j.jeurceramsoc.2016.10.007>.
- [56] B.J. Lee, Z. Zhang, S. Baek, S. Kim, D. Kim, K. Yong, Bio-inspired dewetted surfaces based on SiC/Si interlocked structures for enhanced-underwater stability and regenerative-drag reduction capability, *Sci. Rep.* 6 (2016) 24653. <https://doi.org/10.1038/srep24653>.
- [57] N. Li, X. Wang, H. Zhang, Z. Zhang, J. Ding, J. Lu, Comparing the performance of various nanofiltration membranes in advanced oxidation-nanofiltration treatment of reverse osmosis concentrates, *Environ. Sci. Pollut. Res.* 26 (2019) 17472–17481. <https://doi.org/10.1007/s11356-019-05120-2>.
- [58] M. Fraga, S. Sanches, J. Crespo, V. Pereira, Assessment of a New Silicon Carbide Tubular Honeycomb Membrane for Treatment of Olive Mill Wastewaters, *Membranes (Basel)*. 7 (2017) 12. <https://doi.org/10.3390/membranes7010012>.
- [59] R. Neufert, M. Moeller, A.K. Bakshi, Dead-End Silicon Carbide Micro-Filters for Liquid Filtration, in: 2013: pp. 113–125. <https://doi.org/10.1002/9781118807811.ch10>.
- [60] R.J. Ciora, B. Fayyaz, P.K.T. Liu, V. Suwanmethanond, R. Mallada, M. Sahimi, T.T. Tsotsis, Preparation and reactive applications of nanoporous silicon carbide membranes, *Chem. Eng. Sci.* 59 (2004) 4957–4965. <https://doi.org/10.1016/j.ces.2004.07.015>.
- [61] M. Xu, M. Guan, S. Wang, M. Wu, Preparation of Silicon Carbide hollow fiber Membrane in Low Temperature by Precursor Pyrolysis, *IOP Conf. Ser. Mater. Sci. Eng.* 768 (2020) 022061.

- <https://doi.org/10.1088/1757-899X/768/2/022061>.
- [62] H.G. Choi, M. Son, S.H. Yoon, E. Celik, S. Kang, H. Park, C.H. Park, H. Choi, Alginate fouling reduction of functionalized carbon nanotube blended cellulose acetate membrane in forward osmosis, *Chemosphere*. 136 (2015) 204–210. <https://doi.org/10.1016/j.chemosphere.2015.05.003>.
- [63] J. Wang, Z. Wang, Y. Liu, J. Wang, S. Wang, Surface modification of NF membrane with zwitterionic polymer to improve anti-biofouling property, *J. Memb. Sci.* 514 (2016) 407–417. <https://doi.org/10.1016/j.memsci.2016.05.014>.
- [64] G. Mustafa, K. Wyns, P. Vandezande, A. Buekenhoudt, V. Meynen, Novel grafting method efficiently decreases irreversible fouling of ceramic nanofiltration membranes, *J. Memb. Sci.* 470 (2014) 369–377. <https://doi.org/10.1016/j.memsci.2014.07.050>.
- [65] A.W. Mohammad, Y.H. Teow, W.L. Ang, Y.T. Chung, D.L. Oatley-Radcliffe, N. Hilal, Nanofiltration membranes review: Recent advances and future prospects, *Desalination*. 356 (2015) 226–254. <https://doi.org/10.1016/j.desal.2014.10.043>.
- [66] W. Yuan, A.L. Zydney, Humic Acid Fouling during Ultrafiltration, *Environ. Sci. Technol.* 34 (2000) 5043–5050. <https://doi.org/10.1021/es0012366>.
- [67] A. Charfi, H. Jang, J. Kim, Membrane fouling by sodium alginate in high salinity conditions to simulate biofouling during seawater desalination, *Bioresour. Technol.* 240 (2017) 106–114. <https://doi.org/10.1016/j.biortech.2017.02.086>.
- [68] X. Li, Y. Cao, H. Yu, G. Kang, X. Jie, Z. Liu, Q. Yuan, A novel composite nanofiltration membrane prepared with PHGH and TMC by interfacial polymerization, *J. Memb. Sci.* 466 (2014) 82–91. <https://doi.org/10.1016/j.memsci.2014.04.034>.
- [69] A.W. Zularisam, A.F. Ismail, M. Sakinah, Application and Challenges of Membrane in Surface Water Treatment, *J. Appl. Sci.* 10 (2010) 380–390. <https://doi.org/10.3923/jas.2010.380.390>.
- [70] M.F.A. Goosen, S.S. Sablani, H. Al-Hinai, S. Al-Obeidani, R. Al-Belushi, D. Jackson, Fouling of Reverse Osmosis and Ultrafiltration Membranes: A Critical Review, *Sep. Sci. Technol.* 39 (2005) 2261–2297. <https://doi.org/10.1081/SS-120039343>.
- [71] S.S. Alias, Z. Harun, I.S.A. Latif, Characterization and performance of porous photocatalytic ceramic membranes coated with TiO₂ via different dip-coating routes, *J. Mater. Sci.* 53 (2018) 11534–11552. <https://doi.org/10.1007/s10853-018-2392-3>.
- [72] E.S. Kim, Q. Yu, B. Deng, Plasma surface modification of nanofiltration (NF) thin-film composite (TFC) membranes to improve anti organic fouling, *Appl. Surf. Sci.* 257 (2011) 9863–9871. <https://doi.org/10.1016/j.apsusc.2011.06.059>.
- [73] W.M. Clark, A. Bansal, M. Sontakke, Y.H. Ma, Protein adsorption and fouling in ceramic ultrafiltration membranes, *J. Memb. Sci.* 55 (1991) 21–38. [https://doi.org/10.1016/S0376-7388\(00\)82325-X](https://doi.org/10.1016/S0376-7388(00)82325-X).
- [74] B. Van der Bruggen, M. Mänttari, M. Nyström, Drawbacks of applying nanofiltration and how to avoid them: A review, *Sep. Purif. Technol.* 63 (2008) 251–263. <https://doi.org/10.1016/j.seppur.2008.05.010>.
- [75] K. Staszak, Membrane processes, *Phys. Sci. Rev.* 2 (2017) 1–18. <https://doi.org/10.1515/psr-2017-0142>.
- [76] N.F. Ishak, N.A. Hashim, M.H.D. Othman, P. Monash, F.M. Zuki, Recent progress in the hydrophilic modification of alumina membranes for protein separation and purification, *Ceram. Int.* 43 (2017) 915–925. <https://doi.org/10.1016/j.ceramint.2016.10.044>.
- [77] G. Zhang, W. Jin, N. Xu, Design and Fabrication of Ceramic Catalytic Membrane Reactors for Green Chemical Engineering Applications, *Engineering*. 4 (2018) 848–860.

- <https://doi.org/10.1016/j.eng.2017.05.001>.
- [78] A. Asatekin, S. Kang, M. Elimelech, A.M. Mayes, Anti-fouling ultrafiltration membranes containing polyacrylonitrile-graft-poly(ethylene oxide) comb copolymer additives, *J. Memb. Sci.* 298 (2007) 136–146. <https://doi.org/10.1016/j.memsci.2007.04.011>.
- [79] Y. Baek, C. Kim, D.K. Seo, T. Kim, J.S. Lee, Y.H. Kim, K.H. Ahn, S.S. Bae, S.C. Lee, J. Lim, K. Lee, J. Yoon, High performance and antifouling vertically aligned carbon nanotube membrane for water purification, *J. Memb. Sci.* 460 (2014) 171–177. <https://doi.org/10.1016/j.memsci.2014.02.042>.
- [80] A. Tiraferri, Y. Kang, E.P. Giannelis, M. Elimelech, Superhydrophilic Thin-Film Composite Forward Osmosis Membranes for Organic Fouling Control: Fouling Behavior and Antifouling Mechanisms, *Environ. Sci. Technol.* 46 (2012) 11135–11144. <https://doi.org/10.1021/es3028617>.
- [81] G. Rao, Q. Zhang, H. Zhao, J. Chen, Y. Li, Novel titanium dioxide/iron (III) oxide/graphene oxide photocatalytic membrane for enhanced humic acid removal from water, *Chem. Eng. J.* 302 (2016) 633–640. <https://doi.org/10.1016/j.cej.2016.05.095>.
- [82] R. Wang, D. Ren, S. Xia, Y. Zhang, J. Zhao, Photocatalytic degradation of Bisphenol A (BPA) using immobilized TiO₂ and UV illumination in a horizontal circulating bed photocatalytic reactor (HCBPR), *J. Hazard. Mater.* 169 (2009) 926–932. <https://doi.org/10.1016/j.jhazmat.2009.04.036>.
- [83] R. Goei, T.-T. Lim, Asymmetric TiO₂ hybrid photocatalytic ceramic membrane with porosity gradient: Effect of structure directing agent on the resulting membranes architecture and performances, *Ceram. Int.* 40 (2014) 6747–6757. <https://doi.org/10.1016/j.ceramint.2013.11.137>.
- [84] R. Goei, T.T. Lim, Ag-decorated TiO₂ photocatalytic membrane with hierarchical architecture: Photocatalytic and anti-bacterial activities, *Water Res.* 59 (2014) 207–218. <https://doi.org/10.1016/j.watres.2014.04.025>.
- [85] J. Mendret, M. Hatat-Fraile, M. Rivallin, S. Brosillon, Hydrophilic composite membranes for simultaneous separation and photocatalytic degradation of organic pollutants, *Sep. Purif. Technol.* 111 (2013) 9–19. <https://doi.org/10.1016/j.seppur.2013.03.030>.
- [86] H. Zhang, X. Quan, S. Chen, H. Zhao, Y. Zhao, Fabrication of photocatalytic membrane and evaluation its efficiency in removal of organic pollutants from water, *Sep. Purif. Technol.* 50 (2006) 147–155. <https://doi.org/10.1016/j.seppur.2005.11.018>.
- [87] S. Sanches, C. Nunes, P.C. Passarinho, F.C. Ferreira, V.J. Pereira, J.G. Crespo, Development of photocatalytic titanium dioxide membranes for degradation of recalcitrant compounds, *J. Chem. Technol. Biotechnol.* 92 (2017) 1727–1737. <https://doi.org/10.1002/jctb.5172>.
- [88] C.P. Athanasekou, N.G. Moustakas, S. Morales-Torres, L.M. Pastrana-Martínez, J.L. Figueiredo, J.L. Faria, A.M.T. Silva, J.M. Dona-Rodríguez, G.E. Romanos, P. Falaras, Ceramic photocatalytic membranes for water filtration under UV and visible light, *Appl. Catal. B Environ.* 178 (2015) 12–19. <https://doi.org/10.1016/j.apcatb.2014.11.021>.
- [89] A. Taavoni-Gilan, E. Taheri-Nassaj, M. Shamsipur, Synthesis of nanostructured titania/zirconia membrane and investigation of its physical separation and photocatalytic properties in treatment of textile industries wastewater, *J. Iran. Chem. Soc.* 15 (2018) 2759–2769. <https://doi.org/10.1007/s13738-018-1463-3>.
- [90] K.A. Manjumol, S. Sankar, B.N. Nair, M. Midhun, P.A. Mohamed, K.G.K. Warriar, A novel approach to formulate high flux multifunctional ultrafiltration membranes from photocatalytic titania composite precursors on multi-channel tubular substrates, *RSC Adv.* 6 (2016) 58813–58822. <https://doi.org/10.1039/c6ra14117j>.
- [91] H. Zhang, X. Quan, S. Chen, H. Zhao, Fabrication and characterization of silica/titania nanotubes composite

- membrane with photocatalytic capability, *Environ. Sci. Technol.* 40 (2006) 6104–6109. <https://doi.org/10.1021/es060092d>.
- [92] A.A. Habibpanah, S. Pourhashem, H. Sarpoolaky, Preparation and characterization of photocatalytic titania–alumina composite membranes by sol–gel methods, *J. Eur. Ceram. Soc.* 31 (2011) 2867–2875. <https://doi.org/10.1016/j.jeurceramsoc.2011.06.014>.
- [93] E. Bet-moushoul, Y. Mansourpanah, K. Farhadi, M. Tabatabaei, TiO₂ nanocomposite based polymeric membranes: A review on performance improvement for various applications in chemical engineering processes, *Chem. Eng. J.* 283 (2016) 29–46. <https://doi.org/10.1016/j.cej.2015.06.124>.
- [94] U. Aust, S. Benfer, M. Dietze, A. Rost, G. Tomandl, Development of microporous ceramic membranes in the system TiO₂/ZrO₂, *J. Memb. Sci.* 281 (2006) 463–471. <https://doi.org/10.1016/j.memsci.2006.04.016>.
- [95] T. Fukumoto, T. Yoshioka, H. Nagasawa, M. Kanezashi, T. Tsuru, Development and gas permeation properties of microporous amorphous TiO₂–ZrO₂–organic composite membranes using chelating ligands, *J. Memb. Sci.* 461 (2014) 96–105. <https://doi.org/10.1016/j.memsci.2014.02.031>.
- [96] G.N. Shao, S.M. Imran, S.J. Jeon, M. Engole, N. Abbas, M. Salman Haider, S.J. Kang, H.T. Kim, Sol–gel synthesis of photoactive zirconia–titania from metal salts and investigation of their photocatalytic properties in the photodegradation of methylene blue, *Powder Technol.* 258 (2014) 99–109. <https://doi.org/10.1016/j.powtec.2014.03.024>.
- [97] Q. Xu, M.A. Anderson, Sol-Gel Route to Synthesis of Microporous Ceramic Membranes: Thermal Stability of TiO₂-ZrO₂Mixed Oxides, *J. Am. Ceram. Soc.* 76 (1993) 2093–2097. <https://doi.org/10.1111/j.1151-2916.1993.tb08338.x>.
- [98] M. Takeuchi, H. Yamashita, M. Matsuoka, M. Anpo, T. Hirao, N. Itoh, N. Iwamoto, Photocatalytic decomposition of NO under visible light irradiation on the Cr-ion-implanted TiO₂ thin film photocatalyst, *Catal. Letters.* 67 (2000) 135–137. <https://doi.org/10.1023/A:1019065521567>.
- [99] R. Asahi, Visible-Light Photocatalysis in Nitrogen-Doped Titanium Oxides, *Science* (80-.). 293 (2001) 269–271. <https://doi.org/10.1126/science.1061051>.
- [100] S.C. Warren, E. Thimsen, Plasmonic solar water splitting, *Energy Environ. Sci.* 5 (2012) 5133–5146. <https://doi.org/10.1039/C1EE02875H>.
- [101] K. Maeda, K. Domen, Photocatalytic Water Splitting: Recent Progress and Future Challenges, *J. Phys. Chem. Lett.* 1 (2010) 2655–2661. <https://doi.org/10.1021/jz1007966>.
- [102] C. Gionco, M.C. Paganini, E. Giamello, O. Sacco, V. Vaiano, D. Sannino, Rare earth oxides in zirconium dioxide: How to turn a wide band gap metal oxide into a visible light active photocatalyst, *J. Energy Chem.* 26 (2017) 270–276. <https://doi.org/10.1016/j.jechem.2016.07.006>.
- [103] C. Gionco, A. Battiato, E. Vittone, M.C. Paganini, E. Giamello, Structural and spectroscopic properties of high temperature prepared ZrO₂-TiO₂mixed oxides, *J. Solid State Chem.* 201 (2013) 222–228. <https://doi.org/10.1016/j.jssc.2013.02.040>.
- [104] Q. Yuan, Y. Liu, L.-L. Li, Z.-X. Li, C.-J. Fang, W.-T. Duan, X.-G. Li, C.-H. Yan, Highly ordered mesoporous titania–zirconia photocatalyst for applications in degradation of rhodamine-B and hydrogen evolution, *Microporous Mesoporous Mater.* 124 (2009) 169–178. <https://doi.org/10.1016/j.micromeso.2009.05.006>.
- [105] S.N. Basahel, T.T. Ali, M. Mokhtar, K. Narasimharao, Influence of crystal structure of nanosized ZrO₂ on photocatalytic degradation of methyl orange, *Nanoscale Res. Lett.* 10 (2015) 73. <https://doi.org/10.1186/s11671-015-0780-z>.
- [106] M. Aflaki, F. Davar, Synthesis, luminescence and photocatalyst properties of zirconia nanosheets by modified

- Pechini method, *J. Mol. Liq.* 221 (2016) 1071–1079. <https://doi.org/10.1016/j.molliq.2016.06.067>.
- [107] V.R. Reddy, D.W. Hwang, J.S. Lee, Photocatalytic water splitting over ZrO₂ prepared by precipitation method, *Korean J. Chem. Eng.* 20 (2003) 1026–1029. <https://doi.org/10.1007/BF02706932>.
- [108] C. Gionco, M.C. Paganini, E. Giamello, R. Burgess, C. Di Valentin, G. Pacchioni, Cerium-doped zirconium dioxide, a visible-light-sensitive photoactive material of third generation, *J. Phys. Chem. Lett.* 5 (2014) 447–451. <https://doi.org/10.1021/jz402731s>.
- [109] M.C. Paganini, C. Gionco, E. Giamello, O. Sacco, V. Vaiano, D. Sannino, New Photoactive Materials Based on Zirconium Dioxide Doped with Rare Earth Metal Ions, *Adv. Sci. Lett.* 23 (2017) 5906–5908. <https://doi.org/10.1166/asl.2017.9065>.
- [110] F. Bortot Coelho, C. Gionco, M. Paganini, P. Calza, G. Magnacca, Control of Membrane Fouling in Organics Filtration Using Ce-Doped Zirconia and Visible Light, *Nanomaterials.* 9 (2019) 534. <https://doi.org/10.3390/nano9040534>.
- [111] X. Qu, P.J.J. Alvarez, Q. Li, Applications of nanotechnology in water and wastewater treatment, *Water Res.* 47 (2013) 3931–3946. <https://doi.org/10.1016/j.watres.2012.09.058>.
- [112] D. Friedmann, C. Mendive, D. Bahnemann, TiO₂ for water treatment: Parameters affecting the kinetics and mechanisms of photocatalysis, *Appl. Catal. B Environ.* 99 (2010) 398–406. <https://doi.org/10.1016/j.apcatb.2010.05.014>.
- [113] X. Wang, Z. Wu, Y. Wang, W. Wang, X. Wang, Y. Bu, J. Zhao, Adsorption-photodegradation of humic acid in water by using ZnO coupled TiO₂/bamboo charcoal under visible light irradiation, *J. Hazard. Mater.* 262 (2013) 16–24. <https://doi.org/10.1016/j.jhazmat.2013.08.037>.
- [114] V. Oskoei, M.H. Dehghani, S. Nazmara, B. Heibati, M. Asif, I. Tyagi, S. Agarwal, V.K. Gupta, Removal of humic acid from aqueous solution using UV/ZnO nano-photocatalysis and adsorption, *J. Mol. Liq.* 213 (2016) 374–380. <https://doi.org/10.1016/j.molliq.2015.07.052>.
- [115] G. Wang, Destruction of humic acid in water by UV light catalyzed oxidation with hydrogen peroxide, *Water Res.* 34 (2000) 3882–3887. [https://doi.org/10.1016/S0043-1354\(00\)00120-2](https://doi.org/10.1016/S0043-1354(00)00120-2).
- [116] N.C. Birben, C.S. Uyguner-Demirel, S. Sen Kavurmaci, Y.Y. Gürkan, N. Turkten, Z. Cinar, M. Bekbolet, Application of Fe-doped TiO₂ specimens for the solar photocatalytic degradation of humic acid, *Catal. Today.* 281 (2017) 78–84. <https://doi.org/10.1016/j.cattod.2016.06.020>.
- [117] I.N. Najm, N.L. Patania, J.G. Jacangelo, S.W. Krasner, Evaluating surrogates for disinfection by-products, *J. Am. Water Works Assoc.* 86 (1994) 98–106. <https://doi.org/10.1002/j.1551-8833.1994.tb06213.x>.
- [118] C.S. Uyguner, M. Bekbolet, Evaluation of humic acid photocatalytic degradation by UV-vis and fluorescence spectroscopy, *Catal. Today.* 101 (2005) 267–274. <https://doi.org/10.1016/j.cattod.2005.03.011>.
- [119] E. García-López, G. Marci, F.R. Pomilla, M.C. Paganini, C. Gionco, E. Giamello, L. Palmisano, ZrO₂ Based materials as photocatalysts for 2-propanol oxidation by using UV and solar light irradiation and tests for CO₂ reduction, *Catal. Today.* 313 (2018) 100–105. <https://doi.org/10.1016/j.cattod.2018.01.030>.
- [120] S. Hernández, C. Gionco, T. Husak, M. Castellino, J.A. Muñoz-Tabares, K.R. Tolod, E. Giamello, M.C. Paganini, N. Russo, Insights Into the Sunlight-Driven Water Oxidation by Ce and Er-Doped ZrO₂, *Front. Chem.* 6 (2018). <https://doi.org/10.3389/fchem.2018.00368>.
- [121] K.S.W. Sing, Reporting physisorption data for gas/solid systems with special reference to the determination of surface area and porosity (Provisional), *Pure Appl. Chem.* 54 (1982) 2201–2218. <https://doi.org/10.1351/pac198254112201>.
- [122] D. Wang, L. Guo, Y. Zhen, L. Yue, G. Xue, F. Fu, AgBr quantum dots decorated mesoporous Bi₂WO₆

- architectures with enhanced photocatalytic activities for methylene blue, *J. Mater. Chem. A.* 2 (2014) 11716–11727. <https://doi.org/10.1039/C4TA01444H>.
- [123] Y. Nosaka, A.Y. Nosaka, Generation and Detection of Reactive Oxygen Species in Photocatalysis, *Chem. Rev.* 117 (2017) 11302–11336. <https://doi.org/10.1021/acs.chemrev.7b00161>.
- [124] H. Ranjan Sahu, G. Ranga Rao, Characterization of combustion synthesized zirconia powder by UV-vis, IR and other techniques, *Bull. Mater. Sci.* 23 (2000) 349–354. <https://doi.org/10.1007/BF02708383>.
- [125] C. Gionco, M.C. Paganini, E. Giamello, R. Burgess, C. Di Valentin, G. Pacchioni, Paramagnetic Defects in Polycrystalline Zirconia: An EPR and DFT Study, *Chem. Mater.* 25 (2013) 2243–2253. <https://doi.org/10.1021/cm400728j>.
- [126] D.D. Sun, P.F. Lee, TiO₂ microsphere for the removal of humic acid from water: Complex surface adsorption mechanisms, *Sep. Purif. Technol.* 91 (2012) 30–37. <https://doi.org/10.1016/j.seppur.2011.08.035>.
- [127] S. Liu, M. Lim, R. Amal, TiO₂-coated natural zeolite: Rapid humic acid adsorption and effective photocatalytic regeneration, *Chem. Eng. Sci.* 105 (2014) 46–52. <https://doi.org/10.1016/j.ces.2013.10.041>.
- [128] K.M. Spark, J.D. Wells, B.B. Johnson, The interaction of a humic acid with heavy metals, *Aust. J. Soil Res.* 35 (1997) 89. <https://doi.org/10.1071/S96008>.
- [129] H. Kipton, J. Powell, R.M. Town, Solubility and fractionation of humic acid; effect of pH and ionic medium, *Anal. Chim. Acta.* 267 (1992) 47–54. [https://doi.org/10.1016/0003-2670\(92\)85005-Q](https://doi.org/10.1016/0003-2670(92)85005-Q).
- [130] M.A. Ferro-García, J. Rivera-Utrilla, I. Bautista-Toledo, C. Moreno-Castilla, Adsorption of Humic Substances on Activated Carbon from Aqueous Solutions and Their Effect on the Removal of Cr(III) Ions, *Langmuir.* 14 (1998) 1880–1886. <https://doi.org/10.1021/la970565h>.
- [131] G. Moussavi, S. Talebi, M. Farrokhi, R.M. Sabouti, The investigation of mechanism, kinetic and isotherm of ammonia and humic acid co-adsorption onto natural zeolite, *Chem. Eng. J.* 171 (2011) 1159–1169. <https://doi.org/10.1016/j.cej.2011.05.016>.
- [132] E. Coppola, P. Iovino, S. Salvestrini, S. Capasso, C. Colella, Humic acid sorption properties of calcium-rich derivatives of Neapolitan Yellow Tuff, *WIT Trans. Ecol. Environ.* 111 (2008) 565–574. <https://doi.org/10.2495/WP080561>.
- [133] Y.W. Wang, P.H. Yuan, C.M. Fan, Y. Wang, G.Y. Ding, Y.F. Wang, Preparation of zinc titanate nanoparticles and their photocatalytic behaviors in the photodegradation of humic acid in water, *Ceram. Int.* 38 (2012) 4173–4180. <https://doi.org/10.1016/j.ceramint.2012.01.078>.
- [134] G.E. Fryxell, G. Cao, *Environmental Applications of Nanomaterials*, Imperial College Press, 2012. <https://doi.org/10.1142/p814>.
- [135] X.Z. Li, C.M. Fan, Y.P. Sun, Enhancement of photocatalytic oxidation of humic acid in TiO₂ suspensions by increasing cation strength., *Chemosphere.* 48 (2002) 453–60. [https://doi.org/10.1016/S0045-6535\(02\)00135-2](https://doi.org/10.1016/S0045-6535(02)00135-2).
- [136] G. Xue, H. Liu, Q. Chen, C. Hills, M. Tyrer, F. Innocent, Synergy between surface adsorption and photocatalysis during degradation of humic acid on TiO₂/activated carbon composites, *J. Hazard. Mater.* 186 (2011) 765–772. <https://doi.org/10.1016/j.jhazmat.2010.11.063>.
- [137] D.P. Subagio, M. Srinivasan, M. Lim, T.T. Lim, Photocatalytic degradation of bisphenol-A by nitrogen-doped TiO₂ hollow sphere in a vis-LED photoreactor, *Appl. Catal. B Environ.* 95 (2010) 414–422. <https://doi.org/10.1016/j.apcatb.2010.01.021>.
- [138] S. Chakrabarti, B.K. Dutta, Photocatalytic degradation of model textile dyes in wastewater using ZnO as semiconductor catalyst, *J. Hazard. Mater.* 112 (2004) 269–278.

- <https://doi.org/10.1016/j.jhazmat.2004.05.013>.
- [139] V. V. Gulians, M.A. Carreon, Y.S. Lin, Ordered mesoporous and macroporous inorganic films and membranes, *J. Memb. Sci.* 235 (2004) 53–72. <https://doi.org/10.1016/j.memsci.2004.01.019>.
- [140] H. Yan, L.Y. Chai, B. Peng, M. Li, N. Peng, D.K. Hou, A novel method to recover zinc and iron from zinc leaching residue, *Miner. Eng.* 55 (2014) 103–110. <https://doi.org/10.1016/j.mineng.2013.09.015>.
- [141] R.G. Juez, V. Boffa, D.H.A. Blank, J.E. ten Elshof, Preparation of self-supporting mesostructured silica thin film membranes as gateable interconnects for microfluidics, *J. Memb. Sci.* 323 (2008) 347–351. <https://doi.org/10.1016/j.memsci.2008.06.043>.
- [142] R. Nisticò, D. Scalarone, G. Magnacca, Sol-gel chemistry, templating and spin-coating deposition: A combined approach to control in a simple way the porosity of inorganic thin films/coatings, *Microporous Mesoporous Mater.* 248 (2017) 18–29. <https://doi.org/10.1016/j.micromeso.2017.04.017>.
- [143] B. Neppolian, H.C. Choi, S. Sakthivel, B. Arabindoo, V. Murugesan, Solar light induced and TiO₂ assisted degradation of textile dye reactive blue 4, *Chemosphere.* 46 (2002) 1173–1181. [https://doi.org/10.1016/S0045-6535\(01\)00284-3](https://doi.org/10.1016/S0045-6535(01)00284-3).
- [144] A. Rodrigues, A. Brito, P. Janknecht, M.F. Proença, R. Nogueira, Quantification of humic acids in surface water: effects of divalent cations, pH, and filtration, *J. Environ. Monit.* 11 (2009) 377–382. <https://doi.org/10.1039/B811942B>.
- [145] M. Miyauchi, A. Nakajima, T. Watanabe, K. Hashimoto, Photocatalysis and Photoinduced Hydrophilicity of Various Metal Oxide Thin Films, *Chem. Mater.* 14 (2002) 2812–2816. <https://doi.org/10.1021/cm020076p>.
- [146] N. Kashif, F. Ouyang, Parameters effect on heterogeneous photocatalysed degradation of phenol in aqueous dispersion of TiO₂, *J. Environ. Sci.* 21 (2009) 527–533. [https://doi.org/10.1016/S1001-0742\(08\)62303-7](https://doi.org/10.1016/S1001-0742(08)62303-7).
- [147] Z. Guo, R. Ma, G. Li, Degradation of phenol by nanomaterial TiO₂ in wastewater, *Chem. Eng. J.* 119 (2006) 55–59. <https://doi.org/10.1016/j.cej.2006.01.017>.
- [148] N. Dehghanian, M. Ghaedi, A. Ansari, A. Ghaedi, A. Vafaei, M. Asif, S. Agarwal, I. Tyagi, V.K. Gupta, A random forest approach for predicting the removal of Congo red from aqueous solutions by adsorption onto tin sulfide nanoparticles loaded on activated carbon, *Desalin. Water Treat.* 57 (2016) 9272–9285. <https://doi.org/10.1080/19443994.2015.1027964>.
- [149] S. Khezrianjoo, H.D. Revanasiddappa, Photocatalytic Degradation of Acid Yellow 36 Using Zinc Oxide Photocatalyst in Aqueous Media, *J. Catal.* 2013 (2013) 1–6. <https://doi.org/10.1155/2013/582058>.
- [150] N. Daneshvar, M.H. Rasoulifard, A.R. Khataee, F. Hosseinzadeh, Removal of C . I . Acid Orange 7 from aqueous solution by UV irradiation in the presence of ZnO nanopowder, 143 (2007) 95–101. <https://doi.org/10.1016/j.jhazmat.2006.08.072>.
- [151] H. Chen, J. Motuzas, W. Martens, J.C. Diniz da Costa, Ceramic metal oxides with Ni²⁺ active phase for the fast degradation of Orange II dye under dark ambient, *Ceram. Int.* 44 (2018) 6634–6640. <https://doi.org/10.1016/j.ceramint.2018.01.071>.
- [152] P. Calza, C. Gionco, M. Giletta, M. Kalaboka, V.A. Sakkas, T. Albanis, M.C. Paganini, Assessment of the abatement of acelsulfame K using cerium doped ZnO as photocatalyst, *J. Hazard. Mater.* 323 (2017) 471–477. <https://doi.org/10.1016/j.jhazmat.2016.03.093>.
- [153] M. Thandu, C. Comuzzi, D. Goi, Phototreatment of Water by Organic Photosensitizers and Comparison with Inorganic Semiconductors, *Int. J. Photoenergy.* 2015 (2015) 1–22. <https://doi.org/10.1155/2015/521367>.
- [154] Z. Hua, X. Zhang, X. Bai, L. Lv, Z. Ye, X. Huang, Nitrogen-doped perovskite-type La₂Ti₂O₇ decorated on graphene composites exhibiting efficient photocatalytic activity toward bisphenol A in water, *J. Colloid*

- Interface Sci. 450 (2015) 45–53. <https://doi.org/10.1016/j.jcis.2015.02.061>.
- [155] L. Zhou, G. Zou, H. Deng, The Roles of Graphene and Ag in the Hybrid Ag@Ag₂O-Graphene for Sulfamethoxazole Degradation, *Catalysts*. 8 (2018) 272. <https://doi.org/10.3390/catal8070272>.
- [156] M.L. Tummino, E. Laurenti, F. Deganello, A. Bianco Prevot, G. Magnacca, Revisiting the catalytic activity of a doped SrFeO₃ for water pollutants removal: Effect of light and temperature, *Appl. Catal. B Environ.* 207 (2017) 174–181. <https://doi.org/10.1016/j.apcatb.2017.02.007>.
- [157] N. Serpone, A. V. Emeline, Semiconductor photocatalysis - Past, present, and future outlook, *J. Phys. Chem. Lett.* 3 (2012) 673–677. <https://doi.org/10.1021/jz300071j>.
- [158] J.K. Yang, S.M. Lee, Removal of Cr(VI) and humic acid by using TiO₂ photocatalysis, *Chemosphere*. 63 (2006) 1677–1684. <https://doi.org/10.1016/j.chemosphere.2005.10.005>.
- [159] L.B. Khalil, W.E. Mourad, M.W. Rophael, Photocatalytic reduction of environmental pollutant Cr(VI) over some semiconductors under UV/visible light illumination, *Appl. Catal. B Environ.* 17 (1998) 267–273. [https://doi.org/10.1016/S0926-3373\(98\)00020-4](https://doi.org/10.1016/S0926-3373(98)00020-4).
- [160] M. Gheju, A. Iovi, I. Balcu, Hexavalent chromium reduction with scrap iron in continuous-flow system, *J. Hazard. Mater.* 153 (2008) 655–662. <https://doi.org/10.1016/j.jhazmat.2007.09.009>.
- [161] P. Sane, S. Chaudhari, P. Nemade, S. Sontakke, Photocatalytic reduction of chromium (VI) using combustion synthesized TiO₂, *J. Environ. Chem. Eng.* 6 (2018) 68–73. <https://doi.org/10.1016/j.jece.2017.11.060>.
- [162] V.K. Gupta, A. Rastogi, Biosorption of hexavalent chromium by raw and acid-treated green alga *Oedogonium hatei* from aqueous solutions, *J. Hazard. Mater.* 163 (2009) 396–402. <https://doi.org/10.1016/j.jhazmat.2008.06.104>.
- [163] M. Costa, Potential hazards of hexavalent chromate in our drinking water, *Toxicol. Appl. Pharmacol.* 188 (2003) 1–5. [https://doi.org/10.1016/S0041-008X\(03\)00011-5](https://doi.org/10.1016/S0041-008X(03)00011-5).
- [164] P. Gikas, P. Romanos, Effects of tri-valent (Cr(III)) and hexa-valent (Cr(VI)) chromium on the growth of activated sludge, *J. Hazard. Mater.* 133 (2006) 212–217. <https://doi.org/10.1016/j.jhazmat.2005.10.023>.
- [165] G. Kassaye, N. Gabbiye, A. Alemu, Phytoremediation of chromium from tannery wastewater using local plant species, *Water Pract. Technol.* 12 (2017) 894–901. <https://doi.org/10.2166/wpt.2017.094>.
- [166] Y. Wang, D.J. Blackwood, Nanoporous MnO₂ Nanoflakes Modified Carbon Cloth Material for Efficient Removal of Heavy Metal Ions in Water by Capacitive Deionization, *Meet. Abstr. MA2018-01* (2018) 1973–1973.
- [167] A.U. Rajapaksha, M.S. Alam, N. Chen, D.S. Alessi, A.D. Igalavithana, D.C.W. Tsang, Y.S. Ok, Removal of hexavalent chromium in aqueous solutions using biochar: Chemical and spectroscopic investigations, *Sci. Total Environ.* 625 (2018) 1567–1573. <https://doi.org/10.1016/j.scitotenv.2017.12.195>.
- [168] P.M.B. Chagas, L.B. de Carvalho, A.A. Caetano, F.G.E. Nogueira, A.D. Corrêa, I. do R. Guimarães, Nanostructured oxide stabilized by chitosan: Hybrid composite as an adsorbent for the removal of chromium (VI), *J. Environ. Chem. Eng.* 6 (2018) 1008–1019. <https://doi.org/10.1016/j.jece.2018.01.026>.
- [169] A.M. Cuong, N.T. Le Na, P.N. Thang, T.N. Diep, L.B. Thuy, N.L. Thanh, N.D. Thang, Melanin-embedded materials effectively remove hexavalent chromium (Cr(VI)) from aqueous solution, *Environ. Health Prev. Med.* 23 (2018) 9. <https://doi.org/10.1186/s12199-018-0699-y>.
- [170] J.A. Navó, G. Colón, M. Trillas, J. Peral, X. Domènech, J.J. Testa, J. Padrón, D. Rodríguez, M.I. Litter, Heterogeneous photocatalytic reactions of nitrite oxidation and Cr(VI) reduction on iron-doped titania prepared by the wet impregnation method, *Appl. Catal. B Environ.* 16 (1998) 187–196. [https://doi.org/10.1016/S0926-3373\(97\)00073-8](https://doi.org/10.1016/S0926-3373(97)00073-8).

- [171] H.J. Wiegand, H. Ottenwalder, H.M. Bolt, The reduction of chromium (VI) to chromium (III) by glutathione: An intracellular redox pathway in the metabolism of the carcinogen chromate, *Toxicology*. 33 (1984) 341–348. [https://doi.org/10.1016/0300-483X\(84\)90050-7](https://doi.org/10.1016/0300-483X(84)90050-7).
- [172] Z. Zhao, H. An, J. Lin, M. Feng, V. Murugadoss, T. Ding, H. Liu, Q. Shao, X. Mai, N. Wang, H. Gu, S. Angaiah, Z. Guo, Progress on the Photocatalytic Reduction Removal of Chromium Contamination, *Chem. Rec.* 19 (2019) 873–882. <https://doi.org/10.1002/tcr.201800153>.
- [173] M. Malakootian, F. Mansuri, Hexavalent chromium removal by titanium dioxide photocatalytic reduction and the effect of phenol and humic acid on its removal efficiency, *Int. J. Environ. Health Eng.* 4 (2015) 19. <https://doi.org/10.4103/2277-9183.157720>.
- [174] X. Yan, G. Ning, P. Zhao, Enhanced Visible Light Photocatalytic Reduction of Cr(VI) over a Novel Square Nanotube Poly(Triazine Imide)/TiO₂ Heterojunction, *Catalysts*. 9 (2019) 55. <https://doi.org/10.3390/catal9010055>.
- [175] A.A. Khodja, T. Sehili, J.-F. Pilichowski, P. Boule, Photocatalytic degradation of 2-phenylphenol on TiO₂ and ZnO in aqueous suspensions, *J. Photochem. Photobiol. A Chem.* 141 (2001) 231–239. [https://doi.org/10.1016/S1010-6030\(01\)00423-3](https://doi.org/10.1016/S1010-6030(01)00423-3).
- [176] N. Sapawe, A.A. Jalil, S. Triwahyono, S.H. Adam, N.F. Jaafar, M.A.H. Satar, Isomorphous substitution of Zr in the framework of aluminosilicate HY by an electrochemical method: Evaluation by methylene blue decolorization, *Appl. Catal. B Environ.* 125 (2012) 311–323. <https://doi.org/10.1016/j.apcatb.2012.05.042>.
- [177] A. Marucco, I. Fenoglio, F. Turci, B. Fubini, Interaction of fibrinogen and albumin with titanium dioxide nanoparticles of different crystalline phases, *J. Phys. Conf. Ser.* 429 (2013) 012014. <https://doi.org/10.1088/1742-6596/429/1/012014>.
- [178] I. Fenoglio, G. Greco, S. Livraghi, B. Fubini, Non-UV-Induced Radical Reactions at the Surface of TiO₂ Nanoparticles That May Trigger Toxic Responses, *Chem. - A Eur. J.* 15 (2009) 4614–4621. <https://doi.org/10.1002/chem.200802542>.
- [179] N.M. Mahmoodi, M. Arami, N.Y. Limaee, N.S. Tabrizi, Kinetics of heterogeneous photocatalytic degradation of reactive dyes in an immobilized TiO₂ photocatalytic reactor, *J. Colloid Interface Sci.* 295 (2006) 159–164. <https://doi.org/10.1016/j.jcis.2005.08.007>.
- [180] R. Comparelli, E. Fanizza, M.L. Curri, P.D. Cozzoli, G. Mascolo, A. Agostiano, UV-induced photocatalytic degradation of azo dyes by organic-capped ZnO nanocrystals immobilized onto substrates, *Appl. Catal. B Environ.* 60 (2005) 1–11. <https://doi.org/10.1016/j.apcatb.2005.02.013>.
- [181] S.N. Hosseini, S.M. Borghei, M. Vossoughi, N. Taghavinia, Immobilization of TiO₂ on perlite granules for photocatalytic degradation of phenol, *Appl. Catal. B Environ.* 74 (2007) 53–62. <https://doi.org/10.1016/j.apcatb.2006.12.015>.
- [182] M.A. Fukushima, K. Nakayasu, S. Tanaka, H. Nakamura, Speciation analysis of chromium after reduction of chromium (VI) by humic acid, *Toxicol. Environ. Chem.* 62 (1997) 207–215. <https://doi.org/10.1080/02772249709358508>.
- [183] G.C. Banik, S.K. Sanyav, A Study on Chromium-Humic Complexation: Part 2. Complexation Equilibria of Chromium-Humic/Fulvic Complexes, *J. Indian Soc. Soil Sci.* 54 (2006) 170–173. <https://doi.org/10.1016/j.envpol.2017.10.120>.
- [184] K.D. Jones, C.L. Tiller, Effect of Solution Chemistry on the Extent of Binding of Phenanthrene by a Soil Humic Acid: A Comparison of Dissolved and Clay Bound Humic, *Environ. Sci. Technol.* 33 (1999) 580–587. <https://doi.org/10.1021/es9803207>.

- [185] L. Weng, E.J.M. Temminghoff, S. Lofts, E. Tipping, W.H. Van Riemsdijk, Complexation with Dissolved Organic Matter and Solubility Control of Heavy Metals in a Sandy Soil, *Environ. Sci. Technol.* 36 (2002) 4804–4810. <https://doi.org/10.1021/es0200084>.
- [186] C. Pan, L.D. Troyer, P. Liao, J.G. Catalano, W. Li, D.E. Giammar, Effect of Humic Acid on the Removal of Chromium(VI) and the Production of Solids in Iron Electrocoagulation, *Environ. Sci. Technol.* 51 (2017) 6308–6318. <https://doi.org/10.1021/acs.est.7b00371>.
- [187] Y. Zhao, Y. Zhang, J. Li, X. Du, Solvothermal synthesis of visible-light-active N-modified ZrO₂ nanoparticles, *Mater. Lett.* 130 (2014) 139–142. <https://doi.org/10.1016/j.matlet.2014.05.093>.
- [188] N. Bashir, K.A. Razak, Z. Lockman, Synthesis of freestanding amorphous ZrO₂ nanotubes by anodization and their application in photoreduction of Cr(VI) under visible light, *Surf. Coatings Technol.* 320 (2017) 371–376. <https://doi.org/10.1016/j.surfcoat.2016.12.026>.
- [189] B. Nanda, A.C. Pradhan, K.M. Parida, Fabrication of mesoporous CuO/ZrO₂-MCM-41 nanocomposites for photocatalytic reduction of Cr(VI), *Chem. Eng. J.* 316 (2017) 1122–1135. <https://doi.org/10.1016/j.cej.2016.11.080>.
- [190] G. Colón, M.C. Hidalgo, J.A. Navío, Effect of ZrO₂ incorporation and calcination temperature on the photocatalytic activity of commercial TiO₂ for salicylic acid and Cr(VI) photodegradation, *Appl. Catal. A Gen.* 231 (2002) 185–199. [https://doi.org/10.1016/S0926-860X\(02\)00051-0](https://doi.org/10.1016/S0926-860X(02)00051-0).
- [191] N. Doufar, M. Benamira, H. Lahmar, M. Trari, I. Avramova, M.T. Caldes, Structural and photochemical properties of Fe-doped ZrO₂ and their application as photocatalysts with TiO₂ for chromate reduction, *J. Photochem. Photobiol. A Chem.* 386 (2020) 112105. <https://doi.org/10.1016/j.jphotochem.2019.112105>.
- [192] M. Hidalgo, G. Colon, J. Navio, M. Macias, V. Kriventsov, D. Kochubey, M. Tsodikov, EXAFS study and photocatalytic properties of un-doped and iron-doped ZrO₂-TiO₂ (photo-) catalysts, *Catal. Today.* 128 (2007) 245–250. <https://doi.org/10.1016/j.cattod.2007.07.010>.
- [193] S.G. Botta, J.A. Navío, M.C. Hidalgo, G.M. Restrepo, M.I. Litter, Photocatalytic properties of ZrO₂ and Fe/ZrO₂ semiconductors prepared by a sol–gel technique, *J. Photochem. Photobiol. A Chem.* 129 (1999) 89–99. [https://doi.org/10.1016/S1010-6030\(99\)00150-1](https://doi.org/10.1016/S1010-6030(99)00150-1).
- [194] Zhongyang Li, K. Kusakabe, S. Morooka, Preparation of thermostable amorphous Si–C–O membrane and its application to gas separation at elevated temperature, *J. Memb. Sci.* 118 (1996) 159–168. [https://doi.org/10.1016/0376-7388\(96\)00086-5](https://doi.org/10.1016/0376-7388(96)00086-5).
- [195] E. Eray, V. Boffa, M.K. Jørgensen, G. Magnacca, V.M. Candelario, Enhanced Fabrication of Silicon Carbide Membranes for Wastewater Treatment: from Laboratory to Industrial Scale, *J. Memb. Sci.* (2020) 118080. <https://doi.org/10.1016/j.memsci.2020.118080>.
- [196] E.W. Rice, R.B. Baird, A.D. Eaton, L.S. Clesceri, Standard methods for the examination of water and wastewater, American Public Health Association Washington, DC, 2012.
- [197] M. Naimi-Joubani, M. Shirzad-Siboni, J.K. Yang, M. Gholami, M. Farzadkia, Photocatalytic reduction of hexavalent chromium with illuminated ZnO/TiO₂ composite, *J. Ind. Eng. Chem.* 22 (2015) 317–323. <https://doi.org/10.1016/j.jiec.2014.07.025>.
- [198] Y. Ku, I.-L. Jung, Photocatalytic reduction of Cr(VI) in aqueous solutions by UV irradiation with the presence of titanium dioxide, *Water Res.* 35 (2001) 135–142. [https://doi.org/10.1016/S0043-1354\(00\)00098-1](https://doi.org/10.1016/S0043-1354(00)00098-1).
- [199] E. Selli, A. De Giorgi, G. Bidoglio, Humic acid-sensitized photoreduction of Cr(VI) on ZnO particles, *Environ. Sci. Technol.* 30 (1996) 598–604. <https://doi.org/10.1021/es950368+>.
- [200] M. Suchanek, E. Niewiara, K. Wilkosz, W.W. Kubiak, Nanopowders of Ytria-Stabilized Zirconia Doped

- with Rare Earth Elements as Adsorbents of Humic Acids, *Materials* (Basel). 12 (2019) 3915. <https://doi.org/10.3390/ma12233915>.
- [201] A. OHTA, H. KAGI, H. TSUNO, M. NOMURA, T. OKAI, Speciation study of Cr(VI/III) reacting with humic substances and determination of local structure of Cr binding humic substances using XAFS spectroscopy, *Geochem. J.* 46 (2013) 409–420. <https://doi.org/10.2343/geochemj.2.0222>.
- [202] N. Bashir, T.W. Kian, G. Kawamura, A. Matsuda, K.A. Razak, Z. Lockman, Sunlight activated anodic freestanding ZrO₂ nanotube arrays for Cr(VI) photoreduction, *Nanotechnology*. 29 (2018) 375701. <https://doi.org/10.1088/1361-6528/aaccbd>.
- [203] W.M. Haynes, *CRC Handbook of Chemistry and Physics*, CRC press, 2014.
- [204] M.D. Ward, J.R. White, A.J. Bard, Electrochemical investigation of the energetics of particulate titanium dioxide photocatalysts. The methyl viologen-acetate system, *J. Am. Chem. Soc.* 105 (1983) 27–31. <https://doi.org/10.1021/ja00339a007>.
- [205] S.-M. Lee, T.-W. Lee, B.-J. Choi, J.-K. Yang, Treatment of Cr(VI) and Phenol by Illuminated TiO₂, *J. Environ. Sci. Heal. Part A.* 38 (2003) 2219–2228. <https://doi.org/10.1081/ESE-120023356>.
- [206] T.C. Machado, M.A. Lansarin, N. Matte, Reduction of hexavalent chromium: Photocatalysis and photochemistry and their application in wastewater remediation, *Water Sci. Technol.* 70 (2014) 55–61. <https://doi.org/10.2166/wst.2014.193>.
- [207] E. Masolo, N. Senes, E. Pellicer, M.D. Baró, S. Enzo, M.I. Pilo, G. Mulas, S. Garroni, Evaluation of the anatase/rutile phase composition influence on the photocatalytic performances of mesoporous TiO₂ powders, *Int. J. Hydrogen Energy.* 40 (2015) 14483–14491. <https://doi.org/10.1016/j.ijhydene.2015.05.180>.
- [208] J. Munoz, X. Domenech, TiO₂ catalysed reduction of Cr(VI) in aqueous solutions under ultraviolet illumination, *J. Appl. Electrochem.* 20 (1990) 518–521. <https://doi.org/10.1007/BF01076066>.
- [209] Y. He, N.B. Sutton, H.H.H. Rijnaarts, A.A.M. Langenhoff, Degradation of pharmaceuticals in wastewater using immobilized TiO₂ photocatalysis under simulated solar irradiation, *Appl. Catal. B Environ.* 182 (2016) 132–141. <https://doi.org/10.1016/j.apcatb.2015.09.015>.
- [210] A. Rey, P. García-Muñoz, M.D. Hernández-Alonso, E. Mena, S. García-Rodríguez, F.J. Beltrán, WO₃-TiO₂ based catalysts for the simulated solar radiation assisted photocatalytic ozonation of emerging contaminants in a municipal wastewater treatment plant effluent, *Appl. Catal. B Environ.* 154–155 (2014) 274–284. <https://doi.org/10.1016/j.apcatb.2014.02.035>.
- [211] E. Álvarez-Ayuso, A. García-Sánchez, X. Querol, Adsorption of Cr(VI) from synthetic solutions and electroplating wastewaters on amorphous aluminium oxide, *J. Hazard. Mater.* 142 (2007) 191–198. <https://doi.org/10.1016/j.jhazmat.2006.08.004>.
- [212] B. Wu, L. Zhang, S. Wei, L. Ou'Yang, R. Yin, S. Zhang, Reduction of chromate with UV/diacetyl for the final effluent to be below the discharge limit, *J. Hazard. Mater.* 389 (2020) 121841. <https://doi.org/10.1016/j.jhazmat.2019.121841>.
- [213] S. Li, C. Wei, L. Zhou, P. Wang, Q. Meng, Z. Xie, Sol-gel derived zirconia membrane on silicon carbide substrate, *J. Eur. Ceram. Soc.* (2019) 0–1. <https://doi.org/10.1016/j.jeurceramsoc.2019.04.054>.
- [214] H. Qi, G. Zhu, L. Li, N. Xu, Fabrication of a sol-gel derived microporous zirconia membrane for nanofiltration, *J. Sol-Gel Sci. Technol.* 62 (2012) 208–216. <https://doi.org/10.1007/s10971-012-2711-0>.
- [215] T. Okubo, T. Takahashi, M. Sadakata, H. Nagamoto, Crack-free porous YSZ membrane via controlled synthesis of zirconia sol, *J. Memb. Sci.* 118 (1996) 151–157. [https://doi.org/10.1016/0376-7388\(96\)00085-3](https://doi.org/10.1016/0376-7388(96)00085-3).
- [216] Y. Zhou, M. Fukushima, H. Miyazaki, Y. ichi Yoshizawa, K. Hirao, Y. Iwamoto, K. Sato, Preparation and

- characterization of tubular porous silicon carbide membrane supports, *J. Memb. Sci.* 369 (2011) 112–118. <https://doi.org/10.1016/j.memsci.2010.11.055>.
- [217] M. Niederberger, Nonaqueous sol-gel routes to metal oxide nanoparticles, *Acc. Chem. Res.* 40 (2007) 793–800. <https://doi.org/10.1021/ar600035e>.
- [218] C. Guizard, A. Ayrat, M. Barboiu, A. Julbe, Sol-Gel Processed Membranes, in: L. Klein, M. Aparicio, A. Jitianu (Eds.), *Handb. Sol-Gel Sci. Technol.*, Springer International Publishing, Cham, 2016: pp. 1–47. https://doi.org/10.1007/978-3-319-19454-7_58-1.
- [219] J.E. Zhou, Q. Chang, Y. Wang, J. Wang, G. Meng, Separation of stable oil-water emulsion by the hydrophilic nano-sized ZrO₂ modified Al₂O₃ microfiltration membrane, *Sep. Purif. Technol.* 75 (2010) 243–248. <https://doi.org/10.1016/j.seppur.2010.08.008>.
- [220] W. Balcerzak, J. Kwaśny, M. Kryłów, Oily wastewater treatment using a zirconia ceramic membrane : a literature review, *Arch. Environ. Prot.* 44 (2018) 3. <https://doi.org/10.24425/122293>.
- [221] R. Cano-Crespo, B.M. Moshtaghion, D. Gómez-García, R. Moreno, A. Domínguez-Rodríguez, Graphene or carbon nanofiber-reinforced zirconia composites: Are they really worthwhile for structural applications?, *J. Eur. Ceram. Soc.* 38 (2018) 3994–4002. <https://doi.org/10.1016/j.jeurceramsoc.2018.04.045>.
- [222] R. Greenwood, K. Kendall, Selection of Suitable Dispersants for Aqueous Suspensions of Zirconia and Titania Powders using Acoustophoresis, *J. Eur. Ceram. Soc.* 19 (1999) 479–488. [https://doi.org/10.1016/S0955-2219\(98\)00208-8](https://doi.org/10.1016/S0955-2219(98)00208-8).
- [223] S.P. Rao, S.S. Tripathy, A.M. Raichur, Dispersion studies of sub-micron zirconia using Dolapix CE 64, *Colloids Surfaces A Physicochem. Eng. Asp.* 302 (2007) 553–558. <https://doi.org/10.1016/j.colsurfa.2007.03.034>.
- [224] C. Das, S. Bose, *Advanced ceramic membranes and applications*, CRC Press, 2017.
- [225] F. Shojai, T. Mäntylä, Monoclinic zirconia microfiltration membranes: preparation and characterization, *J. Porous Mater.* 8 (2001) 129–142. <https://doi.org/10.1023/A:1009694709010>.
- [226] T. Fengqiu, H. Xiaoxian, Z. Yufeng, G. Jingkun, Effect of dispersants on surface chemical properties of nano-zirconia suspensions, *Ceram. Int.* 26 (2000) 93–97. [https://doi.org/10.1016/S0272-8842\(99\)00024-3](https://doi.org/10.1016/S0272-8842(99)00024-3).
- [227] P. Boch, J.-C. Niepce, *Ceramic Materials: Processes, Properties, and Applications*, John Wiley & Sons, 2010.
- [228] A. Pettersson, G. Marino, A. Pursiheimo, J.B. Rosenholm, Electrosteric Stabilization of Al₂O₃, ZrO₂, and 3Y-ZrO₂ Suspensions: Effect of Dissociation and Type of Polyelectrolyte, *J. Colloid Interface Sci.* 228 (2000) 73–81. <https://doi.org/10.1006/jcis.2000.6939>.
- [229] B.A. Silva, V. De Souza, G. De Oliveira, M. Di Luccio, D. Hotza, K. Rezwan, M. Wilhelm, Characterization of functionalized zirconia membranes manufactured by aqueous tape casting, *Ceram. Int.* (2020). <https://doi.org/10.1016/j.ceramint.2020.03.162>.
- [230] J. Cesarano, I.A. Aksay, A. Bleier, Stability of Aqueous alpha-Al₂O₃ Suspensions with Poly(methacrylic acid) Polyelectrolyte, *J. Am. Ceram. Soc.* 71 (1988) 250–255. <https://doi.org/10.1111/j.1151-2916.1988.tb05855.x>.
- [231] X. Ding, Y. Fan, N. Xu, A new route for the fabrication of TiO₂ ultrafiltration membranes with suspension derived from a wet chemical synthesis, *J. Memb. Sci.* 270 (2006) 179–186. <https://doi.org/10.1016/j.memsci.2005.07.003>.
- [232] M.R.O. and H. Mukhtar, Review on Development of Ceramic Membrane From Sol-Gel Route: Parameters Affecting Characteristics of the Membrane, *IJUM Eng. J.* 1 (2000) 1–6. <https://doi.org/10.31436/iiumej.v1i2.334>.

- [233] X. Ju, P. Huang, N. Xu, J. Shi, Influences of sol and phase stability on the structure and performance of mesoporous zirconia membranes, *J. Memb. Sci.* 166 (2000) 41–50. [https://doi.org/10.1016/S0376-7388\(99\)00243-4](https://doi.org/10.1016/S0376-7388(99)00243-4).
- [234] F. Snijkers, A. de Wilde, S. Mullens, J. Luyten, Aqueous tape casting of yttria stabilised zirconia using natural product binder, *J. Eur. Ceram. Soc.* 24 (2004) 1107–1110. [https://doi.org/10.1016/S0955-2219\(03\)00388-1](https://doi.org/10.1016/S0955-2219(03)00388-1).
- [235] M.P. Albano, L.B. Garrido, K. Plucknett, L.A. Genova, Processing of porous yttria-stabilized zirconia tapes: Influence of starch content and sintering temperature, *Ceram. Int.* 35 (2009) 1783–1791. <https://doi.org/10.1016/j.ceramint.2008.10.003>.
- [236] R.V. Kumar, A.K. Ghoshal, G. Pugazhenthii, Fabrication of zirconia composite membrane by in-situ hydrothermal technique and its application in separation of methyl orange, *Ecotoxicol. Environ. Saf.* 121 (2015) 73–79. <https://doi.org/10.1016/j.ecoenv.2015.05.006>.
- [237] Y.S. Lin, C.H. Chang, R. Gopalan, Improvement of Thermal Stability of Porous Nanostructured Ceramic Membranes, *Ind. Eng. Chem. Res.* 33 (1994) 860–870. <https://doi.org/10.1021/ie00028a012>.
- [238] J. Etienne, A. Larbot, A. Julbe, C. Guizard, L. Cot, A microporous zirconia membrane prepared by the sol-gel process from zirconyl oxalate, *J. Memb. Sci.* 86 (1994) 95–102. [https://doi.org/10.1016/0376-7388\(93\)E0141-6](https://doi.org/10.1016/0376-7388(93)E0141-6).
- [239] S.D. Ramamurthi, Z. Xu, D.A. Payne, Nanometer-Sized ZrO₂ Particles Prepared by a Sol-Emulsion-Gel Method, *J. Am. Ceram. Soc.* 73 (1990) 2760–2763.
- [240] K.B. Singh, M.S. Tirumkudulu, Cracking in Drying Colloidal Films, *Phys. Rev. Lett.* 98 (2007) 218302. <https://doi.org/10.1103/PhysRevLett.98.218302>.
- [241] M.S. Tirumkudulu, W.B. Russel, Cracking in Drying Latex Films, *Langmuir.* 21 (2005) 4938–4948. <https://doi.org/10.1021/la048298k>.
- [242] W.P. Yang, S.S. Shyu, E.-S. Lee, A.-C. Chao, Effects of Poly(Vinyl Alcohol) Content and Calcination Temperature on the Characteristics of Unsupported Alumina Membrane, *Sep. Sci. Technol.* 31 (1996) 1327–1343. <https://doi.org/10.1080/01496399608006954>.
- [243] M. Copel, M. Gribelyuk, E. Gusev, Structure and stability of ultrathin zirconium oxide layers on Si(001), *Appl. Phys. Lett.* 76 (2000) 436–438. <https://doi.org/10.1063/1.125779>.
- [244] J.P. Chang, Y.-S. Lin, S. Berger, A. Kepten, R. Bloom, S. Levy, Ultrathin zirconium oxide films as alternative gate dielectrics, *J. Vac. Sci. Technol. B Microelectron. Nanom. Struct.* 19 (2001) 2137. <https://doi.org/10.1116/1.1415513>.
- [245] S. Ognier, C. Wisniewski, A. Grasmick, Characterisation and modelling of fouling in membrane bioreactors, *Desalination.* 146 (2002) 141–147. [https://doi.org/10.1016/S0011-9164\(02\)00508-8](https://doi.org/10.1016/S0011-9164(02)00508-8).
- [246] J. Kaewsuk, G.T. Seo, Computational study of NF membrane removal in rejection of specific NOM compounds, *Desalin. Water Treat.* 51 (2013) 6218–6223. <https://doi.org/10.1080/19443994.2013.780788>.
- [247] F. de Souza, S.R. Bragança, Extraction and characterization of humic acid from coal for the application as dispersant of ceramic powders, *J. Mater. Res. Technol.* 7 (2018) 254–260. <https://doi.org/10.1016/j.jmrt.2017.08.008>.
- [248] G. Zhan, C. Li, D. Luo, Electrochemical Investigation of Bovine Hemoglobin at an Acetylene Black Paste Electrode in the Presence of Sodium Dodecyl Sulfate, *Bull. Korean Chem. Soc.* 28 (2007) 1720–1724. <https://doi.org/10.5012/bkcs.2007.28.10.1720>.
- [249] B. Braunschweig, W. Peukert, Protein Adsorption at the Electrically Charged Air – Water Interface: Implications on Foam Stability, (2012).

- [250] J.-H.H. Eom, Y.-W.W. Kim, S.-H.H. Yun, I.-H.H. Song, Low-cost clay-based membranes for oily wastewater treatment, *J. Ceram. Soc. Japan.* 122 (2014) 788–794. <https://doi.org/10.2109/jcersj.2.122.788>.
- [251] Y. Zhang, X. Shan, Z. Jin, Y. Wang, Synthesis of sulfated Y-doped zirconia particles and effect on properties of polysulfone membranes for treatment of wastewater containing oil, *J. Hazard. Mater.* 192 (2011) 559–567. <https://doi.org/10.1016/j.jhazmat.2011.05.058>.
- [252] Q. Chang, J. Zhou, Y. Wang, J. Wang, G. Meng, Hydrophilic modification of Al₂O₃ microfiltration membrane with nano-sized γ -Al₂O₃ coating, *Desalination.* 262 (2010) 110–114. <https://doi.org/10.1016/j.desal.2010.05.055>.
- [253] F. Shojai, T. Mäntylä, Structural stability of yttria doped zirconia membranes in acid and basic aqueous solutions, *J. Eur. Ceram. Soc.* 21 (2001) 37–44. [https://doi.org/10.1016/S0955-2219\(00\)00163-1](https://doi.org/10.1016/S0955-2219(00)00163-1).
- [254] T. Van Gestel, C. Vandecasteele, A. Buekenhoudt, C. Dotremont, J. Luyten, B. Van Der Bruggen, G. Maes, Corrosion properties of alumina and titania NF membranes, *J. Memb. Sci.* 214 (2003) 21–29. [https://doi.org/10.1016/S0376-7388\(02\)00517-3](https://doi.org/10.1016/S0376-7388(02)00517-3).
- [255] U. Aust, T. Moritz, U. Popp, G. Tomandl, Direct synthesis of ceramic membranes by sol-gel process, *J. Sol-Gel Sci. Technol.* 26 (2003) 715–720. <https://doi.org/10.1023/A:1020789903666>.
- [256] D. Li, H. Wang, W. Jing, Y. Fan, W. Xing, Fabrication of mesoporous TiO₂ membranes by a nanoparticle-modified polymeric sol process, *J. Colloid Interface Sci.* 433 (2014) 43–48. <https://doi.org/10.1016/j.jcis.2014.05.026>.
- [257] N. Barbero, D. Vione, Why Dyes Should Not Be Used to Test the Photocatalytic Activity of Semiconductor Oxides, *Environ. Sci. Technol.* 50 (2016) 2130–2131. <https://doi.org/10.1021/acs.est.6b00213>.
- [258] G. Witz, V. Shklover, W. Steurer, S. Bachegowda, H.P. Bossmann, Phase evolution in yttria-stabilized zirconia thermal barrier coatings studied by rietveld refinement of X-ray powder diffraction patterns, *J. Am. Ceram. Soc.* 90 (2007) 2935–2940. <https://doi.org/10.1111/j.1551-2916.2007.01785.x>.
- [259] H.G. Scott, Phase relationships in the zirconia-yttria system, *J. Mater. Sci.* 10 (1975) 1527–1535. <https://doi.org/10.1007/BF01031853>.
- [260] N. Veronovski, P. Andreozzi, C. La Mesa, M. Sfiligoj-Smole, Stable TiO₂ dispersions for nanocoating preparation, *Surf. Coatings Technol.* 204 (2010) 1445–1451. <https://doi.org/10.1016/j.surfcoat.2009.09.041>.
- [261] S. Ciston, R.M. Lueptow, K.A. Gray, Bacterial attachment on reactive ceramic ultrafiltration membranes, *J. Memb. Sci.* 320 (2008) 101–107. <https://doi.org/10.1016/j.memsci.2008.03.065>.
- [262] T. Ohno, K. Sarukawa, K. Tokieda, M. Matsumura, Morphology of a TiO₂ Photocatalyst (Degussa, P-25) Consisting of Anatase and Rutile Crystalline Phases, *J. Catal.* 203 (2001) 82–86. <https://doi.org/10.1006/jcat.2001.3316>.
- [263] D.A.H. Hanaor, C.C. Sorrell, Review of the anatase to rutile phase transformation, *J. Mater. Sci.* 46 (2011) 855–874. <https://doi.org/10.1007/s10853-010-5113-0>.
- [264] M.K. Akhtar, S.E. Pratsinis, S.V.R. Mastrangelo, Dopants in Vapor-Phase Synthesis of Titania Powders, *J. Am. Ceram. Soc.* 75 (1992) 3408–3416. <https://doi.org/10.1111/j.1551-2916.1992.tb04442.x>.
- [265] J. Tauc, R. Grigorovici, A. Vancu, Optical Properties and Electronic Structure of Amorphous Germanium, *Phys. Status Solidi.* 15 (1966) 627–637. <https://doi.org/10.1002/pssb.19660150224>.
- [266] B. Menezes, D. Moreira, H. Oliveira, L. Marques, J. Lima, Solvothermal Synthesis of Cerium-Doped Titania Nanostructured Materials Modified with Acetylacetone for Solar-Driven Photocatalysis, *J. Braz. Chem. Soc.* (2020). <https://doi.org/10.21577/0103-5053.20190148>.
- [267] F.E. Bortot Coelho, V.M. Candelario, E.M.R. Araújo, T.L.S. Miranda, G. Magnacca, Photocatalytic

- Reduction of Cr(VI) in the Presence of Humic Acid Using Immobilized Ce–ZrO₂ under Visible Light, *Nanomaterials*. 10 (2020) 779. <https://doi.org/10.3390/nano10040779>.
- [268] H.E. Garrafa-Gálvez, C.G. Alvarado-Beltrán, J.L. Almaral-Sánchez, A. Hurtado-Macías, A.M. Garzon-Fontecha, P.A. Luque, A. Castro-Beltrán, Graphene role in improved solar photocatalytic performance of TiO₂-RGO nanocomposite, *Chem. Phys.* 521 (2019) 35–43. <https://doi.org/10.1016/j.chemphys.2019.01.013>.
- [269] G.D. Parfitt, Surface Chemistry of Oxides, *Pure Appl. Chem.* 48 (1976) 415–418. <https://doi.org/10.1351/pac197648040415>.
- [270] D.L. Liao, G.S. Wu, B.Q. Liao, Zeta potential of shape-controlled TiO₂ nanoparticles with surfactants, *Colloids Surfaces A Physicochem. Eng. Asp.* 348 (2009) 270–275. <https://doi.org/10.1016/j.colsurfa.2009.07.036>.
- [271] M. Kosmulski, P. Próchniak, J.B. Rosenholm, Letter: The IEP of Carbonate-Free Neodymium(III) Oxide, *J. Dispers. Sci. Technol.* 30 (2009) 589–591. <https://doi.org/10.1080/01932690902766319>.
- [272] S.Z.A. Bukhari, J. Ha, J. Lee, I. Song, Effect of different heat treatments on oxidation-bonded SiC membrane for water filtration, *Ceram. Int.* 44 (2018) 14251–14257. <https://doi.org/10.1016/j.ceramint.2018.05.029>.
- [273] K. Boussu, B. Van der Bruggen, A. Volodin, C. Van Haesendonck, J.A. Delcour, P. Van der Meeren, C. Vandecasteele, Characterization of commercial nanofiltration membranes and comparison with self-made polyethersulfone membranes, *Desalination*. 191 (2006) 245–253. <https://doi.org/10.1016/j.desal.2005.07.025>.
- [274] N. Aryanti, A. Saraswati, R. Pratama Putra, A. Nafiunisa, D.H. Wardhani, FOULING MECHANISM OF MICELLE ENHANCED ULTRAFILTRATION WITH SDS SURFACTANT FOR INDIGOZOL DYE REMOVAL, *J. Teknol.* 80 (2018) 29–36. <https://doi.org/10.11113/jt.v80.12741>.
- [275] L.F. Albuquerque, A.A. Salgueiro, J.L. de S. Melo, O. Chiavone-Filho, Coagulation of indigo blue present in dyeing wastewater using a residual bitter, *Sep. Purif. Technol.* 104 (2013) 246–249. <https://doi.org/10.1016/j.seppur.2012.12.005>.
- [276] A.R. Tehrani-Bagha, K. Holmberg, Solubilization of hydrophobic dyes in surfactant solutions, *Materials (Basel)*. 6 (2013) 580–608. <https://doi.org/10.3390/ma6020580>.
- [277] M. Mahzoura, N. Tahri, M. Daramola, J. Duplay, G. Schäfer, R. Ben Amar, M. Mahzoura, N. Tahri, M. Daramola, J. Duplay, G. Schäfer, Comparative investigation of indigo blue dye removal efficiency of activated carbon and natural clay in adsorption / ultrafiltration system To cite this version : HAL Id : hal-02323260, (2020).
- [278] D. Shen, J. Fan, W. Zhou, B. Gao, Q. Yue, Q. Kang, Adsorption kinetics and isotherm of anionic dyes onto organo-bentonite from single and multisolute systems, *J. Hazard. Mater.* 172 (2009) 99–107. <https://doi.org/10.1016/j.jhazmat.2009.06.139>.
- [279] C. Li, W. Sun, Z. Lu, X. Ao, C. Yang, S. Li, Systematic evaluation of TiO₂-GO-modified ceramic membranes for water treatment: Retention properties and fouling mechanisms, *Chem. Eng. J.* 378 (2019) 122138. <https://doi.org/10.1016/j.cej.2019.122138>.
- [280] Z.G. Peng, K. Hidajat, M.S. Uddin, Adsorption of bovine serum albumin on nanosized magnetic particles, *J. Colloid Interface Sci.* 271 (2004) 277–283. <https://doi.org/10.1016/j.jcis.2003.12.022>.
- [281] D.H.G. Pelegrine, C.A. Gasparetto, Whey proteins solubility as function of temperature and pH, *LWT - Food Sci. Technol.* 38 (2005) 77–80. <https://doi.org/10.1016/j.lwt.2004.03.013>.
- [282] A. Larbot, J. -P Fabre, C. Guizard, L. Cot, J. Gillot, New Inorganic Ultrafiltration Membranes: Titania and Zirconia Membranes, *J. Am. Ceram. Soc.* 72 (1989) 257–261. <https://doi.org/10.1111/j.1151-2916.1989.tb06111.x>.

- [283] M. Sarro, N.P. Gule, E. Laurenti, R. Gamberini, M.C. Paganini, P.E. Mallon, P. Calza, ZnO-based materials and enzymes hybrid systems as highly efficient catalysts for recalcitrant pollutants abatement, *Chem. Eng. J.* 334 (2018) 2530–2538. <https://doi.org/10.1016/j.cej.2017.11.146>.
- [284] E. Cerrato, C. Gionco, I. Berruti, F. Sordello, P. Calza, M.C. Paganini, Rare earth ions doped ZnO: Synthesis, characterization and preliminary photoactivity assessment, *J. Solid State Chem.* 264 (2018) 42–47. <https://doi.org/10.1016/j.jssc.2018.05.001>.
- [285] V. Diesen, M. Jonsson, Formation of H₂O₂ in TiO₂ Photocatalysis of Oxygenated and Deoxygenated Aqueous Systems: A Probe for Photocatalytically Produced Hydroxyl Radicals, *J. Phys. Chem. C.* 118 (2014) 10083–10087. <https://doi.org/10.1021/jp500315u>.
- [286] Z. Jiang, L. Wang, J. Lei, Y. Liu, J. Zhang, Photo-Fenton degradation of phenol by CdS/rGO/Fe²⁺ at natural pH with in situ-generated H₂O₂, *Appl. Catal. B Environ.* 241 (2019) 367–374. <https://doi.org/10.1016/j.apcatb.2018.09.049>.
- [287] E.-E. Chang, Y.-C. Chang, C.-H. Liang, C.-P. Huang, P.-C. Chiang, Identifying the rejection mechanism for nanofiltration membranes fouled by humic acid and calcium ions exemplified by acetaminophen, sulfamethoxazole, and triclosan, *J. Hazard. Mater.* 221–222 (2012) 19–27. <https://doi.org/10.1016/j.jhazmat.2012.03.051>.
- [288] R. Wang, K. Hashimoto, A. Fujishima, M. Chikuni, E. Kojima, A. Kitamura, M. Shimohigoshi, T. Watanabe, Photogeneration of Highly Amphiphilic TiO₂ Surfaces, *Adv. Mater.* 10 (1998) 135–138. [https://doi.org/10.1002/\(SICI\)1521-4095\(199801\)10:2<135::AID-ADMA135>3.0.CO;2-M](https://doi.org/10.1002/(SICI)1521-4095(199801)10:2<135::AID-ADMA135>3.0.CO;2-M).

7. APPENDIX A: PUBLICATIONS

1. Bortot Coelho, F. E., Gionco, C., Paganini, M., Calza, P., and Magnacca, G. “Control of Membrane Fouling in Organics Filtration Using Ce-Doped Zirconia and Visible Light”, *Nanomaterials* **2019**, 9, 534. <https://doi.org/10.3390/nano9040534>
2. Janowska, K., Boffa, V., Jørgensen, M.K. *et al.* Thermocatalytic membrane distillation for clean water production. *npj Clean Water* **2020**, 3, 34. <https://doi.org/10.1038/s41545-020-00082-2>.
3. Bortot Coelho, F.E.; Candelario, V.M.; Araújo, E.M.R.; Miranda, T.L.S.; Magnacca, G. Photocatalytic Reduction of Cr(VI) in the Presence of Humic Acid Using Immobilized Ce–ZrO₂ under Visible Light. *Nanomaterials* **2020**, 10, 779, <https://10.3390/nano10040779>
4. Bortot Coelho, F.E.; Kaiser N. N.; Magnacca, G.; Candelario, V.M. Novel ZrO₂/SiC Ultrafiltration Membranes with Low Fouling and High Chemical Resistance. *Journal of Membrane Science*. **Submitted**
5. Bortot Coelho, F.E.; Deemter, D.; Candelario, V.M.; Boffa, V.; Magnacca, G. Development of Photocatalytic Zirconia-Titania Ultrafiltration Membranes with Anti-fouling Properties. *Chemical Engineering Journal*. **Submitted**
6. Bortot Coelho, F.E.; Lucchesi, C.; Magnacca, G.; Azo Dyes Degradation Using a Perovskite: Catalysis Explained by an Environmental Friendly Experiment. *Journal of Chemical Education*. **In preparation**
7. Bortot Coelho, F.E.; Candelario V.M.; Magnacca, G. A Review on the Fabrication of ZrO₂ Membranes: from Micro to Nanofiltration. *Journal of the European Ceramic Society*. **In preparation**
8. Eray, E.; Bortot Coelho, F.E.; Boffa, V.; Magnacca, G.; Candelario, V.M. Microporous SiC membranes. **In preparation**

8. APPENDIX B: PERIODS ABROAD

Period	Location	Supervisor
2018 (August-September)	Aalborg University, Department	Prof. Vittorio Boffa.
2020 (September-October)	of Chemistry and Bioscience, Denmark	
2019 (August-October)	Liqtech International A/S,	Dr. Victor M.
2020 (1-14 November)	Denmark	Candelario
2020/21 (15 November - 15 February)	Plataforma Solar de Almería, Spain	Dr. Sixto Malato Dr. Isabel Oller

9. APPENDIX C: DIDACTIC WORK

Oral presentations

1. Bortot Coelho, F.E. Use of membranes for water purification: some case studies, *NIS Colloquium*, 17 May 2019, Turin, Italy.
2. Bortot Coelho, F.E.; Magnacca, G. Photocatalytic Reduction of Cr(VI) in the Presence of Humic Acid using Ce-ZrO₂ under visible light, *International Conference on Chemical Energy and Semiconductor Photochemistry (CESCOP 2019)*, 4-6 September 2019, Trabzon, Turkey - Book of Abstracts (page 46).
3. Bortot Coelho, F.E.; Candelario, V.M.; Magnacca, G. Photocatalytic Ultrafiltration ZrO₂/TiO₂ Membrane, *17th Network Young Membranes Meeting (NYM 2020)*, 3-4 December 2020, Manchester, United Kingdom.

Poster presentations

1. Gionco, C.; Bortot Coelho, F. E.; Fabbri, D.; Cerruti, M.; Magnacca, G.; Calza, P.; Paganini, M.C. Metal oxide photocatalysts supported on reduced graphene oxide self-standing structures: a new perspective for wastewater treatment. *10th European meeting on Solar Chemistry and Photocatalysis: Environmental Applications (SPEA10)*, 4-8 June 2018, Almeria, Spain.
2. Janowska, K.; Bortot Coelho, F.E.; Deganello, F.; Magnacca, G.; Boffa, V. Catalytic activity of doped SrFeO_{3-δ} perovskite-type oxide ceramics for degradation of water pollutants, *2nd*

Nordic Conference on Ceramic and Glass Technology, 10-11 December **2018**, Roskilde, Denmark.

3. Bortot Coelho, F. E.; Gionco, C.; Paganini, M.C.; Magnacca, G. Development of a Ce-doped ZrO₂ Photocatalyst for the Degradation of Humic Acid, *International Winter School in "Innovative Catalysis and Sustainability"*, 7-11 January **2019**, Bardonecchia, Italy – Book of Abstracts (page 35).
4. Bortot Coelho, F. E.; Gionco, C.; Paganini, M.C.; Magnacca, G. Control of Membrane Fouling in Organics Separation Using Ce-doped Zirconia under Visible Light, 6th Marie Curie Alumni Association (MCAA), General Assembly and Annual Conference, 23-24 February **2019**, Vienna, Austria.– Book of Abstracts (page 85).
5. Bortot Coelho, F. E.; Paganini, M.C.; Magnacca, G. Membrane fouling mitigation by organics degradation using Ce-doped Zirconia photocatalyst, *6th European Conference on Environmental Applications of Advanced Oxidation Processes (EAAOP-6)*, 26-30 June **2019**, Portoroz, Slovenia.
6. Bortot Coelho, F.E.; Kaiser N. N.; Magnacca, G.; Candelario, V.M. Photocatalytic ultrafiltration ZrO₂/TiO₂ -membrane, *2th International Congress on Membranes & Membrane Processes 2020 (ICOM 2020)*, 7-11 December **2020**, London, United Kingdom.

Outreach Activities - Public Engagement

1. Presentation of AQUAlity project: Stand + experiments. *Notte dei Ricercatori 2018 (European Researchers' Night 2018)*. Università del Piemonte Orientale (UPO), 28 Sep **2018**, Alessandria, Italy
2. Demonstration activity (experiment) and Power Point presentation entitled "Removal of pollutants with a thermo-catalyst". *AQUAlity Lab*. University of Turin, 18 Feb **2019**, Turin, Italy.
3. Presentation of AQUAlity project and LiqTech membranes: Pollutants and Water Treatment, ForskarFredag ("Researchers' Friday"), European Researcher's Night 2019, 27 Sep **2019**, Lund Sweden.

4. Video: Abbattimento degli inquinanti dell'acqua con un termo catalizzatore. Notte Europea dei Ricercatori 2020 (European Researchers Night 2020, University of Turin, 27 Nov **2020**, Turin, Italy. <https://www.youtube.com/watch?v=A2MQjPXAsro>)

PhD Courses Attended

University of Turin, Department of Chemistry:

Course title	Instructor	Hours	CFU
Determination of specific surface area and porosity of solid materials	Giuliana Magnacca	8	2
Reactive Species in the Photochemical Treatment of Water	Daniel Mártire and Marco Minella	16	4
Patenting and Knowledge Transfer	Marco Venturello	4	1
Lean thinking	Alessandra Bianco Prevot	4	1
Interactive laboratory to stimulate an attitude to outreach activities on basic physico-chemical phenomena	Giuliana Magnacca/ Gloria Berlier	12	3
Giornate del CrisDi: X-ray Powder Diffraction: a useful tool for Chemistry and Material Science	Domenica Marabello	4	1
The vitreous state	Livio Battezzati	12	3
Chemical Sensors for Scientific Research and Everyday Life	Ornella Abollino	8	2

PhD Schools Attended

1. Summer School on Photochemistry and Depollution – Clermond-Ferrand, France, 25-27 April **2018**.
2. 35th European Membrane Society (EMS) Summer School - Enschede, Netherlands, 24-29 June **2018**.
3. International Summer School on Micropollutant Analysis and Abatement - Aalborg, Denmark, 27-29 August **2018**.
4. Innovative Catalysis and Sustainability - International Winter School – Bardonecchia, Italy, 7-11 January **2019**.

5. International Winter School on Mass Spectrometry, Ecole Polytechnique, Palaiseau, France, 4-5 March **2019**.
6. 3rd European Summer School on Environmental Applications of Advanced Oxidation Processes. Alcoy, Spain, 3-7 June **2019**.
7. Summer School on “Introduction to Basic Statistical Tools and Data Analysis in Research”, University of Ioannina (Greece) and University of Piemonte Orientale (Italy), 23-24 September **2020**.

Seminars, Conferences Attended

1. First AQUALity Symposium - Clermont-Ferrand, France, 23-24 April **2018**.
2. 10th European meeting on Solar Chemistry and Photocatalysis: Environmental Applications (SPEA10) – Spain, 4-8 June **2018**.
3. Second AQUALity Symposium – Aalborg, Denmark, 30-31 August **2018**.
4. 6th Marie Curie Alumni Association (MCAA) General Assembly and Annual Conference, Vienna, Austria, 23-24 February **2019**.
5. Workshop on Prioritisation of emerging contaminants in Urban Wastewater, Ecole Polytechnique, Palaiseau, France, 6 March **2019**.
6. Third AQUALity Symposium – Palaiseau, France, 7-8 March **2019**.
7. NIS colloquium - AQUALity & Project Ô: a combined strategy to address water reuse, Turin, Italy, 16-17 May **2019**.
8. 6th European Conference on Environmental Applications of Advanced Oxidation Processes (EAAOP-6), Portoroz, Slovenia, 26-30 June **2019**.
9. Forth AQUALity Symposium, Trabzon, Turkey, 2-3 September **2019**.
10. International Conference on Chemical Energy and Semiconductor Photochemistry (CESCOP 2019), Trabzon, Turkey, 4-6 September **2019**.

11. Fifth AQUALity Symposium, Greece (Held remotely), 6 April **2020**.
12. Webinar: “Open science and the reward system: how can they be aligned?”, Netherlands, 2 July **2020**.
13. Sixty AQUALity Symposium, Spain (Held remotely), 22 September **2020**.
14. NanoInnovation 2020, Italy (Online event), 15-18 November **2020**.
15. Webinar: “Advances and challenges in the measurement of contaminants of emerging concern (and transformation products) in environmental matrices”, University of Almeria (Spain), 23 November **2020**.
16. 17th Network Young Membrains Meeting (NYM 2020), Manchester (United Kingdom), 3-4 December **2020**.
17. 2th International Congress on Membranes & Membrane Processes 2020 (ICOM 2020), London (United Kingdom), 7-11 December **2020**.
18. Webinar: “Toxicity tests: methods and relevance for water/wastewater treatment by AOPs”, CIEMAT-Plataforma Solar de Almeria (Spain), 16 December **2020**.
19. Webinar: “EU versus Italian Water Management”, Società Metropolitana Acque Torino (SMAT) - Italy, 18 January **2021**.
20. Webinar: “Preparation and characterization of photocatalysts for environmental applications”, Instituto de Tecnología Química - Universitat Politècnica de Valencia (Spain), 27 January **2021**.
21. Seventh AQUALity Symposium, Held remotely, 1-2 March **2021**.

Collaborations

1. Abatement of contaminants with a thermocatalyst based on the perovskite cerium doped strontium ferrite. In collaboration with Vittorio Boffa, Aalborg University (Denmark), and Francesca Deganello, Istituto per lo Studio dei Materiali Nanostrutturati UOS Palermo (Italy).

2. Removal of Cr(VI) from wastewaters using Ce-ZrO₂ photocatalyst. In collaboration with Tania Lucia Santos Miranda and Adriane Salum from the Chemical Engineering Department of the Federal University of Minas Gerais (Brazil).

Referee

- Reviewer for papers submitted in the Advances in Chemical Engineering and Science.
<https://www.scirp.org/journal/aces/>

Supervision

- Preparation of a second level laurea degree (Corelatore). Chiara Lucchesi Corso di laurea in Chimica Industriale 2019/2020, Dipartimento di Chimica, University of Turin.

ACKNOWLEDGMENTS

This PhD thesis is part of a project that has received funding from the European Union's Horizon 2020 research and innovation programme under the Marie Skłodowska-Curie grant agreement No 765860.

Unmeasurable thanks to my supervisor, Prof. Giuliana Magnacca, which took me as her own son from day one, and made this work possible. You thought me how a smile helps when everything seems wrong. You and your laughs will be forever in my heart, *grazie mille!* A special thanks to my co-supervisor and colleague Dr. Victor Candelario that supported me in all the steps of the big challenge that was this work, and give me so many opportunities. A great thanks to the jury members for dedicating your precious time to read and help to improve this work.

Thanks to the whole team of the AQUAlity project, ESRs, professors, and staff. The opportunity to work three years with all of you was truly transformative. Thank you, Prof. Paola Calza, for carrying this great responsibility in your shoulders. A special thanks to my colleagues Alice, Davide, Nuno, Reni, Masho, Ilaria, Cristina, Zsuzsanna, Oihane, Dimitra, Bethel, and Iván, with which I shared incredible moments.

A warm thanks to the colleagues and friends of Work Package 4, Kate, Dennis, and Esra, for your unlimited help, kindness, and company in the challenging months of the secondments. I would not have made it without you, I hope we can continue working together.

Thanks to...

- ...the colleagues from the Department of Chemistry of UNITO, including master and PhD students, visitors, professors, and technicians. A special thanks to Chiara Gionco and Prof. Paganini, which shared their precious zirconia with me.
- ...all the LiqTech team for welcoming me so closely and make me feel part it. Thank you for the unlimited support I had to develop my membranes. Your company is an example of diversity, not judging people for their race, sexuality, or nationality.
- ...the Department of Chemistry and Bioscience of Aalborg University that hosted and supported me for months, allowing me to achieve more than I expected. A special thanks to Prof. Vittorio for the trust and the opportunities.
- ...all members of Plataforma Solar de Almeria that even in difficult times were happy in helping me to develop my work.

...To the European Union for founding science, recognizing its utmost value in the well-being and development of our society.

Aos meus pais, Rosângela e Murilo, pelo amor incondicional e pelo suporte, dia a dia, durante 3 anos. Mesmo distante, vocês estavam presentes em todos os momentos, a cada conquista, a cada obstáculo superado. Os últimos tempos não foram fáceis, mas não existe fronteira para o amor de vocês, ele me fez crescer e encarar o mundo de cabeça erguida. Essa conquista também é de vocês. Obrigado por serem pais maravilhosos. Ao meu irmão, Murillo, por ser uma inspiração de coragem para encarar novos desafios.

Aos supervisores que me fizeram chegar até aqui e agora são amigos queridos, Adriane, Tania, Julio, Estêvão, Roberto, Maria Elisa, e Ricardo. Integridade é um valor que não se aprende nos livros, mas que se transmite sendo exemplo. Obrigado por todas oportunidades que vocês me deram e por nunca cortarem minhas asas quando precisei voar.

À prof. Maria das Graças Caria (in memoriam) do Colégio Santo Antônio, que dividiu comigo sua paixão pela Química e me ensinou que enfrentar os pequenos desafios é se preparar para os grandes. Infelizmente vítima da pandemia, sua partida evidencia a importância da educação e do investimento em ciência para transformação do nosso país.

À minha amiga Gisele, que não encontro palavras para descrever, tamanha a amizade e o amor que compartilhamos. Essa cumplicidade se entende nos desafios de ser pesquisador, e no sonho de ver nosso país justo e democrático, um país que valorize a educação e a vida do seu povo. Sem você eu não teria conseguido chegar até aqui, muito obrigado.

À minha amiga Laura, por estar sempre presente e me dar forças para seguir em frente. Mesmo quando não nos falamos, é só lembrar de você que já ponho um sorriso no rosto. À minha querida Luiza, cujo amor e alegria me deram forças para seguir em frente. Ansioso para compartilhar boas risadas com você.

Ao meu irmão mais novo, Márcio, que é meu confidente e psicólogo, companheiro em todas minhas lutas e que me enche de orgulho a cada nova conquista, admiro sua força na busca da sua felicidade.

Aos meus amigos Rafael, Gilberto, Felipe, Sarah, Isabela, Laís, Gustavo, Gabriela, Mari, Lila, Pri, Mi, Douglas e Samuel. Doe demais ficar todo esse tempo longe de vocês, mas ao mesmo tempo levo vocês sempre aqui comigo no meu coração.

Al mio caro amico Giovanni, che mi ha accolto a Torino ed è stato responsabile di tutti i momenti incredibili che ho trascorso lì. Il tuo supporto è stato essenziale nei momenti più difficili. Grazie infinite.

Para él que es mi base, mi razón de vivir, llegaste a mi vida cuando no lo esperabas y lo cambiaste por completo. Te has convertido en mi Norte, mi compañero para toda la vida. Eres todo lo que soñé y más de lo que jamás imaginé. Esta tesis también es una victoria para ti, y espero compartir contigo muchas más. Te quiero!